UNIVERSITÉ DU LUXEMBOURG

PhD-FSTC-2016-58
The Faculty of Sciences, Technology and Communication

DISSERTATION

Defense held on 24/11/2016 in Luxembourg

to obtain the degree of

DOCTEUR DE L'UNIVERSITÉ DU LUXEMBOURG

EN PHYSIQUE

by

Mads Christof WEBER
Born on 18 April 1986 in Heidelberg (Germany)

ELECTRONIC AND STRUCTURAL PROPERTIES OF BISMUTH- AND RARE-EARTH-FERRITES

Dissertation defense committee

Prof. Dr. Jens Kreisel, dissertation supervisor
Université du Luxembourg, Luxembourg Institute of Science and Technology

Prof. Dr. Ludger Wirtz, Chairman
Université du Luxembourg

Prof. Dr. Matthieu Le Tacon, Vice Chairman
Karlsruher Institute für Technologie

Prof. Dr. Gustau Catalán Bernabé
Catalan Institute of Nanoscience and Nanotechnology

Dr. Mael Guennou
Luxembourg Institute of Science and Technology

Acknowledgments

During the last four years, many people were involved in the research providing academic, technical or moral help to make this thesis happen.
First and foremost, I would like to express my deepest gratitude to my advisor Prof. Dr. Jens Kreisel for giving me the possibility to perform this work under his guidance and for manifold opportunities in the context of this work and beyond. His constant scientific, strategic and personal guidance, support and motivation were essential for the success of this thesis. I could not have had a better supervisor and mentor.
Dr. Mael Guennou cannot be thanked enough. His fantastic co-supervision was a cornerstone for this work. His constructive input, patience, availability for many in-depth discussions, immense knowledge and ultimately the very careful proof-reading of the manuscript were of great importance and help to me.
I would like to thank sincerely Prof. Dr. Ludger Wirtz on the one hand for being the president of the thesis jury, but also for following the progress of the work over the full time as a member of the CET, giving constructive input and raising important questions about the work.
A special thanks goes to Prof. Dr. Matthieu Le Tacon and Prof. Dr. Gustau Catalan for being members of the jury. I highly appreciate their effort to come to Luxembourg, read the manuscript and their challenging and fruitful questions during the defense.

I was very fortunate to collaborate scientifically with many external groups during the research of the work. I am very grateful

- *to Dr. Yannick Gillet and Prof. Dr. Xavier Gonze, Université catholique de Louvain, Belgium, for the fruitful and continuous exchange on theoretical and experimental aspects of Raman scattering over the full time of the thesis.*

- *to Dr. Steven Huband and Prof. Dr. Pam A. Thomas, Warwick University, UK, as well as Dr. Donald M. Evans and Prof. Dr. Michael Carpenter, Cambridge University, UK, for the possibility to spend time at their laboratories to perform birefringence measurement and RUS measurements, respectively. The help with the experiments, data treatment, time for discussions and scientific input are highly appreciated.*

- *to Dr. Constance Toulouse and Prof. Dr. Maximilien Cazayous, Paris 7, France, for collaborating on 'the wavelength-dependent Raman spectroscopy on $BiFeO_3$'-project and in particular for the great measurements, as well as Rui Vilarinho, Prof. Dr. Abílio Almeida and Prof. Dr. Joaquim Agostinho Moreira for collaborating on the '$RFeO_3$'-project.*

- *to Dr. Brahim Dhkil, Central Paris, France, Prof. Dr. Ekhard Salje, University Cambridge, UK, Prof. Dr. James F. Scott, St. Andrews, UK, Prof. Dr. Susanne Siebentritt, University of Luxembourg, and Dr. Inmaculada Peral Alonso, University of Luxembourg, for many fruitful discussions.*

- *The samples used in this work were provided by many external partners. I would like to thank R. Haumont (Université Paris Sud) and D. Colson (CEA Saclay), B. Dkhil (Université Paris Saclay) and W. Ren (Shanghai University), E. Queiros and P.B. Tavares (University of Trás-os-Montes e Alto Douro), and M. Mihalik Jr., M. Mihalik, and M. Zentkova (Slovak Academy of Sciences) for providing high-quality samples.*

I would like to thank all members of the Materials Research and Technology department, in particular the entire FMT group for all their assistance and for making the time of my PhD such a great experience; I would like to express my deepest thank

- *to Emmanuel Defay for all his management work as head of the group.*

- *to Jorge Íñiguez and Hong Jian Zhao. I highly appreciate the interaction and cooperation to link theory and experiment.*

- *to Torsten Granzow for the discussions and the help with dielectric measurements.*

- *to the technical support team (A. Chauvière, A. el Moul, S. Menaouli, Y. Rault, J. Furgala) and to Yves Fleming for the help with the XRD measurements.*

- *to Corinne Lavorel for all her administrative assistance.*

A great thanks goes to my fellow labmates, for all their help, the long discussions, the positive distraction at work and the great fun outside of work.

- *Guillaume Nataf and Alexander Schober for exploring the world of Raman spectroscopy together and always coming up with new ideas. I sincerely hope to continue these productive collaborations in the future.*

- *Charlotte Cochard, Alex Gansen, David Spirito, Ingrid Cañero Infante, Jan Sendler, Shankari Nadupalli, thank you very much for the fantastic time and in particular for all your support and motivation in the tough time of writing the manuscript as well as to Tobias Bertram to whom I am indebted for careful proofreading of the manuscript.*

- *Sunil, Carlos, Peng, Romain, Nicolas, Hameeda, Gaëlle, Olivier, Ben, Canan, Arindam, Nohora, Conrad, Max, Germain, Patrick, Brahime, Marina, Daniele, Mauro, Vincent, Hongtao, Fintan, thank you for good times we spent together in the lab, during coffee breaks and outside of the institute making the time at the institute so enjoyable.*

I would like to thank my parents, Ursula and Michael, my sister, Lilli, for their constant motivation and support until the very last minute of submitting. Last but certainly not least, I would like to express my deepest gratitude to Cristina for her continuous moral support in good and bad moments, for calming me down in situations of highest stress and for the help to keep the focus on the essentials.

I am grateful for financial support from the Fond National de Recherche Luxembourg.

Contents

Introduction **1**

1 Fundamentals **5**
1.1 Functional perovskite-type oxides 5
1.1.1 Crystallographic properties 6
1.1.2 General properties and multiferroicity 12
1.2 Raman scattering 14
1.2.1 Macroscopic approach 17
1.2.2 Scattering cross section 22
1.2.3 Quantum mechanical description 23
1.2.4 Crystal vibrations - phonons 31
1.2.5 Soft modes in Landau theory of phase transitions . . . 41
1.2.6 Probing magnetism by Raman scattering 45

2 Experimental methods **47**
2.1 Raman spectroscopy 47
2.1.1 Experimental setup 47
2.1.2 Porto's notation 48
2.1.3 Corrections of the Raman spectrum 49
2.2 Optical birefringence - Metripol setup 52
2.3 Temperature dependent measurements 55
2.4 Resonant ultrasound spectroscopy (RUS) 56

3 Raman scattering on RFeO$_3$ 59
3.1 Rare-earth orthoferrites - structure . . . 60
3.2 Sample description . . . 63
3.3 Raman scattering on rare-earth orthoferrites . . . 65
3.3.1 Raman spectra and mode assignment . . . 65
3.3.2 Phonon modes vs. ionic radii and octahedra tilt angle 70
3.4 Conclusion . . . 76

4 Structural investigations of SmFeO$_3$ 77
4.1 Review of magnetic properties of SmFeO$_3$ . . . 78
4.2 SmFeO$_3$ samples . . . 81
4.3 Results . . . 82
4.3.1 Raman scattering . . . 82
4.3.2 Resonant ultrasound spectroscopy (RUS) . . . 89
4.3.3 Birefringence measurements . . . 93
4.4 Discussion . . . 98
4.4.1 Impact of the spin ordering at T_N (680 K) on the lattice 98
4.4.2 Anomalies during the spin-reorientation (450 - 480 K) 100
4.4.3 High temperature anomaly ($\sim$ 740 K) . . . 101
4.4.4 Low temperature anomalies ($\sim$ 220 K) . . . 101
4.5 Conclusion . . . 108

5 Temperature evolution of the band gap in BiFeO$_3$ 109
5.1 Structure of BiFeO$_3$ . . . 111
5.2 Optical properties and band structure . . . 112
5.3 Additional experimental setup and samples . . . 113
5.4 The Raman spectrum of BiFeO$_3$ . . . 115
5.5 Multiwavelength Raman spectroscopy on BiFeO$_3$ . . . 121
5.5.1 Wavelength dependence of first-order Raman spectra . 121
5.5.2 Tracing the temperature dependence of the band gap 125
5.6 Conclusion . . . 131

Conclusion and Perspectives 133

Introduction

Today's society demands for high-performance, multi-purpose microelectronic devices which collect, sort and distribute information in the most efficient way. Accordingly, the industry is constantly looking for new ways to record, process, and store this information. Also the need for sensing possibilities, computing power or data storage devices increases tremendously. "The Independent" reported in January, 2016, that data centers are "consuming about 3 per cent of the global electricity supply and accounting for about 2 per cent of total greenhouse gas emissions." [1] This trend can be expected to continue (see also Ref. 2). Accordingly, an important goal for our society is the minimization of this energy consumption. Such challenges are intimately related to advances in materials research and technology. The European Commission estimates that "70% of all new product-innovation is based on materials with new / improved properties." [3]

One approach of the material research community is the engineering of new materials with preferably strongly-coupled multi-functional properties with low power consumption for reading and writing processes.

In this context, perovskite-type oxides ABO_3 are a versatile group of materials. The possibility to incorporate many different elements into the structure paired with structural distortions gives rise to a large variety of properties and coupling phenomena.

Particularly interesting for applications are the so-called ferroic properties, namely ferromagnetism, ferroelectricity and ferroelasticity, which can be tuned by the chemical composition or external parameters. Accordingly, materials/perovskites which possess more than one ferroic order - *multiferroics* - are even more attractive as they can intrinsically combine magnetic, ferroelectric, and elastic properties [4,5].

In multiferroics the magnetism and the ferroelectricity can occur independently [6]. This is the case for example in the most prominent representative bismuth ferrite, $BiFeO_3$, which is one of the only room-temperature multi-

ferroic materials with a particularly strong polarization. On the other hand, the ferroelectricity can also be induced by magnetism[6] such as in $TbMnO_3$[7] or $GdFeO_3$[8]. The magnetically induced ferroelecticity allows a more direct coupling. However, the polarization is usually substantially smaller than in $BiFeO_3$, for example.
Commonly, these properties result from small atomic displacements. Therefore, a detailed understanding of subtle structural distortions is of general importance for the understanding of multiferroicity.

More recently, the interest for multiferroics has been extended to their interactions with light[9] - namely photovoltaic properties[10–12]. This adds another coupling possibility to the rich portfolio of multiferroic materials, making multiferroics ideal multifuntional materials for future-devices. One of the major challenges within this topic is the understanding of charge-carrier creation and separation mechanisms. The knowledge of the electronic band structure as well as defect state is therefore crucial.

Objectives and outline of this work

With the present work, we wish to contribute to the field of multiferroic perovskites and their interaction with light. For this purpose we analysis, two material systems rare-earth orthoferrites, RFeO$_3$, with a special focus on $SmFeO_3$, and bismuth ferrite, $BiFeO_3$.

In a first part, an introduction is given to perovskite-type materials and Raman spectroscopy, the main technique of this work. Further measurement techniques will be introduced subsequently.

In the second part of this work, we report a detailed study of the vibrational properties of a rare-earth orthoferrite series. For a long time the major interest in rare-earth orthoferrites has been arising from sophisticated magnetic structures and transitions[13]. More recently, multiferroic properties have been reported for certain RFeO$_3$, induced by the magnetic ordering[8,14,15]. The analysis of the phonon spectra provides a basis for further investigation of potential multiferroic coupling phenomena in RFeO$_3$.

In the third chapter, we focus on one member of the rare-earth orthoferrite family, namely samarium ferrite $SmFeO_3$, in greater detail. In terms of multiferroic properties, $SmFeO_3$ is probably the most controversially discussed member of the orthoferrite family in recent literature[16–19]. To create a better understanding of the interaction between magnetism and lattice, we investigate the evolution of structural properties as a function of temperature with a particular focus on the magnetic transition temperatures.

In the last part of this work, bismuth ferrite is studied. $BiFeO_3$ is certainly the most investigate multiferroic material. Accordingly, the structural and multiferroic properties are well-known.[20] More recently, $BiFeO_3$ receives additional attention for its photovoltaic properties[21–23]. However, the electronic band structure and defect states of $BiFeO_3$ are not fully understood despite their major importance for light induced effects. Therefore, we aim to shed light on the electronic band structure of $BiFeO_3$ by wavelength-dependent Raman spectroscopy.

Chapter 1

Fundamentals

1.1 Functional perovskite-type oxides

Originally, perovskite is the mineral name of calcium titanate $CaTiO_3$. It was discovered by the Prussian mineralogist Gustav Rose and named in honor of the Russian Napoleonic-wars veteran and later minister of the Interior L. A. Perovski[26]. More generally, the term perovskite is used for the crystal structure type of calcium titanate. The chemical formula of materials crystallizing in the perovskite structure is ABX_3. In case of perovskite-type oxides, the site X is occupied by oxygen O. The ideal perovskite adopts a cubic structure with the space group $Pm\bar{3}m$[27], illustrated in Fig. 1.1, classically exemplified by strontium titanate $SrTiO_3$. The A atom is placed at the center of the cube. The B atoms are occupying the eight vertices of the cube. The oxygen atoms are found on the edges, forming octahedra with a B atom in their center. With respect to the A atom the oxygens form a cuboctahedron.
The great interest in the perovskite structure lies in the possibility to incorporate a large number of different chemical elements. Depending on the size and the electron structure of the elements, it is possible to tune structural distortions and thus engineer the physical properties of perovskite-type oxides.

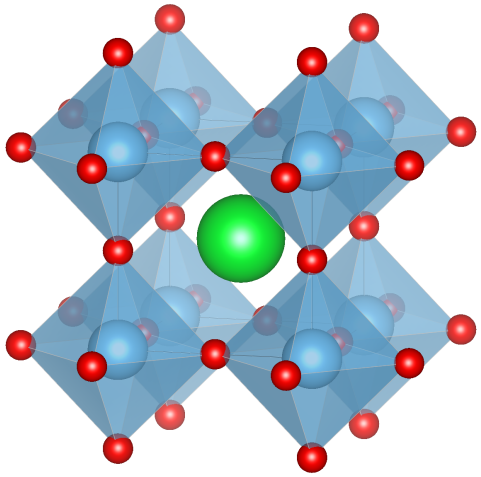

Figure 1.1: Ideal cubic perovskite stucture of the space group $Pm\bar{3}m$ illustrated by $SrTiO_3$ [24]. The figure was created using VESTA [25]. (Note, all figures in this work representing structural data have been created using VESTA.)

1.1.1 Crystallographic properties

The size ratio of the incorporated elements is crucial to allow crystallization in the perovskite structure. Most perovskites are considered to be ionic compounds where the ions can be regarded as spheres with ionic radii r. Typically the A-site cations are of similar size as the oxygen anions but larger than the B-site cations. In 1926 Goldschmidt found that the ionic sizes follow a certain ratio to allow crystallization in the perovskite structure [28]:

$$t = \frac{(r_O + r_A)}{\sqrt{2}(r_O + r_B)}, \tag{1.1}$$

where r_A, r_B and r_O are the ionic radii of A and B cations and oxygen anion. The tolerance factor t is a measure for the stability of the perovskite structure for a given choice of A and B cations. The ideal cubic perovskite structure has a tolerance factor t of unity corresponding to a perfect stacking of rigid spheres. In practice, the tolerance factors of cubic perovskites range from 0.8 to 1.1. For example, it is 1.002 for cubic $SrTiO_3$ (Fig. 1.1). Materials with tolerance factors of approximately $t = 0.8$ to 1.2 can crystallize in perovskite structures. However, the tolerance factor can only be used to approximate if a crystal may possess a perovskite structure and is no measure for the space group of a crystal [27]. The tolerance factor takes solely the ionic size into account but no interaction mechanisms or covalent bonds.

The incorporation and combination of different elements into the structure leads to distortions away from the ideal cubic perovskite structure. A lot of work has been devoted to the study of different distortions and their impact on the crystal symmetry. Works of Megaw, Glazer, Woodward, Howard, Stokes and Carpenter, among others, have lead to an in-depth description of practically all types of distortions and the resulting crystalline structures of perovsikte compounds[27,29–40]. Three main types of distortions have been commonly discussed[35]:

(i) Rotation of the corner linked, rigid BO_6 octahedra.
(ii) Displacement of the A or B cation away from their high symmetry position.
(iii) Distortion of the BO_6 octahedra.

In some cases these distortions coexist. These distortions are briefly addressed in the following.

Octahedra tilting

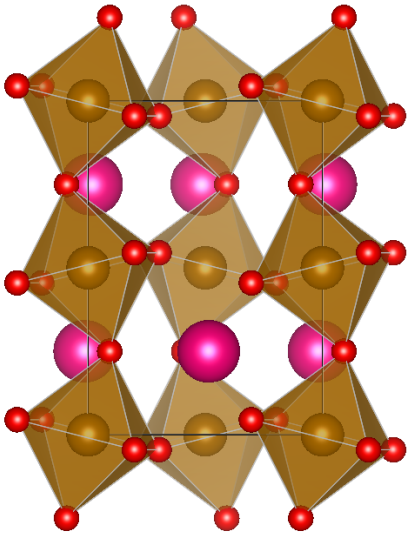

Figure 1.2: Octahedra tilting exemplified by the orthorhombic $SmFeO_3$ with space group $Pnma$[41].

Octrahedra tilts around crystallographic axes are the most common type of distortions in the perovskite structure[35]. The corner-linked BO_6 octahedra are assumed to be rigid, while the AO_{12} cuboctahedra deforms strongly

leading to changes of the A−O bond lengths. This octahedra tilting is illustrated in Fig. 1.2 by the orthorhombic $SmFeO_3$.
A notation to describe the octahedra tilt system of a perovskite crystal was introduced by Glazer[30]. The rotations are described with respect to axes of the ideal cubic perovskite structure $Pm\overline{3}m$. Octahedral rotations around the cubic axes x, y and z are represented by the symbols a, b and c. Identical symbols indicate the same rotation angles. Superscripts "+" and "−" indicate the sense of rotation in successive layers. "+" stands for octahedra rotation in the successive layer in the same direction, i.e. in-phase; "−" implies an anti-phase octahedra tilt in the successive layer. If there is no rotation around an axis, a zero is used as superscript.[27,30] Hence, the cubic $Pm\overline{3}m$ structure without octahedral tilts is denoted as $a^0a^0a^0$. The symbol $a^0b^+b^-$, for example, represents a tilt structure with no rotation around the pseudocubic x-axis, the octahedra are rotated by the same angle about y and z, but with in-phase and anti-phase tilting of the successive layer.
Particularly fruitful was the octahedra tilt analysis by Howard and Stokes following group theoretical rules and Landau theory of phase transitions. This allowed to identify the space groups corresponding to a tilt system and the group-subgroup relations of the different tilt systems where the octahedra tilts represent the order parameter[35]:
The different tilt systems can be described as the superposition of the following tilts: $a^+b^0b^0$, $b^0a^+b^0$, $b^0b^0a^+$, $a^-b^0b^0$, $b^0a^-b^0$ and $b^0b^0a^-$[35]. The combinations give rise to 25 distinct tilt systems (including $a^0a^0a^0$). However, these 25 tilt systems can be reduced to 15 simple systems due to geometrical reasons or because some tilt systems possess a higher symmetry than required by the space group. For example $a^0b^+b^+$ has the same symmetry as $a^0b^+c^+$ and does therefore not appear in the list of Howard and Stokes[35]. The possible space groups of perovskite-type materials and the corresponding subgroup relations that arise from octaherdal tilts only are presented in Fig. 1.3.

It is difficult to predict which tilt system will be established for a particular chemical composition. Certainly, the size ratio of A and B cation plays an important role. Furthermore, some tilt systems are more in favor of energy optimization of A-O bondings with predominately ionic character, while others will be adapted by compounds with an important covalent character[33]. For example, the $a^+b^-b^-$ tilt system, which leads to the orthorhombic $Pnma$ structure, has been found by Woodward to minimize the repulsive A-O overlap and to maximize the A-O covalent bonding[33]. Therefore, compounds

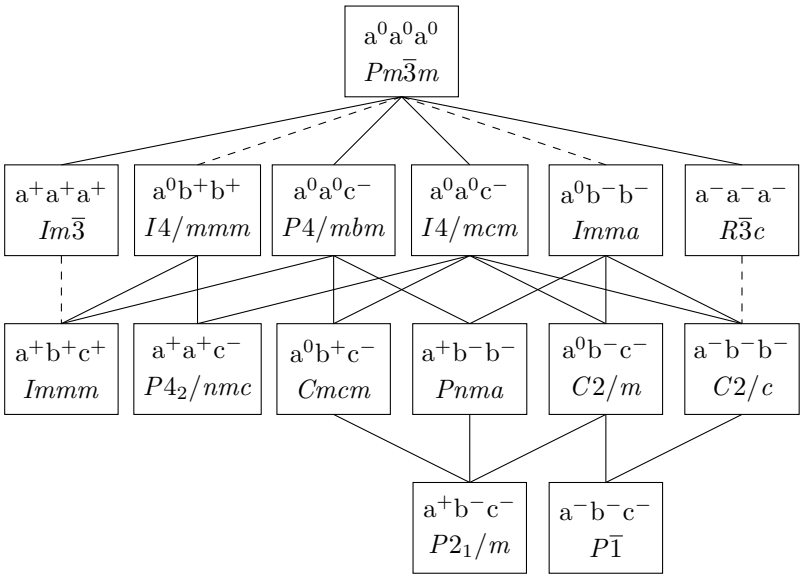

Figure 1.3: Group-subgroup relations for space groups arising from the 15 different tilt systems. Solid lines represent second-order transitions whereas dashed lines indicate transitions required to be of first-order nature. The scheme has been reproduced from Ref. 35.

with a small tolerance factor t or an A cation of 'large' electronegativity are likely to adapt the $a^+b^-b^-$ tilt system[33].
Mitchell reviewed the calculation of the octahedral tilt angles in great detail[27]. Octahedra tilt angles are most accurately calculated from atomic positions. Nevertheless, they can be approximated from cell dimensions as well. However, since in real crystals the octahedra are not rigid and regular, but slightly distorted, the octahedra tilt angles tend to be underestimated when determined from unit cell dimensions.[27]

Octahedra distortions

The BO_6 octahedra can be distorted away from their high symmetry shape by elongation/shortening of certain oxygen bonds and changes of the octahedra angles. The strongest octahedra distortions result from the *Jahn-Teller effect*. The Jahn-Teller effect leads to a lowering the energy of the system by lowering the symmetry of the structure. This effect can occur in ABO_3 compounds if the B cation position is occupied by a transition metal with an odd number of electrons in the degenerated e_g (or t_{2g}) orbitals of the d-shell, for example Mn^{3+}, Cr^{2+}, Fe^{4+}, or Cu^{2+}. To minimize the energy, the degeneracy of the d-shell electrons of the B cation is lifted in the crystal

field of the O^{2-} anions. The lifting of the degeneracy is accompanied by a lowering in symmetry and distortion of the octahedra.[27] In this manner the Jahn-Teller effect links the changes in the electronic system to changes of the structure[40].

The most common distortions are either a contraction (or lengthening) of two B–O bonds and a lengthening (or contraction) of the other four B–O bonds, or a lengthening of two and a contraction of the other two bonds[42]. The first distortion results in a tetragonal, the latter in an orthorhombic symmetry of the octahedra[40].

In Fig. 1.4 the Jahn-Teller effect is exemplified by $KCuF_3$. This example has been chosen since the Jahn-Teller effect is the only distortion of this compound. Note that in most cases octahedra distortions occur together with octahedra rotations, for example rare-earth managnites or rare-earth vanadates[40,43].

The octahedra tilting does not require a distortion of the octahedra*[27]. Nevertheless, depending on the space group the octahedra can have a certain distortion, leading to a shortening or lengthening of the B-O bond and/or changes of the O-B-O angles[27]. However these distortions are commonly much smaller than those resulting from the Jahn-Teller effect.

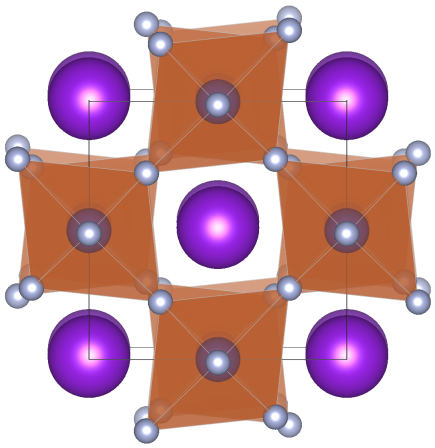

Figure 1.4: Unit cell of $KCuF_3$ with strongly Jahn-Teller-distorted octahedra[44].

*Solely the tilt system $a^+a^+c^-$, with the space group $P4_2/nmc$, requires an octahedra distortion to maintain the structural connectivity[27].

Cation displacement

A and B cations can be displaced from their high symmetry positions. Most prominent displacements of A and B cations occur through covalent bondings with the surrounding oxygens. Here, ns^2 lone pairs, for example of Pb^{2+} or Bi^{3+}, form particularly strong covalent bonds with the oxygen cations resulting in a strong displacement of the cations from the ideal site.[27] Fig. 1.5(a) illustrates the displacement of the B cation inside the octahedra in an exaggerated way. Here, the cation is displaced towards one of the corners of the octahedra, i.e. in cubic settings along one of the principal axis. This displacement leads in general to a tetragonal structure. Equally, the cation can be shifted along a face or body diagonal causing orthorhombic or rhombohedral symmetry, respectively, if the cation displacement is the only distortion of the system. Fig. 1.5(b) shows the tetragonal structure of $PbTiO_3$ where both, A and B cations are displaced from their high symmetry positions.
Less prominent displacement occur often in combination with other distortions. For example under octahedra rotation, the AO_{12} polyhedra deform resulting in a change of A-O bond lengths and eventually in a decrease of A cation coordination number[27]. Some space groups allow a displacement of

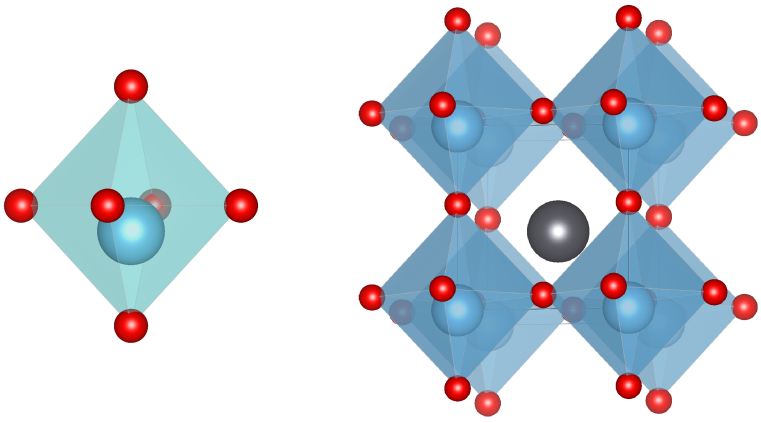

(a) (b)

Figure 1.5: Cation displacements: (a) B cation displacement along a cubic axis within the oxygen-octahedra framework. (b) Illustration of tetragonal $PbTiO_3$ with displacements of A and B cations[45].

the A cations from the ideal site, such as the *Pnma* space group, $a^+b^-b^-$ tilts, where the A cations of most compounds are shifted in an anti-parallel fashion[27].

Since in many perovskite compounds the here discussed distortions appear simultaneously, coupled distortions were studied using group symmetry rule and Landau theory by for example Carpenter and Howard[40,43] or Stokes *et al.*[46] leading to an in-depth description of structural distortions in perovskite-type materials.

1.1.2 General properties and multiferroicity

The variety of the elements that can be incorporated into the perovskite system and the structural flexibility with respect to distortions lead to an extraordinarily rich range of properties. Prominent examples are strong ferroelectricity in $BaTiO_3$ or $PbTiO_3$, piezoelectricity in $Pb(Zr,Ti)O_3$, superconductivity in $Y_{0.33}Ba_{0.66}CuO_{3-\delta}$ or colossal magneto-resistance in $LaMnO_{3-\delta}$. Table 1.1 gives an overview of some properties. Often, perovskite-type oxides possess more than one property which is of interest for potential applications. These materials can potentially have several "functions" in a device and are, thus, called multi-functional materials. Photoferroelectrics, combining fer-

Table 1.1: Properties and prominent examples of materials crystallizing in a perovskite-type structure.[47–50]

Property	Example
dielectric	$CaTiO_3$, $SrTiO_3$
ferroelectric	$BaTiO_3$, $PbTiO_3$
piezoelectric	$Pb(Zr,Ti)O_3$
conducting	$LaNiO_3$, $SrRuO_3$
superconducting	$Y_{0.33}Ba_{0.66}CuO_{3-\delta}$
magnetic	$R FeO_3$, $R CrO_3$, $R MnO_3$
multiferroic	$BiFeO_3$
proton conducting	$SrCeO_3$
catalytic	$LaCeO_3$, $BaCuO_3$
ion conducting	$Li_{0.5-3x}La_{0.5+x}TiO_3$
magneto-resistive	$LaMnO_{3-\delta}$, $La_{1-x}Sr_xMnO_3$

roelectricity and photovoltaic properties, and multiferroics, materials with several ferroic orders, are multi-functional materials *par excellence*.

Multiferroics are commonly classified as "type I" and "type II" [6]. In "type I" multiferroics magnetism and ferroelectricity arise independently. Classical examples are $BiFeO_3$ or the lead containing $Pb_2(Fe,Ta)O_6$, $PbFe_{0.5}Nb_0.5O_3$ or $Pb(Zr,Ti)O_3$-$Pb(Fe,Ta)O_3$ [7,51,52]. In both cases, covalent bonds due to ns^2 electron lone-pairs give rise to ferroelectric displacements [27]. The ferroelectricity occurs usually at higher temperatures than the ordering of the Fe^{3+} magnetic moments. Nevertheless, both properties can couple, such that the direction of polarization can influence the magnetic ordering and vice versa, as illustrated in $BiFeO_3$ [53].
On the contrary, in "type II" multiferroics ferroelectricity is induced by magnetism† [6]. The most investigated example of "type II" multiferroics is $TbMnO_3$. In this case, Mn^{3+} spins order in a cycloidal structure at low temperatures which leads to a symmetry breaking, allowing for ferroelectric displacement [54,55]. A new group of "type II" multiferroic has been proposed more recently. The group includes several rare-earth manganites $R MnO_3$ [56] and ferrites $R FeO_3$ [8,14,15]. Here, the symmetry breaking occurs from the combined magnetic order of A and B cations [6] which gives rise to a ferroelectric displacement. This requires a magnetic A cation, but no cycloidal spin structure is needed. This mechanism is often disregarded because the magnetic moments of the rare-earth A cations are usually assumed to order at very low temperatures.
Generally, the magnetoelectric coupling of "type II" multiferroics is more direct than in the "type I" multiferroics. However, the magnetically induced polarization of "type II" multiferroics is substantially weaker (2 to 3 orders of magnitude) in comparison to "type I" multiferroics where the polarization occurs through the covalent bonds [6].

†Note, the term "type II" multiferroic is ambiguously used in the literature. Here, we use "type II" multiferroic as term for all kinds of materials with magnetically-induced ferroelectricity.

1.2 Raman scattering

Raman scattering is the inelastic scattering of light by a solid, liquid or gas. The Raman effect was first theoretically predicted by Adolf Smekal[57]. Experimentally the phenomenon was first reported by C.V. Raman and K.S. Krishnan in 1928[58] simultaneously with the Russian scientists G. Landsberg and L. Mandelstam[59]. Only two years after the discovery, in 1930, C.V. Raman was awarded the Nobel price "for his work on the scattering of light and for the discovery of the effect named after him"[60]. Why the Nobel prize was not shared with the Russian team, remains speculative. Yet, C.V. Raman published the work first and was cited by Landsberg and Mandelstam[61].
Raman spectroscopy is a non-destructive probe for excitations of low energies in the meV regime. In addition, Raman spectroscopy can reveal information about symmetry of the excitations which is difficult to gain otherwise. Excitations can be of magnetic, electronic, vibrational nature and others. However, the main focus of Raman spectroscopy experiments lies on vibrational (phonon) spectroscopy which allows a profound insight into the structural properties of a material. As a consequence, Raman spectroscopy has become a major characterization technique of materials with applications reaching from physical, chemical and bio-chemical to medical analysis[62,63]. Raman scattering is sensitive to even very subtle distortions and, thus, has played a crucial role in understanding structural peculiarities and phase transitions in perovskites[64–68]. In the past, Raman spectroscopy was mainly focused on bulk systems, but is today at least equally applied to the characterization of thin or ultra-thin oxide films[69–71], multilayers[72] and nano-structures[73].
The use of Raman spectroscopy for the investigation of the electronic structure of perovskite-type oxides remains rare, whereas this approach is commonly use for bio-chemical samples[74,75] and in the past for classical semiconductors[76–81].

In this section, we aim to introduce the concepts of Raman scattering, which are of particular importance for this work. First, the scattering process is presented from a macroscopic point of view, followed by a description of the quantum-mechanic expression. In a second part, lattice vibrations are discussed and finally concepts of further applications that are of interest for the present work shall be briefly introduced.

Summary of Raman scattering

This section starts with a brief introduction to the basic mechanism of the Raman scattering effect. Subsequently, an overview of the properties of Raman scattering, which are of particular importance for this work, are given. These properties will be worked out in detail in the following sections.

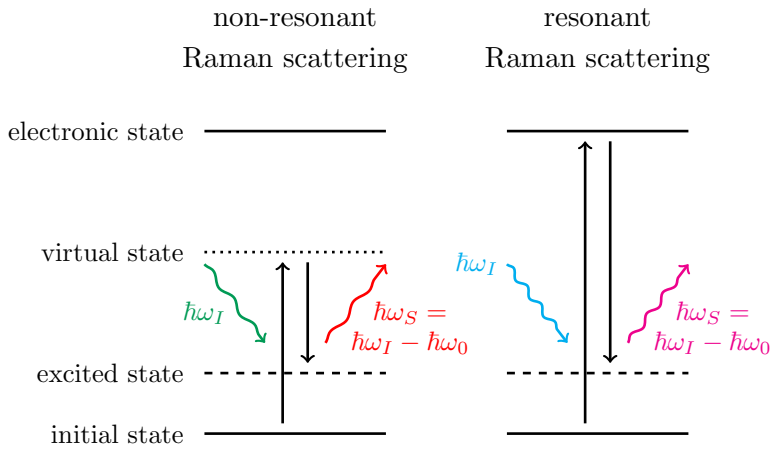

Figure 1.6: Scheme of the Stokes Raman (left) and resonant Raman scattering process (right).

Fig. 1.6 (left) illustrates the (non-resonant) *Raman scattering* process. Incident light of the energy $\hbar\omega_I$ excites the system from the initial state into virtual state. Under the emission of a photon of the energy $\hbar\omega_S = \hbar\omega_I - \hbar\omega_0$, the system falls back into an excited state. If the energy of the incident light is in the vicinity of an electronic transition of the system (see Fig. 1.6 (right)), the intensity of the scattered light is dramatically enhanced. This effect - called *resonant Raman scattering* - provides information about the initial and the higher electronic state of the resonant scattering process.

Important properties:

1. **first-order Raman scattering (one excitation):**

   - Energy conservation: $\omega_0 = \omega_I - \omega_S$
   - Momentum conservation: $\boldsymbol{q} = \boldsymbol{k}_I - \boldsymbol{k}_S$
   - $|\boldsymbol{q}| = 0$, the momentum of light is negligible in comparison to the size of the Brillouin zone.

   $\Rightarrow$ Only Γ-point excitations can be probed.

   $\Rightarrow$ Discrete spectrum.

   $\Rightarrow$ Resonant Raman scattering only for direct electronic transitions.

2. **second- (or higher-) order Raman scattering (multiple excitations):**

   - Energy conservation: $\sum_i \omega_{0,i} = \omega_I - \omega_S$
   - Momentum conservation: $\sum_i \boldsymbol{q}_i = \boldsymbol{k}_I - \boldsymbol{k}_S$
   - $|\sum_i \boldsymbol{q}_i| = 0$, the momentum of light is negligible in comparison to the size of the Brillouin zone.

   $\Rightarrow$ Excitations of the entire Brillouin zone can be probed.

   $\Rightarrow$ Continuous spectrum.

   $\Rightarrow$ Resonant Raman scattering for direct and indirect electronic transitions.

3. **Consequences of resonant Raman scattering:**

   - Enhancement of the scattered intensity.
   - Changes in intensity ratio of different excitation bands.

1.2.1 Inelastic light scattering - Raman scattering - Macroscopic approach

In this section, the basic features of the inelastic light-scattering process are discussed. We follow the macroscopic approach, as described for example by Hayes and Loudon[82] or Yu and Cardona[79].
For a light scattering experiment, we consider a medium which is irradiated by light. The incident light shall be a sinusoidal plane electromagnetic wave $\boldsymbol{E}(\boldsymbol{r},t)$ with a frequency ω_I and momentum vector $\boldsymbol{k}_I$ defined by

$$\boldsymbol{E}(\boldsymbol{r},t) = \boldsymbol{E}(\boldsymbol{k}_I,\omega_I)\cos(\boldsymbol{k}_I\cdot\boldsymbol{r}-\omega_I t). \tag{1.2}$$

The electromagnetic wave induces a polarization $\boldsymbol{P}(\boldsymbol{r},t)$ with equivalent frequency and momentum vector in the medium, as

$$\boldsymbol{P}(\boldsymbol{r},t) = \boldsymbol{P}(\boldsymbol{k}_I,\omega_I)\cos(\boldsymbol{k}_I\cdot\boldsymbol{r}-\omega_I t). \tag{1.3}$$

Polarization and electric field are connected by the electric susceptibility χ of the medium. The electric susceptibility, a second-rank tensor, specifies how a material responds to an external electric field. The i-th Cartesian coordinate of the polarization is given as

$$P^i(\boldsymbol{k_I},\omega_I) = \sum_{j=1}^{3}\chi^{ij}(\boldsymbol{k_I},\omega_I)E^j(\boldsymbol{k_I},\omega_I). \tag{1.4}$$

Now, be $\boldsymbol{X}(\boldsymbol{r},t)$ an excitation of the medium, which perturbs the electric susceptibility χ with the form:

$$\boldsymbol{X}(\boldsymbol{r},t) = \boldsymbol{X}(\boldsymbol{q},\omega_0)\cos(\boldsymbol{q}\cdot\boldsymbol{r}-\omega_0 t). \tag{1.5}$$

As mentioned before, the excitation can be of different nature. For example vibrational displacements, spin deviations in a magnetic system, electronic excitations, etc. Under adiabatic approximation, i.e. the frequency ω_I of the incident light is much larger than the frequency ω_0 of the excitation $\boldsymbol{X}(\boldsymbol{r},t)$, and the assumption that the amplitude of the excitation is small compared to the lattice, the susceptibility tensor χ can be expanded in a Taylor series

as a function of the excitation $\boldsymbol{X}(\boldsymbol{r},t)$:

$$\begin{aligned}\chi^{ij}(\boldsymbol{k}_I,\omega_I,\boldsymbol{X}(\boldsymbol{r},t)) = \chi_0^{ij} &+ \sum_{k=1}^{3}\left(\frac{\partial\chi^{ij}}{\partial X^k}\right)_0 X^k(\boldsymbol{r},t) \\ &+ \sum_{k,l=1}^{3}\left(\frac{\partial^2\chi^{ij}}{\partial X^k\partial X^l}\right)_0 X^k(\boldsymbol{r},t)X^l(\boldsymbol{r},t) \\ &+ ... \\ = \chi_0^{ij} &+ \chi_1^{ij} + \chi_2^{ij} + ...\end{aligned} \tag{1.6}$$

k and l represent Cartesian coordinates of the excitation $\boldsymbol{X}$. The first term expresses the unperturbed susceptibility. χ_1^{ij}, linear in $\boldsymbol{X}$, describes the change of the susceptibility due to the perturbation of one excitation, the term quadratic in $\boldsymbol{X}$ represents the perturbation as a result of two excitations, and so on. For the moment, we are interested in a single excitation only. Therefore, we take only the first two terms of the Taylor series into account. The polarization expresses as:

$$\begin{aligned}P^i(\boldsymbol{r},t,\boldsymbol{X}) &= \sum_{j=1}^{3}\chi_0^{ij}E^j(\boldsymbol{r},t) + \sum_{j,k=1}^{3}\left(\frac{\partial\chi^{ij}}{\partial X^k}\right)_0 X^k(\boldsymbol{r},t)E^j(\boldsymbol{r},t) \\ &= P_0^i(\boldsymbol{r},t,\boldsymbol{X}) + P_{ind}^i(\boldsymbol{r},t,\boldsymbol{X})\end{aligned} \tag{1.7}$$

With Eq. (1.2) we find that the polarization stemming from the first term is given by

$$P_0^i(\boldsymbol{r},t,\boldsymbol{X}) = \sum_{j=1}^{3}\chi_0^{ij}E^j(\boldsymbol{k}_I,\omega_I)\cos(\boldsymbol{k}_I\cdot\boldsymbol{r}-\omega_I t). \tag{1.8}$$

It oscillates with the same frequency as the incident light. Thus, the light is elastically scattered referred to as *Rayleigh scattering*.
The second term $P_{ind}^i(\boldsymbol{r},t,\boldsymbol{X})$ is composed of the derivative of the susceptibility with respect to the excitation $\boldsymbol{X}$, the excitation $\boldsymbol{X}$ itself and the electro-magnetic wave $\boldsymbol{E}$ and is thus induced by the excitation.
With Eq. (1.2) and (1.5) and the trigonometric relation $\cos(a)\cos(b) =$

$\frac{1}{2}\left[\cos(a+b)+\cos(a+b)\right]$ we can write $P^i_{ind}(\boldsymbol{r},t,\boldsymbol{X})$ as

$$\begin{aligned} P^i_{ind}(\boldsymbol{r},t,\boldsymbol{X}) = &\sum_{j,k=1}^{3}\left(\frac{\partial\chi^{ij}}{\partial X^k}\right)_0 X^k(\boldsymbol{q},\omega_0)\cos(\boldsymbol{q}\cdot\boldsymbol{r}-\omega_0 t) \\ &\times E^j(\boldsymbol{k_I},\omega_I)\cos(\boldsymbol{k}_I\cdot\boldsymbol{r}-\omega_I t) \\ =&\frac{1}{2}\sum_{j,k=1}^{3}\left(\frac{\partial\chi^{ij}}{\partial X^k}\right)_0 X^k(\boldsymbol{q},\omega_0)E^j(\boldsymbol{k}_I,\omega_I) \\ &\times\left[\cos((\boldsymbol{k}_I-\boldsymbol{q})\cdot\boldsymbol{r}-(\omega_I-\omega_0)\cdot t\right) \\ &+\cos((\boldsymbol{k}_I+\boldsymbol{q})\cdot\boldsymbol{r}-(\omega_I+\omega_0)\cdot t)\Big] \end{aligned} \tag{1.9}$$

The induced polarization decomposes into the sum of two cos-functions. Compared to the undisturbed polarization, the frequencies and momentum vectors are altered by the frequency ω_0 and the momentum $\boldsymbol{q}$ of the excitation $\boldsymbol{X}$. Thus, the polarization emerging from the *susceptibility derivatives* contributes to the inelastic scattering of the light. This inelastically scattered light gives rise to sidebands in the spectrum of scattered light. The part of the inelastically scattered light resulting in a red shift of the scattered light with $\omega_S=\omega_I-\omega_0$ and $\boldsymbol{k}_S=\boldsymbol{k}_I-\boldsymbol{q}$ is called *Stokes Raman scattering* and the blue shifted contributions with $\omega_{AS}=\omega_I+\omega_0$ and $\boldsymbol{k}_{AS}=\boldsymbol{k}_I+\boldsymbol{q}$ are called *anti-Stokes Raman scattering*. The difference in frequency of incident and scattered light is referred to as *Raman shift* or *Raman frequency*. As energy and momentum have to be conserved in the inelastic light scattering process the Raman shift corresponds to the energy of the excitation $\boldsymbol{X}$. Fig. 1.7 illustrates the scheme of typical spectrum of Stokes, anti-Stokes and Rayleigh scattering for three different excitation $X(1)$, $X(2)$, $X(3)$. Stokes and anti-Stokes intensities are related by[82]:

$$n(\omega)I_{\text{Stokes}} = [n(\omega)+1]I_{\text{anti-Stokes}} \tag{1.10}$$

where $n(\omega)$ is the Bose-Einstein thermal occupation factor. Thus the intensity of anti-Stokes Raman scattering processes is always weaker than for Stokes Raman scattering.
Thereafter, we only consider Stokes Raman scattering in the present work. For reason of convenience, Stokes scattering is commonly displayed at positive wavenumbers despite the actual red-shift.

In short, an excitation of the medium can modulate the electric susceptibility χ. The modulated electric susceptibility causes inelastic scattering

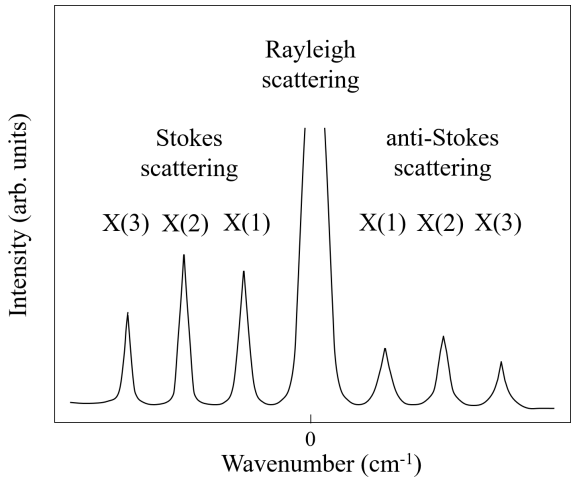

Figure 1.7: Schematic Raman spectrum of three excitations X(1), X(2) and X(3) with the band positions of Stokes and anti-Stokes scattering symmetric with respect to the Rayleigh scattering at 0 cm^{-1}.

of light. The second-rank tensor χ_1, responsible for the inelastic scattering process, is called *Raman tensor*. An excitation is named *Raman-active* if the susceptibility derivative of the excitation does not vanish:

$$\left(\frac{\partial \chi^{ij}}{\partial X^k}\right)_0 \neq (0)\,, \forall i,j,k = 1,2,3 \tag{1.11}$$

Symmetry properties of the Raman tensor

The symmetry of the Raman tensor is directly linked to the point group of the crystal. Following Neumann's principle, the symmetry elements of the point group are included in the symmetry elements of any physical property of the crystal[83]. This holds equally for the induced polarization in Eq. 1.9, which is defined by the susceptibility derivative. Therefore, the excitation can only be Raman-allowed if the Raman tensor remains unchanged under the symmetry operations of the point group. Group theory allows to calculate the symmetries of the Raman-allowed excitations and Raman tensors from its point group[84,85]. Thus different materials with the same point group possess Raman tensors of same symmetries, however, the number of bands may vary. Furthermore, the values of components of the Raman tensors are unique to a certain excitation of a particular material[82].

Consequence of scattering of visible light

By scattering of visible light, the possible processes are restricted by energy range and momentum of visible light. The momentum of visible light is small compared to the size of the Brillouin zone. The possible momentum transfered in the scattering process is approximately three orders of magnitude smaller than the Brillouin zone. Therefore, the momentum transfer can be approximated to be zero for light scattering processes on a single excitation. Hence, only excitations close to the Brillouin zone center (Γ-point) are accessible by Raman scattering.[82]

$$|\boldsymbol{q}| \approx 0 \tag{1.12}$$

Second-order light scattering

So far, we restricted the discussion to light scattering involving one excitation only. However, scattering processes involving multiple excitations are also possible and are called *second-order* scattering process for two excitations, third-order for three excitations and so forth. For a scattering process on two excitations, the energy and momentum conservation is given by

$$\omega_{0,\sigma,\boldsymbol{q}} + \omega_{0,\sigma',\boldsymbol{q}'} = \omega_I - \omega_S \tag{1.13}$$

$$\boldsymbol{q} + \boldsymbol{q}' = \boldsymbol{k}_I - \boldsymbol{k}_S \tag{1.14}$$

where σ and σ' are two excitation, but not necessarily the same. With Eq. 1.12 we can write

$$\boldsymbol{q} + \boldsymbol{q}' \approx 0. \tag{1.15}$$

In comparison with first-order scattering, **higher-order processes are not limited to the Γ-point**, but the excitations can originate from different points of Brillouin zone with the restrictions of energy and momentum conservation, and selection rules. While the first-order spectrum is discrete, higher- order scattering gives rise to a continuous spectrum, representing to some extend the density of states of the excitation[82]. Maxima in the higher-order spectrum are due to van Hove singularities in the density of states. The symmetry of a higher-order process is given by the direct product of the involved excitations. However, pattern and symmetry of the excitation are $\boldsymbol{q}$-dependent which makes the identification of second-order features difficult.

1.2.2 Scattering cross section

The connecting point between theory and experiment is the scattering cross section σ. The cross section is defined as the rate of energy removal from the incident light as a result of the scattering process, and thus is proportional to the intensity of the scattered light. As discussed in section 1.2.1 inelastically scattered light appears as side bands (Raman bands) of elastically scattered light (Rayleigh). The energy difference represents the energy of the scattering excitation. The intensity of the Raman bands, on the other hand, contains information about the symmetry of the excitation, orientation of the crystal, occupation state of the excitation and in some cases even on the electronic states as shall be discussed in the following. The total cross section determines the light inelastically scattered in all direction for all possible scattering frequencies. In a scattering experiment the main interest lies on the spectral differential cross section (SDCS). It describes the intensity of light as the result of a scattering process in a volume ν into a solid angle $d\Omega$ with a frequency ω_S with respect to the light intensity of the incident beam. Eq. 1.16 gives the SDCS of a Stokes scattering process[82].

$$\frac{d^2\sigma}{d\Omega d\omega_s} = \frac{\omega_I \omega_S^3 \nu \eta_S}{(4\pi\epsilon_0)^2 c^4 \eta_I} \left| \epsilon_0 \sum_{i,j} e_S^i \chi_1^{ij} e_I^j \right|^2 \frac{\hbar}{2\omega_{0,\sigma}} \left(n(\omega_{0,\sigma}) + 1\right) g_\sigma(\omega) \quad (1.16)$$

The SDCS depends linearly on the frequencies of incident beam ω_I and to the power three on the scattered light ω_S. In most cases the SDCS is said to be proportional to ω_I^4 under the approximation $\omega_I \approx \omega_S$. η_S and η_I are the refractive indices for the incident and scattered light. $\boldsymbol{e}_S$ and $\boldsymbol{e}_I$ give the direction of the electric field vectors for the scattering and incident light, respectively; χ_1 is the earlier discussed Raman tensor. $n(\omega_{0,\sigma})$ represents the Bose-Einstein thermal occupation factor of the excitation:

$$n(\omega_\sigma) = \frac{1}{\exp(\hbar\omega_{0,\sigma}/k_B T) - 1} \quad (1.17)$$

This shows that the cross section depends on the temperature T. The subscript σ indicates the excitation mode.
The equation of 'motion' of an excitation X can be approximated by an harmonic oscillator. Accordingly, the frequency dependence of the SDCS, i.e. the line shape of a Raman band, has the shape of a Lorentzian[82]:

$$g_\sigma(\omega) = \frac{\Gamma_\sigma/2\pi}{(\omega_{0,\sigma} - \omega)^2 + (\Gamma_\sigma/2)^2} \quad (1.18)$$

where Γ_σ is the damping (or inverse lifetime) of the excitation.
The heart of the scattered intensity is the quadratic term

$$\left| \sum_{i,j} e_S^i \chi_1^{ij} e_I^j \right|^2 . \tag{1.19}$$

It describes the probability of the scattering process. As we have seen in 1.2.1 the Raman tensor χ_1 is given by a matrix. Its form is defined by the symmetry properties of the crystal and therefore, related to the orientation of the crystalline axes. For certain geometries and directions of the electric field vectors e_I and e_S the scattered light vanishes entirely depending to the symmetry[79]. This ability to suppress bands of a certain symmetry in specific scattering configurations is called *Raman selection rules* and allows to determine the symmetry of Raman-active excitations. In scattering geometries that do not allow full vanishing of bands it is possible to deduce the symmetry of a Raman band from its intensity evolution when rotating crystal around an arbitrary but well-known crystalline direction[86,87].

1.2.3 Quantum mechanical description

For a deeper understanding of the Raman process, the macroscopic approach is not longer sufficient and it becomes necessary to study its quantum mechanical description. In particular, wavelength-dependent phenomena of the Raman scattering process and the interaction of the incident and scattered light with the electronic states of the system require a quantum mechanical description.
From a quantum mechanical point of view, the first-order Raman scattering process consists of the annihilation of a photon, the creation of a bosonic particle corresponding to the excitation and the creation of a photon:
(1) The incident photon is absorbed under creation of an electron-hole pair by promoting an electron from a valence band state $v\boldsymbol{k}_h$ to a conduction band state $c\boldsymbol{k}_e$. In this way the system is excited from its initial state $|0\rangle$ with the energy E_0 into an intermediated state $|n\rangle$ with the energy E_n. n is a shortcut for the conduction band c, the valence band v and the momenta $\boldsymbol{k}_e$ and $\boldsymbol{k}_h$ of the electron-hole pair. (2) This electron-hole pair is scattered into a further intermediate state $|n'\rangle$ under the creation of a bosonic particle corresponding to the excitation. (3) The electron-hole pair is radiatively annihilated under the emission of a photon. The final state $|f\rangle$ of the system corresponds to the initial state $|0\rangle$.[79,82] The electronic system is unchanged

with respect to the initial state. However, the number of particles of the particular excitation has increased by one.

$$
\begin{aligned}
P_{\mathrm{Raman}} = \delta(\hbar\omega_I - \hbar\omega_S - \hbar\omega_{ex})\times \\
\Bigg| \sum_{n,n'} & \frac{\left\langle 0 \middle| H_{eR}(\omega_I) \middle| n \right\rangle \left\langle n \middle| H_{eEx} \middle| n' \right\rangle \left\langle n' \middle| H_{eR}(\omega_S) \middle| 0 \right\rangle}{[\hbar\omega_I - (E_n - E_0)][\hbar\omega_I - \hbar\omega_{ex} - (E_{n'} - E_0)]} && (a) \\
& + \frac{\left\langle 0 \middle| H_{eR}(\omega_I) \middle| n \right\rangle \left\langle n \middle| H_{eR}(\omega_S) \middle| n' \right\rangle \left\langle n' \middle| H_{eEx} \middle| 0 \right\rangle}{[\hbar\omega_I - (E_n - E_0)][\hbar\omega_I - \hbar\omega_S - (E_{n'} - E_0)]} && (b) \\
& + \frac{\left\langle 0 \middle| H_{eR}(\omega_S) \middle| n \right\rangle \left\langle n \middle| H_{eEx} \middle| n' \right\rangle \left\langle n' \middle| H_{eR}(\omega_I) \middle| 0 \right\rangle}{[-\hbar\omega_S - (E_n - E_0)][-\hbar\omega_S - \hbar\omega_{ex} - (E_{n'} - E_0)]} && (c) \quad (1.20) \\
& + \frac{\left\langle 0 \middle| H_{eR}(\omega_S) \middle| n \right\rangle \left\langle n \middle| H_{eR}(\omega_I) \middle| n' \right\rangle \left\langle n' \middle| H_{eEx} \middle| 0 \right\rangle}{[-\hbar\omega_S - (E_n - E_0)][-\hbar\omega_S + \hbar\omega_I - (E_{n'} - E_0)]} && (d) \\
& + \frac{\left\langle 0 \middle| H_{eEx} \middle| n \right\rangle \left\langle n \middle| H_{eR}(\omega_I) \middle| n' \right\rangle \left\langle n' \middle| H_{eR}(\omega_S) \middle| 0 \right\rangle}{[-\hbar\omega_{ex} - (E_n - E_0)][-\hbar\omega_{ex} + \hbar\omega_I - (E_{n'} - E_0)]} && (e) \\
& + \frac{\left\langle 0 \middle| H_{eEx} \middle| n \right\rangle \left\langle n \middle| H_{eR}(\omega_S) \middle| n' \right\rangle \left\langle n' \middle| H_{eR}(\omega_I) \middle| 0 \right\rangle}{[-\hbar\omega_{ex} - (E_n - E_0)][-\hbar\omega_{ex} - \hbar\omega_S - (E_{n'} - E_0)]} \Bigg|^2 && (f)
\end{aligned}
$$

It is important to note that these three processes are not independent, but need to be seen as an ensemble. Energy and momentum conservation hold for the entire process but not necessarily for every intermediate step. No real self-containing absorption or luminescence process as such are taking place to excite or recombine the intermediate states $|n\rangle$ and $|n'\rangle$. That means the intermediated states cannot be measured nor do they possess a lifetime (aside from the lifetime derived from uncertainty relations). These states are therefore named *virtual states*. However, their contribution is cru-

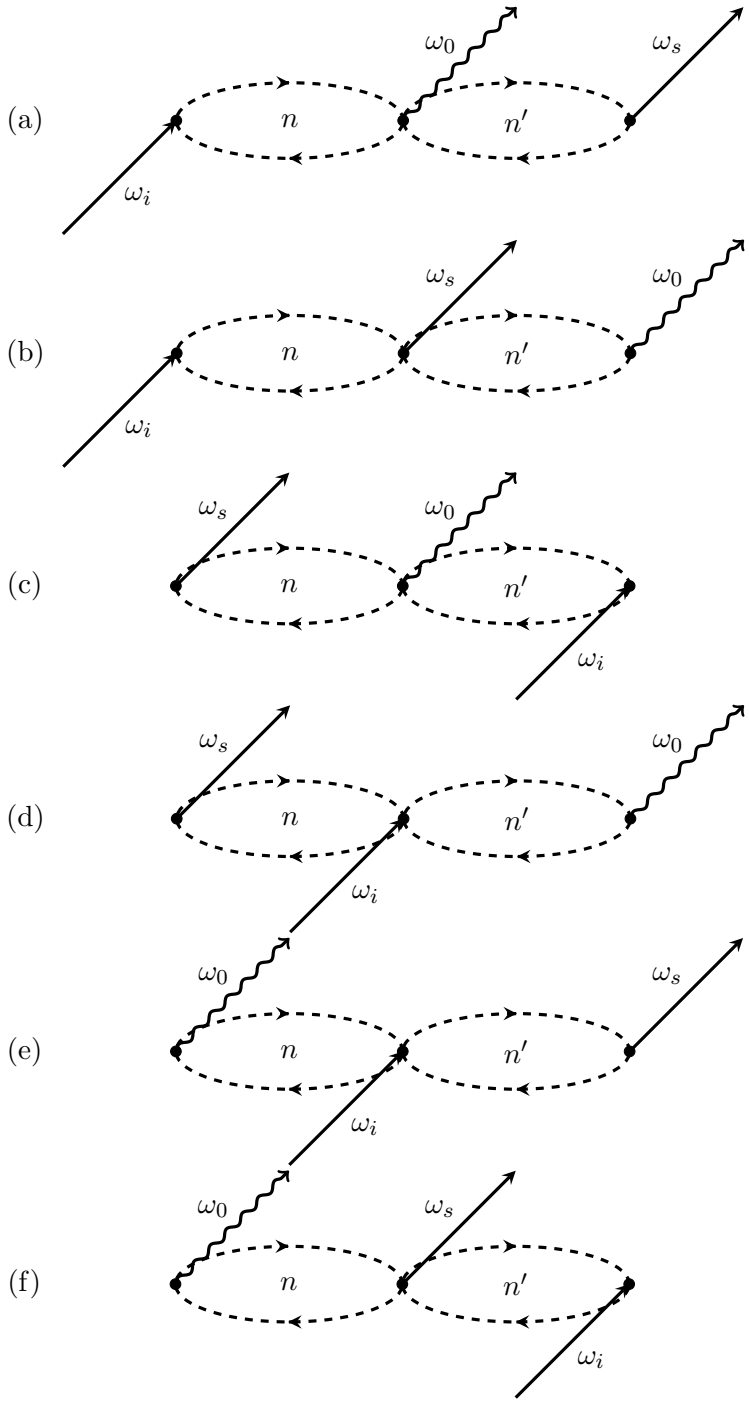

Figure 1.8: Graphical representation of the six scattering processes contribunting to the first order Raman (Stokes) scattering[79].

cial for the mathematical expression of the scattering processes. As a result, Raman scattering has no time delay, i.e. $\Delta t = 0$ (neglecting the uncertainty relations).
These three processes can take place in any time order giving rise to in total six transition processes which together form the Raman scattering process.[88] This, at first, little intuitive result derives from the perturbation theory, as demonstrated for example by Ganguly and Birman[89]. The Raman scattering probability P_{Raman} is thus the sum of all possible processes, as expressed in Eq. 1.20[79,89–91]. Fig. 1.8 illustrates the terms of Eq. 1.20.
The frequencies ω_I, ω_S and ω_0 of the incident light, scattered light and created excitation, respectively, are given such that a positive frequency denotes the creation and a negative frequency the destruction of the corresponding particle. Hamiltonians $H_{eR}(\omega_i)$ and $H_{eR}(\omega_s)$ describe the electron-radiation interaction and H_{eEx} electron-excitation interaction. P_{Raman} is the quantum-mechanical expression of the macroscopic term in Eq. 1.19. The polarization of incident and scattered light, $\boldsymbol{e}_I$ and $\boldsymbol{e}_S$ (Eq. 1.16 and 1.19), are included in the electron-radiation interaction terms, $\langle 0|H_{eR}(\omega_I)|n\rangle$ and $\langle n'|H_{eR}(\omega_S)|0\rangle$, respectively. It is summed over all the intermediate states $|n\rangle$ and $|n'\rangle$ of the system.

Second-order Raman scattering

The second-order Raman scattering is given by the emission of two excitations during the scattering process. Perturbation theory reveals that the second-order process consists of three main types of processes illustrated in Fig. 1.9. (a) The first process consists of the absorption of the incident photon under the creation of an exciton. The exciton is scattered into a different excitonic state under the simultaneous creation of two excitations. Finally, the exciton is annihilated emitting a the scattered photon. In comparison, process (b) consists of the creation of two excitations separately. An excitation is created by scattering the exciton n_1 into the state n_2, followed by the creation of a second excitation. Process (c) occurs by iteration of the first-order process. Two first-order-like processes are mediated by a virtual photon or phonon that occurs with the absorption of the incident photon, the separate emission of the two excitations and the emission of the scattered photon. In correspondence to the first-order process, the transition probability is given by the sum over the permutations of processes (a), (b) and (c). Therefore, the process (a) gives rise to six terms, (b) to 24 terms and process (c) contributes 36 terms to the Raman tensor.[80,89,92] As mentioned

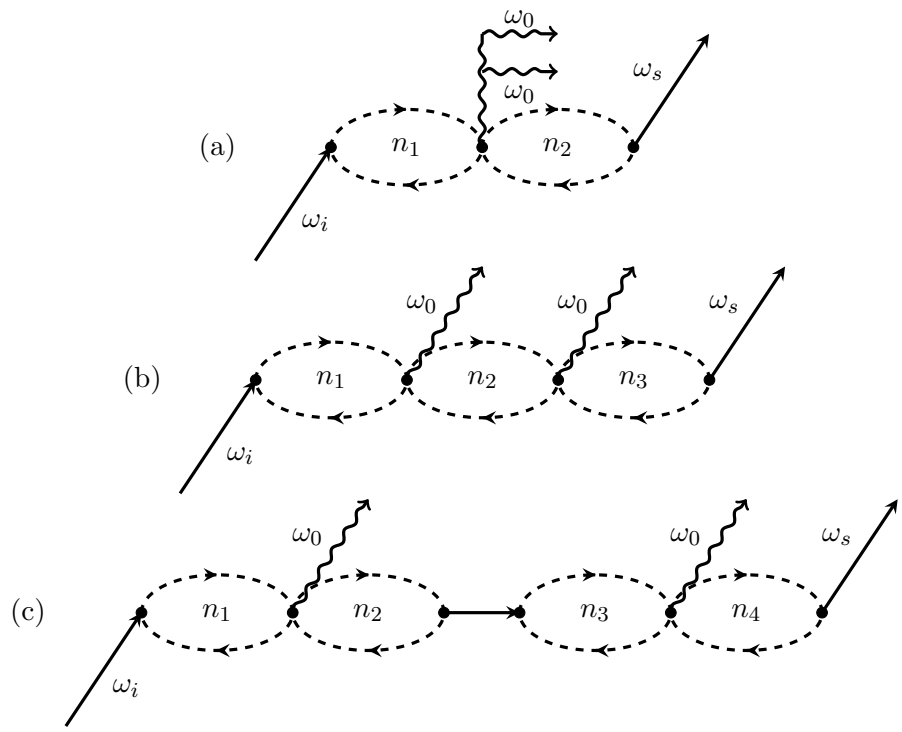

Figure 1.9: Graphical representation for second order processes. (a) Simultaneous emission of two excitations. (b) Separate emission of two excitations. (c) Separate emission of two excitations mediated by a virtual photon.

earlier (see section 1.2.1), for the second-order Raman effect, excitations of all wavevectors are allowed as long as the two excitations satisfy Eq. 1.15. [89] This includes also combinations of Stokes and anti-Stokes scattering. [80]

Resonant Raman scattering

So far we have only considered energies of incident and scattered light substantially smaller than any electronic transitions of the system. If the laser energy is tuned to the proximity of an electronic transition, it has a significant impact on the scattering probability. For $\hbar\omega_{I/S} \rightarrow E_n - E_0$ the denominators of certain scattering processes approach zero. Thus the scattering probability increases dramatically. This effect is called *resonant Raman scattering*. The resonant Raman effect in crystals has been extensively discussed by Scott, Cardona, Martin and others primarily in classical semiconductors, see for example Ref. 76,77,81,92–94.

At first, the resonant Raman effect of the first-order scattering shall be discussed by evaluating Eq. 1.20. For $\hbar\omega_I = E_n - E_0$, term (a) in Eq. 1.20

becomes dominant, since it is the only term, where both parts of the denominator approach zero for sufficiently small ω_0 and equivalence of the intermediate states n and n'. In principle the terms (b) and (e) lead to a resonant effect as well, but show only single resonance. The summation over all electronic levels n and n' can be neglected because the electronic state, that causes the resonance, is largely dominating the transition probability. The transition probability can then be expressed by

$$P_{\text{resonant-Raman}} \approx \delta(\hbar\omega_I - \hbar\omega_S - \hbar\omega_{ex}) \times \left| \frac{\left\langle 0 \middle| H_{eR}(\omega_I) \middle| n \right\rangle \left\langle n \middle| H_{eEx} \middle| n \right\rangle \left\langle n \middle| H_{eR}(\omega_S) \middle| 0 \right\rangle}{[\hbar\omega_I - (E_n - E_0)][\hbar\omega_I - \hbar\omega_{ex} - (E_n - E_0)]} + C \right|^2 \tag{1.21}$$

where C summarizes the remaining terms.

The most obvious consequence of resonant Raman scattering is the **strong enhancement of the scattered light intensity**. In addition, the **intensity ratios change for Raman bands stemming from different excitations** in comparison to the non-resonant state. This occurs because intensities and thus intensity ratios at non-resonant conditions are given by all six terms of Eq. 1.20 and by all possible electronic states of the system. In the resonant case the number of contributing terms is strongly reduced. Only the electronic state n defined by the resonant condition $\hbar\omega_I = E_n - E_0$ is of relevance.

In practice, strong changes in the intensity ratio are often the more obvious indication for resonant Raman scattering. Particularly, in the vicinity of an electronic band-to-band transition, Raman scattering is in competition with absorption. Strong absorption can cover the resonance effect.

The enhancement of the intensity is a continuous process and pre-resonance phenomena occur below the actual resonance energy. This is illustrated in Fig. 1.10 on the example of intensity evolutions of two vibrational excitations of CdS with increasing laser energy reported by Ralston and coworkers[95]. The intensity of the E_1(LO) band grows strongly with increasing laser energy ($\hbar\omega_I$) towards the electronic transition of the direct band gap E_{gap} = 2.58 eV. Under certain conditions, the scattering probability has been reported to vanish in pre-resonant conditions due to compensation of the different scattering processes (see Eq. 1.20). This leads to an anti-resonant behavior before the actual resonant enhancement.[95,96] This behav-

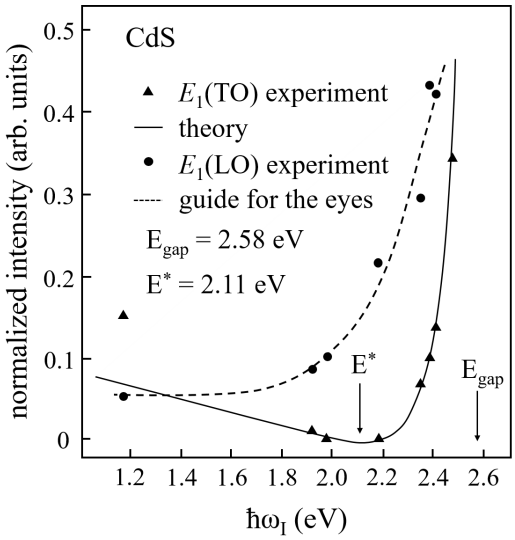

Figure 1.10: Scattered intensity of a transverse optical and a longitudinal optical E_1 mode of CdS aganist the energy of the incident laser. E_{gap} and E^* represent the energy of the band gap of CdS and the anti-resonance energy of the E_1(TO) mode. Reproduced from Ref. 95.

ior is found for the E_1(TO) mode in Fig. 1.10. The intensity of the E_1(TO) mode shows an anti-resonant behavior with a minimum $E^* = 2.11$ eV well below the electronic band gap energy, before increasing towards E_{gap}.

A Raman-active excitation is not necessarily resonant-Raman-active. With respect to the quantum mechanical terms an excitation is Raman-active if there are n, n' out of all n, n' over which is summed in Eq. 1.20 such that $P_{\text{Raman}} \neq 0$ for arbitrary ω_I. In case of resonance the summation over all n, n' is dropped. An excitation can therefore only be resonant-Raman-active if $P_{\text{resonant-Raman}} \neq 0$ for the electronic state n defined by the resonant condition $\hbar\omega_I = E_n - E_0$. As a result not all excitations may couple to specific electronic transitions and, therefore, show no resonance effect in the Raman scattering process.
In general, resonant Raman scattering enables to probe electronic transitions. **For first-order Raman scattering processes, only direct transitions can be observed**, due to the small momentum transfer (see section 1.2.1). This is illustrated in Fig. 1.11, process I (red).
On the contrary, second-order Raman scattering allows excitations of all momentum vectors $\boldsymbol{q}$. Hence, **the second-order scattering can be in res-**

onance with direct and indirect transitions, as illustrated in Fig. 1.11, process II (blue).[80,97–99]

However, the Raman shift of second-order scattering processes is difficult to assign to particular excitations, since multiple combinations of excitations can provide the necessary momentum transfer to interact with indirect transitions. An exception here are overtones of the first-order spectrum, i.e. doubly scattered first-order excitations. In direct-gap semiconductors, overtones show strong resonance behavior. Here, first- and second- (or higher-) order scattering are simultaneously resonant if the laser energy $\hbar\omega_I$ is in vicinity of the energy of direct electronic transition (see Fig. 1.11, process I (red)). Under resonant conditions overtone intensities are often higher than first-order intensities since for second- (and higher-) order scattering processes more transition terms occur and triple (or higher) resonances are possible.[80,81,93]

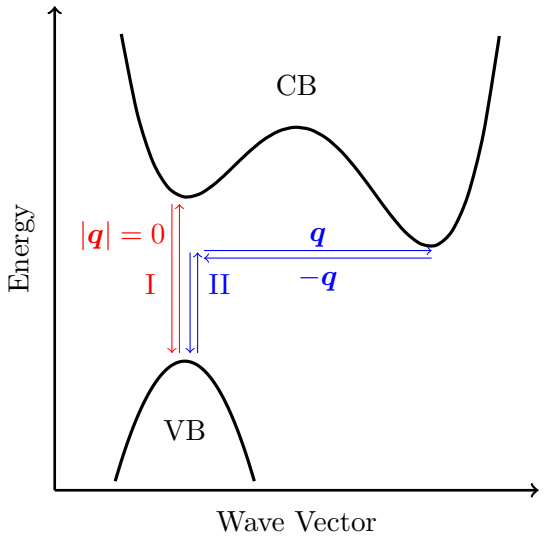

Figure 1.11: Schematic electronic band structure of an indirect semiconductor. (I) (in red) illustrates the interaction of $|\boldsymbol{q}| = 0$ resonant processes. (II) (in blue) illustrates the interaction for resonant processes with indirect electronic transitions.

1.2.4 Crystal vibrations - phonons

In the present work, Raman scattering is mainly used for the analysis of vibrational states. Therefore, in the following section an overview of crystal vibrations shall be given (following classical textbooks such as Ref. 82,100). The major concepts will be introduced without the full derivation of all formulas.
In a first step, we will focus on deriving the equations of crystal vibrations for *non-polar* vibrations, i.e. displacements which do not carry a dipole moment. In a second step, the particularities of *polar* vibrations shall be discussed. Here, it is sufficient to treat the problem classically.

Non-polar phonons

Let us consider a crystal with n atoms per unit cell. The potential V represents the energy of all atoms. This potential can be expressed as a Taylor expansion of atomic displacements around the equilibrium positions. Under the assumption of the *harmonic approximation*, the expansion is stopped after the second-order

$$V = V_0 + \sum_{\boldsymbol{R}_\alpha,\alpha,i} \left.\frac{\partial V}{\partial U^i_{\boldsymbol{R}_\alpha\alpha}}\right|_0 U^i_{\boldsymbol{R}_\alpha\alpha} + \frac{1}{2} \sum_{\boldsymbol{R}_\alpha,\boldsymbol{R}_\beta,\alpha,\beta,i,j} \left.\frac{\partial^2 V}{\partial U^i_{\boldsymbol{R}_\alpha\alpha}\partial U^j_{\boldsymbol{R}_\beta\beta}}\right|_0 U^i_{\boldsymbol{R}_\alpha\alpha} U^j_{\boldsymbol{R}_\beta\beta} \tag{1.22}$$

with displacements $\boldsymbol{U}_{\boldsymbol{R}_\alpha\alpha}$ and $\boldsymbol{U}_{\boldsymbol{R}_\beta\beta}$ for the atoms α and β with their lattice vectors $\boldsymbol{R}_\alpha$ and $\boldsymbol{R}_\beta$, respectively, where i, j run over the Cartesian components. The linear term vanishes expanding around the equilibrium position and using an appropriate normalization the constant V_0 can be set to zero, so that Eq. 1.22 becomes

$$V = \frac{1}{2} \sum_{\boldsymbol{R}_\alpha,\boldsymbol{R}_\beta,\alpha,\beta,i,j} \left.\frac{\partial^2 V}{\partial U^i_{\boldsymbol{R}_\alpha\alpha}\partial U^j_{\boldsymbol{R}_\beta\beta}}\right|_0 U^i_{\boldsymbol{R}_\alpha\alpha} U^j_{\boldsymbol{R}_\beta\beta}. \tag{1.23}$$

The potential is formally similar the harmonic oscillator. Thus, we define the force constants as

$$A^{ij}_{\boldsymbol{R}_\alpha\boldsymbol{R}_\beta\alpha\beta} = \left.\frac{\partial^2 V}{\partial U^i_{\boldsymbol{R}_\alpha\alpha}\partial U^j_{\boldsymbol{R}_\beta\beta}}\right|_0 . \tag{1.24}$$

The equation of motion for the atom α of the mass M_α under the influence of the displacement of the other atoms in the unit cell (including itself) is

therefore given by

$$M_\alpha \ddot{U}^i_{\boldsymbol{R}_\alpha \alpha} = -\sum_{\boldsymbol{R}_\beta \beta} A^{ij}_{\boldsymbol{R}_\alpha \boldsymbol{R}_\beta \alpha\beta} U^j_\beta. \tag{1.25}$$

The vibrations of the entire lattice are described by $3n$ coupled differential equations. To simplify Eq. 1.25 we introduce mass-weighted coordinates for the displacement and the force constants

$$\begin{aligned} \boldsymbol{w}_{\boldsymbol{R}_\alpha \alpha} =& M_\alpha \boldsymbol{U}_\alpha \\ \overline{A}^{ij}_{\boldsymbol{R}_\alpha \boldsymbol{R}_\beta \alpha\beta} =& A^{ij}_{\boldsymbol{R}_\alpha \boldsymbol{R}_\beta \alpha\beta} (M_\alpha M_\beta)^{-1/2}. \end{aligned} \tag{1.26}$$

Thus, Eq. 1.25 becomes

$$\ddot{w}^i_{\boldsymbol{R}_\alpha \alpha} = -\sum_{\boldsymbol{R}_\beta \beta} \overline{A}^{ij}_{\boldsymbol{R}_\alpha \boldsymbol{R}_\beta \alpha\beta} w^j_{\boldsymbol{R}_\beta \beta}. \tag{1.27}$$

$\overline{A}^{ij}_{\boldsymbol{R}_\alpha \boldsymbol{R}_\beta \alpha\beta}$ possesses translational symmetry. Therefore, the absolute position of the atom in the crystal is not of importance, but only the relative position between the atoms. This allows to introduce a relative vector $\boldsymbol{R'} = \boldsymbol{R}_\alpha - \boldsymbol{R}_\beta$. Furthermore, the displacements can be expressed as Bloch functions as

$$w^i_{\boldsymbol{R}_\alpha \alpha} = v^i_\alpha e^{-i[\omega t - \boldsymbol{q}\boldsymbol{R}]} \tag{1.28}$$

with the oscillation frequency ω, the wavevector $\boldsymbol{q}$ and the amplitude $\boldsymbol{v}$, so that Eq. 1.27 becomes

$$\omega^2 v^i_\alpha = \sum_\beta \left[\sum_{\boldsymbol{R'}} \overline{A}^{ij}_{\boldsymbol{R'} \alpha\beta} e^{i\boldsymbol{q}\boldsymbol{R'}} \right] v^j_\beta = \sum_\beta D^{ij}_{\alpha\beta}(\boldsymbol{q}) v^j_\beta. \tag{1.29}$$

$D^{ij}_{\alpha\beta}(\boldsymbol{q})$ is referred to as the *dynamical matrix* containing all information to describe the vibrations of the crystal. Eq. 1.29 can be written as

$$\sum_\beta \left[D^{ij}_{\alpha\beta}(\boldsymbol{q}) - \omega^2 \delta_{\alpha\beta} \right] v^j_\beta = 0 \tag{1.30}$$

This equation system has only non-trivial solutions if the determinant vanishes:

$$\det \left| D^{ij}_{\alpha\beta}(\boldsymbol{q}) - \omega^2 \delta_{\alpha\beta} \right| = 0 \tag{1.31}$$

The eigenfrequncies ω are the vibration frequencies of the system. The relation between ω and the momentum $\boldsymbol{q}$ is called *dispersion relation*. Once the eigenfrequencies ω are known the amplitudes v_α can be calculated. The

actual vibrational patterns corresponding to the eigenfrequencies are the *normal modes* $\boldsymbol{W}_\sigma$ which are given as a linear combination of the displacements of single atoms $\boldsymbol{w}_\alpha$:

$$W^i_\sigma(\boldsymbol{q}) = \sum_\alpha c^i_{\alpha\sigma}(\boldsymbol{q}) w^i_\alpha \tag{1.32}$$

where $c^i_{\alpha\sigma}$ are transformation coefficients and $\sigma(= 1, 2, ..., 3n)$ is the branch index that distinguishes different solutions of the equations. These *normal modes* diagonalize the equations of motion and thus, decouple the equations of motion into $3n$ non-interacting collective motions:

$$\ddot{\boldsymbol{W}}_\sigma + \omega^2_\sigma \boldsymbol{W}_\sigma = 0 \tag{1.33}$$

In every system the branches of the normal modes are divided into three *acoustic* branches with $\omega(\boldsymbol{q} = 0) = 0$ and $3n - 3$ *optical* branches with $\omega(\boldsymbol{q} = 0) \neq 0$. The acoustic modes represent at $\boldsymbol{q} = 0$ the displacement of the entire unit cell and thus, a hypothetical displacement of the entire crystal along the three axes. Fig. 1.12 illustrates the dispersion relation for an acoustic and an optical branch. The collective vibrations can be classified as *longitudinal* or *transverse* according to whether the displacement is parallel or perpendicular, respectively, to the propagation direction $\boldsymbol{q}$ of the vibration mode.

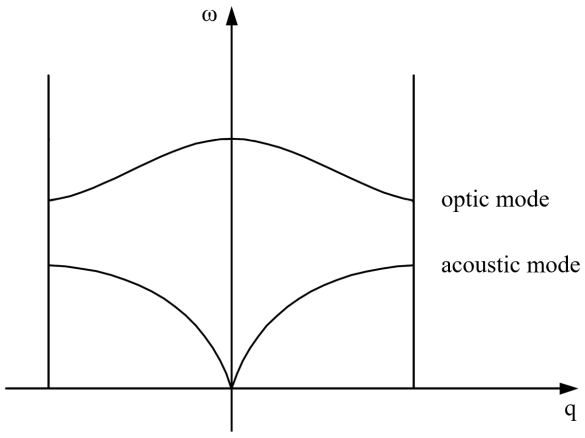

Figure 1.12: Schematic dispersion relation for an acoustic and an optical branch within the first Brillouin zone. The straight lines indicate the boundaries of first the Brillouin zone.

To clarify the terminology used hereafter, a *crystal vibration* is a collective, displacive excitation of the atoms of the crystal. In quantum mechanical description this excitation state is termed *phonon*, a quantum mechanical quasi-particle. In the following, both terms are used synonymically.

In order to probe a crystal vibration by Raman spectroscopy, Eq. 1.11 has to be fulfilled. I.e. the vibrational displacement alters the dielectric susceptibility. Group theoretical rules allow to determine the Raman-active vibrations modes[82,85].
A centro-symmetric crystal and its tensor properties remain unchanged under inversion. This is only the case for an vibration mode with even parity which does not change sign under inversion. A mode of odd parity changes sign under inversion, thus, χ_1 changes sign. Therefore, the Raman tensor for an odd-parity mode vanishes. On the contrary, only odd-parity modes change their dipole moment and, hence, are infrared-active. This correlation is known as *rule of mutual exclusion* of infrared and Raman-active vibrations in centro-symmetric materials[79]. If an atom occupies an inversion center in the crystal structure, any vibration including this atom is of odd parity. In turn, all vibration modes involving the displacement of an atom occupying an inversion center are Raman-inactive. An extreme case is cubic Perovskite structure $Pm\bar{3}m$. Here, all atoms occupy inversion centers. Therefore, none of the vibration modes are Raman-active. Modes which are neither Raman nor infrared active are said to be *silent*.
In the present work, excitation symmetries of vibrational excitations are given in Mulliken's notation[101,102]. The symbol A denotes a fully symmetric vibration, B an anti-symmetric vibration and E and T indicate doubly and triply degenerated vibrations, respectively. *g*, *u*, *1*, *2*, *3* are subscripts to A, B, E and T. *1*, *2*, *3* define the axis and mirror planes to which the excitations are symmetric. Subscripts g and u denote displacements of even parity and odd parity with respect to a inversion center. Hence, these notations only exist for centro-symmetric crystals.

Polar vibrations and oblique modes

So far we only considered non-polar modes. Polar vibrational modes, i.e. vibrations that carry an electric-dipole moment, show different properties. Here, the vibration is accompanied by an electric field induced by the dipole moment. Therefore, the equation of motion needs to be solved for the vibration and the electric field. As consequence the equation of motion Eq. 1.33 becomes (the derivation can be found in Hayes and Loudon[82])

$$\ddot{\boldsymbol{W}}_\sigma + \omega_\sigma^2 \boldsymbol{W}_\sigma = \frac{Z_\sigma(\boldsymbol{q}\cdot\boldsymbol{\xi}_\sigma)\sum_\tau Z_\tau(\boldsymbol{q}\cdot\boldsymbol{\xi}_\tau)\boldsymbol{W}_\tau}{V\epsilon_0 \sum_{ij} q^i \epsilon_\infty^{ij} q^j}. \tag{1.34}$$

Z_σ is the *effective charge* and $\boldsymbol{\xi}_\sigma$ the unity vector parallel to the electrical field of the vibration σ. V stands for the volume of the primitive cell and ϵ_∞ for the dielectric tensor. τ runs over all polar modes.
We find that the vibrational frequency changes due to the influence of the electric field. For non-polar modes the effective charge vanishes ($Z_\sigma = 0$), the right-hand side of 1.34 becomes zero and Eq. 1.34 turns into 1.33. If the mode is polar ($Z_\sigma \neq 0$), the vibration frequency ω_σ of the polar mode depends on the angle between propagation direction of the mode $\boldsymbol{q}$ and the vector $\boldsymbol{\xi}_\sigma$ along the electric field of the vibration. The scalar product $(\boldsymbol{q}\cdot\boldsymbol{\xi}_\sigma)$ becomes maximal for a longitudinal wave when $\boldsymbol{q} \parallel \boldsymbol{\xi}_\sigma$ and zero for transversal modes ($\boldsymbol{q} \perp \boldsymbol{\xi}_\sigma$) with $\boldsymbol{q}\cdot\boldsymbol{\xi}_\sigma = 0$. Transversal modes have no associated electric field. The appearance of all polar modes in Eq. 1.34, since we sum over all polar displacements τ, shows that the frequency of the polar mode σ is not only affected by its own electric field but also by the electric fields of other polar modes of the system.

In the following, we discuss the limiting cases of the transformation from longitudinal to transversal modes under changing propagation direction $\boldsymbol{q}$. Here, we shall concentrate on uniaxial systems as it will be of need in chapter 5.
For uniaxial crystals, where x and y are the ordinary and z is the extraordinary axes, we consider a group of three polar vibrations, each along one direction. The subscripts $\parallel$ and $\perp$ indicate parallel or perpendicular displacements with respect to the extraordinary axis. The superscripts l and t stand for longitudinal and transversal wave propagation with respect to the electric field direction. The anisotropy of the crystal structure leads to an anisotropy of the force constants along the ordinary and extraordinary axes. Therefore, the vibration frequencies without associated electric-field

for the displacement along z-axis $\omega_{\parallel}^{t}$, and in the x-y plane $\omega_{\perp}^{t}$ are different. The vibrations along x- and y-direction are degenerated. For the evolution of the mode frequency with changing angle between the electric field $\boldsymbol{E}$ and the propagation direction $\boldsymbol{q}$, it is important whether the anisotropy of the force constants is strong compared to the addition of the electric field or not. In the following, we discuss these two limiting cases. For that we assign the vibrational symmetry A to the vibrations $\omega_{\parallel}^{l}$ and $\omega_{\parallel}^{t}$ and E to $\omega_{\perp}^{t}$ and $\omega_{\perp}^{l}$.
i) At first we assume the *anisotropy of the force constants to be large* compared to the effect of the electric field of the polar mode:

$$\left|\omega_{\parallel} - \omega_{\perp}\right| \gg \left|\omega_{\parallel}^{l} - \omega_{\parallel}^{t}\right| \text{ and } \left|\omega_{\perp}^{l} - \omega_{\perp}^{t}\right|$$

The frequencies ω as a function of the angle θ between the propagation direction and the electric field can be approximated as[90]:

$$\text{Upper extraordinary branch}: \quad \omega^2(\theta) = {\omega_{\parallel}^{t}}^2 \sin^2\theta + {\omega_{\parallel}^{l}}^2 \cos^2\theta \qquad (1.35)$$

$$\text{Lower extraordinary branch}: \quad \omega^2(\theta) = {\omega_{\perp}^{t}}^2 \cos^2\theta + {\omega_{\perp}^{l}}^2 \sin^2\theta \qquad (1.36)$$

The term extraordinary branch determines a frequency branch changing with the orientation in contrast to an ordinary frequency branch showing no effect for varying orientation. The frequency evolutions for changing θ are illustrated in Fig. 1.13. For $\theta = 0°$ the frequency of the upper branch is $\omega_{\parallel}^{l}$ with the symmetry A. For increasing θ, the vibration changes from longitudinal to transversal, thus, from a higher frequency $\omega_{\parallel}^{l}$ to a lower frequency $\omega_{\parallel}^{t}$ with no associated electric field. The frequency of the lower branch is degenerated at $\theta = 0°$. As the angle θ increases the degeneracy is lifted and the vibration branch splits in an ordinary and an extraordinary one. The frequency $\omega_{\perp}^{t}$ and the symmetry E of the ordinary branch remain independent of the orientation. Whereas the extraordinary branch changes from transversal to longitudinal for $\theta = 90°$ with the symmetry being E for $\theta = 0°$ and 90°. The extraordinary branches have strictly no simple polarization and symmetry for intermediate angles θ. However, since the anisotropy of the force constants is stronger than the effect of the electric field, displacement corresponding to the upper extraordinary branch can be regarded as parallel to the z-axis and the displacement of the lower extraordinary branch as perpendicular to the z-axis.[90]

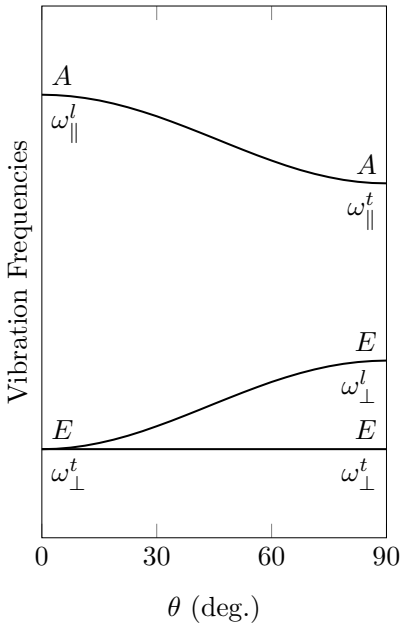

Figure 1.13: Evolution of band position of polar modes of an uniaxial crystal against the angle between polarization and phonon propagation direction for the limiting case where the anisotropy of the force constants are *large* compared to the effect of the electric field of the polar mode.[82]

ii) In the second case the *anisotropy of the force constants is small* in comparison to the frequency difference of transversal and longitudinal vibrations caused by the electric field:

$$\left|\omega_{\parallel} - \omega_{\perp}\right| \ll \left|\omega_{\parallel}^{l} - \omega_{\parallel}^{t}\right| \text{ and } \left|\omega_{\perp}^{l} - \omega_{\perp}^{t}\right|$$

The frequency dependence on the angle θ is given by:

$$\text{Upper extraordinary branch}: \quad \omega^2(\theta) = {\omega_{\parallel}^{l}}^2 \cos^2\theta + {\omega_{\perp}^{l}}^2 \sin^2\theta \tag{1.37}$$

$$\text{Lower extraordinary branch}: \quad \omega^2(\theta) = {\omega_{\parallel}^{t}}^2 \sin^2\theta + {\omega_{\perp}^{t}}^2 \cos^2\theta \tag{1.38}$$

Fig. 1.14 illustrates the frequency behavior of Eqs. 1.37 and 1.38. The upper extraordinary branch represents a longitudinal vibration mode for the angles $\theta = 0°$ and $90°$, while the vibrational pattern changes from parallel to perpendicular to the z-axis. For the lower extraordinary branch we face the reverse situation. $\theta = 0°$ and $90°$ leads to a transversal mode, but symmetry and vibrational pattern change from E and perpendicular to the x-axis to A and parallel to the x-axis. Apart from the extreme cases of

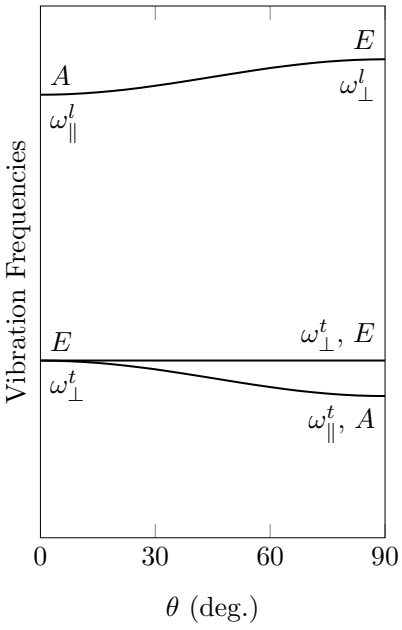

Figure 1.14: Evolution of band position of polar modes of an uniaxial crystal against the angle between polarization and phonon propagation direction for the limiting case where the anisotropy of the force constants are *small* compared to the effect of the electric field of the polar mode.[82]

$\theta = 0°$ and 90°, there is no simple polarization, but since the impact of the electric field of the mode is more important than the anisotropy of the force constants, the vibration modes can be regarded as longitudinal and transversal, respectively. The vibrational pattern and the symmetry, on the other hand, change crucially for intermediate angle θ.
The vibrational modes of intermediate angle θ between electric field and propagation direction of the polar mode are called *mixed* or *oblique modes*. Due to the mixed states of symmetry, vibrational pattern and polarization, the analysis of oblique modes is difficult from an experimental and theoretical point of view. In particular, in powder samples of polar materials where all possible crystalline orientations are present, Raman bands tend to become very broad and single band analyses are impossible.

A particularly interesting example of mode mixing is α-quartz, reported by Shapiro and Axe[103]. Both above-discussed critical cases are present in α-quartz. The point group 32 gives rise to vibrational modes of A_1, A_2 and E symmetry. Here, the A_1 modes are non-polar, thus, do not interact with other polar modes. The A_2 modes are polar but Raman-inactive, whereas the modes of E symmetry are polar and Raman-active. Fig. 1.15 shows the

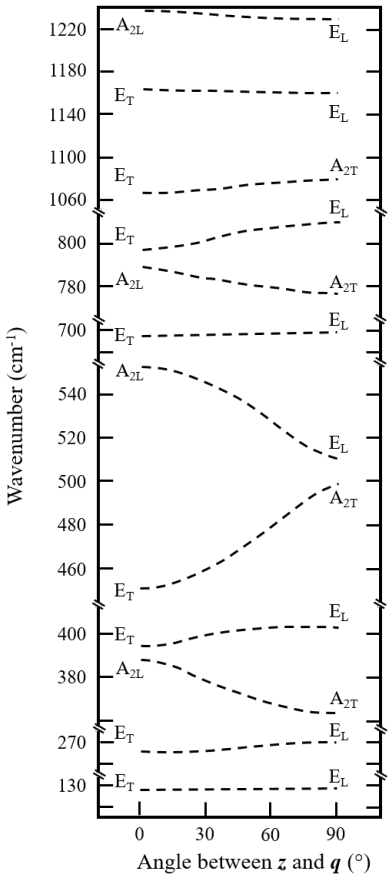

Figure 1.15: Oblique mode evolution of quartz. Reproduced from Ref. 103.

Raman mode evolution for changing propagation directions. A set of vibrational modes of A_2 and E symmetry where the electric field contribution is more important than the anisotropy of the force constants behaves according to case ii) discussed above. For an angle $\theta = 0°$ the two extraordinary branches are of E(T) and A_2(L) symmetry, where T stands for transversal and L of longitudinal. For $\theta = 90°$ the E(T) mode changed into an A_2(T) mode and the A_2(L) into an E(L) mode. In these extreme cases only the E mode is observable by Raman spectroscopy. For intermediate values of θ the symmetries mix and the bands become Raman-active and the intensities increase with the increasing contribution of the E mode. In case of predominant anisotropy of force constants over the electric-field contribution, the symmetries of the extrema of the extraordinary branches are A_2(L) and A_2(T) for one and E(T) and E(L) for the other branch. While the branch

of mainly E symmetry is observable for any value θ, the vibrations of the A_2-symmetry branch are Raman-inactive for $\theta = 0°$ and 90°. However, for intermediate angle θ the symmetries mix also with other E modes and the vibrations become Raman-active[103]. This case demonstrates that oblique modes possess strongly mixed character changing significantly the interaction and observation properties compared to their un-mixed, "parental" vibrational modes, and thus, illustrates the complexity of analyzing *oblique modes*.

In addition, the intensity is strongly affected by the contribution of electric field that accompanies a polar vibration mode. The linear susceptibility of the crystal is perturbed by the electric field and the total Stokes polarization becomes[82]

$$P_S^i = \sum_{\sigma,j,h,k} \left(a_\sigma^{ij} W_\sigma^k E_I^j + b^{ijh} E^h E_I^j \right) \tag{1.39}$$

where

$$b^{ijh} = \epsilon_0 \frac{\partial \chi^{ij}(\omega_I)}{\partial E^h} \text{ and } a_\sigma^{ij} = \frac{\partial \chi^{ij}(\omega_I)}{\partial W_\sigma^k} \tag{1.40}$$

describe the modulation of the susceptibility by the electric field accompanying the polar mode and by the vibrational displacement, respectively (see section 1.2.1). The contribution to the intensity arising from the electric field of a polar mode can be significant. In analogy to the vibration frequency of a the polar mode (see Eq. 1.34) the intensity depends not only on the perturbation of the electric susceptibility by the electric field of one polar mode but is effected by the perturbation of the electric susceptibility of all polar modes[82]. This crosstalk makes the intensity analysis of polar modes particularly difficult.

1.2.5 Soft modes in Landau theory of phase transitions

In this section, we briefly explain the basics of soft mode spectroscopy for structural changes.
As we have seen in section 1.1.1, distortions may lead to new structures of lower symmetry in comparison to the ideal cubic perovskite structure $Pm\overline{3}m$. By changing external parameters, like temperature, pressure or strain, as well as substituting elements, it is possible to change the structure of a material. Here, we are interested in phase transitions that are accompanied with a change in symmetry where the structure changes from a state of higher symmetry to a state of lower symmetry. This can either happen in an abrupt way, first-order phase transition, or in a continuous manner, second-order phase transition. For first-order phase transitions the two structures on either side of the transition do not have a predictable symmetry relation. By contrast, in second-order phase transitions the lower symmetry group is a subgroup of the higher symmetry group.
Landau theory of phase transitions allows to describe these kind of phase transitions. A basic idea of Landau theory is to consider a quantity, the so-called *order parameter*, directly linked to the change of the system related to the phase transition. The equilibrium state of this quantity minimizes the *free energy* $F(T, p, \eta)$ of the system where T and p represent temperature and pressure, and η the *order parameter*.
As an example serves the phase transition of strontium titanate. $SrTiO_3$ is cubic at room temperature crystallizing in the space group $Pm\overline{3}m$. At 106 K a phase transition occurs. The tilt system changes from the cubic perovskite type $a^0a^0a^0$ to $a^0a^0c^-$ given rise to the space group $I4/mcm$ as we can find in Fig. 1.3. In the low temperature phase, the octahedra are rotated around the z-axis such that two subsequent octahedra are rotated in anti-phase. The octahedra tilt angle can be considered as order parameter of the phase transition being zero in the high temperature phase and increasing below the phase transition temperature.
We can assume η to be small in the vicinity of the phase transition and develop $F(T, p, \eta)$ in a Taylor expansion of η:

$$F = F_0 + A_1\eta + \frac{1}{2}A_2\eta^2 + \frac{1}{3}A_3\eta^3 + \frac{1}{4}A_4\eta^4 + ... \tag{1.41}$$

For symmetry reasons, terms to an odd power of η vanish and A_4 is required to be positive:

$$F = F_0 + \frac{1}{2}A_2\eta^2 + \frac{1}{4}A_4\eta^4 \tag{1.42}$$

$F(T, p, \eta)$ is required to be in an equilibrium state with respect to η. The equilibrium values are defined by:

$$\frac{\partial F}{\partial \eta} = 0 \tag{1.43}$$

with the stability condition:

$$\frac{\partial^2 F}{\partial \eta^2} > 0. \tag{1.44}$$

The stable states are

$$\eta = 0 \qquad \text{for } A_2 \geq 0 \tag{1.45}$$

$$\eta = \pm\sqrt{-\frac{A_2}{A_4}} \qquad \text{for } A_2 < 0 \tag{1.46}$$

For temperature driven phase transitions, where the high temperature phase is of higher symmetry than the low temperature phase, it is customary to assume A_2 to be of the form[64]

$$A_2 = A_{2,0}(T - T_c) \tag{1.47}$$

where T_c is the transition temperature, such that

$$\eta = 0 \qquad \text{for } T \geq T_c \tag{1.48}$$

$$\eta = \pm\sqrt{-\frac{A_{2,0}(T - T_c)}{C}} \qquad \text{for } T < T_c \tag{1.49}$$

This dependence of the free energy on the order parameter is illustrated in Fig. 1.16.

Phase transitions can be characterized by vibrational modes that change substantially in frequency when approaching the transition temperature. These vibrations are termed unstable or *soft modes*[64]. The expression "*soft*" refers to the strong changes of the vibration frequency in the vicinity of the phase transition, in contrast to *hard modes* with less prominent frequency changes. The vibrational patterns of soft modes are commonly closely related to the structural changes at the phase transition. In the example of the tetragonal-to-cubic phase transition of $SrTiO_3$, the vibrational displacement of the soft modes represents an octahedra rotation movement.
To investigate the frequency evolution of the soft mode when approaching the phase transition, we regard F in Eq. 1.41 as the potential of a

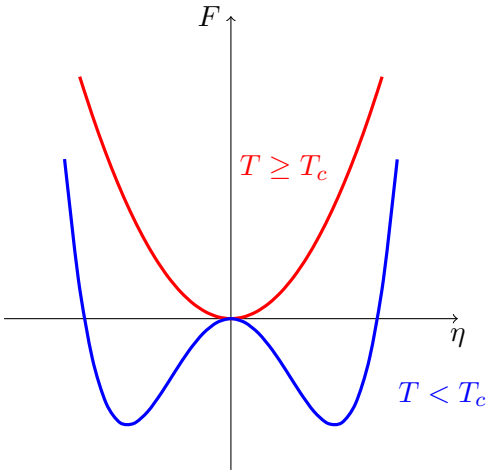

Figure 1.16: Free energy F against the order parameter η for temperatures $T \geq T_c$ (red) and $T < T_c$ (blue) where T_c determines the temperature of the phase transition.

one-dimensional oscillator expanded in η in harmonic approximation, thus that[64,82]:

$$\frac{\partial^2 F}{\partial \eta^2} = m\omega^2 = A_2 \tag{1.50}$$

where ω is the soft mode frequency and m the mass of the contributing atoms. With Eq 1.47, the soft mode frequency is given as[64,82]:

$$\omega = \text{const.} \, |T - T_c|^{1/2} \, . \tag{1.51}$$

Comparing Eq. 1.51 with 1.48 we find that the order parameter is proportional to the frequency of the corresponding soft mode for temperature-driven phase-transitions: $\eta_i \propto \omega_i$.
The soft mode frequency evolution towards the phase transition in Eq. 1.51 indicates that the soft mode frequency goes to zero at the transition temperature T_c. This behaviour is illustrated in Fig. 1.17. The low lying A_{1g} and E_g modes represent the soft modes of $SrTiO_3$. Approaching the phase transition from the low symmetry phase both modes soften to zero at T_c.

An order parameter may give rise to several soft modes which do not necessarily need to be Raman-active. In Fig. 1.17, the Raman-active soft modes are shown. However, in the higher symmetry phase the soft-mode is not Raman-active (and in fact is not at the Γ-point but at the R-point), but is re-increasing in the cubic phase, as can be followed by inelastic neutron scattering. On the other hand, in the low symmetry phase at least one

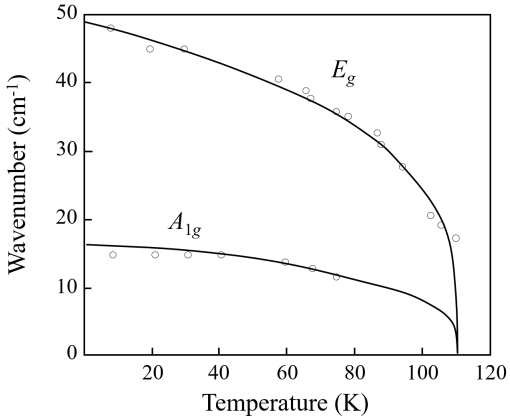

Figure 1.17: Evolution of the A_{1g} and E_g soft modes of $SrTiO_3$ towards the phase transition. Reproduced from Ref. 104.

Raman-active soft mode of A symmetry exists as by Birman[105] and Shigenari[106].

1.2.6 Probing magnetism by Raman scattering

In this section, we shall briefly introduce two possibilities to probe magnetism and magnetic effects by Raman scattering.
A direct way to probe magnetism of a material by Raman spectroscopy is the scattering on magnetic excitations. Magnetic excitations, also called magnons, can be understood as fluctuations of the magnetic spin system. The inelastic scattering on magnetic excitations follows essentially the general rules as described in chapter 1.2.1-1.2.3. However, the spin-orbit coupling of the magnetic material is important, since the cross section scales directly with the strength of the spin-orbit splitting. I.e. small spin-orbit splitting leads to weak scattering intensities.
Magnon frequencies of ferromagnetic materials are commonly too low for Raman scattering experiments. In contrast anti-ferromagnetic materials possess magnetic excitation frequencies in the accessible range[82].
In equivalence to phonon scattering, multiple magnetic excitations scattering is also possible. However, the scattering intensity can be higher in comparison to higher-order phonon scattering.
Magnetism can be indirectly probed by analyzing the effect of the ordering of the magnetic moments on the structure. The alignment of spins at a magnetic phase transition induces a strain in the material, magnetostriction. By this means the magnetic system influences the crystalline lattice and thus couples to the phonon system. This allows an indirect probing of the magnetic ordering. The interaction between vibrational frequency and the magnetic moments is commonly assumed as

$$\omega_{\mathrm{sp}} = \omega_0 + \gamma \langle \boldsymbol{S}_i \boldsymbol{S}_j \rangle \tag{1.52}$$

where ω_{sp}, ω_0, γ, $\boldsymbol{S}_{i/j}$ are the frequency due to interaction with the spin moments, the undisturbed frequency, the coupling constant and the spin moment for different spins i and j[107].

Chapter 2

Experimental methods

2.1 Raman spectroscopy

The Raman scattering effect has been discussed in the previous chapter. Here, the Raman spectroscopy setup, the measurement environment and corrections of the measured spectra is addressed.

2.1.1 Experimental setup

The Raman measurements at the Luxembourg Institute of Science and Technology were performed on a Renishaw inVia Reflex Raman Microscope. A sketch of the setup is shown in Fig. 2.1. The monochromatic light beam is provided by four different sources depending on the designated wavelength: a solid state diode (785 nm), a helium-neon (633 nm), a frequency doubled Nd:YAG (532 nm) and a helium-cadmium laser (325 / 442 nm). Raman spectra are recorded in backscattering geometry. The Rayleigh peak is filtered with spectral cut-offs at 60 cm^{-1} (infrared), 350 cm^{-1} (UV), 70 cm^{-1} (red), 80 cm^{-1} (green) or 95 cm^{-1} (blue). In addition, low frequency filters are available for the 532 and 633 nm laser lines allowing to record Raman features down to 10 cm^{-1}. The laser beam is focused via an optical Leica microscope on the sample. The microscope is equipped with interchangeable optical lenses providing magnifications/numerical apertures of $\times$5/0.12, $\times$20/0.4, $\times$50/0.75 and $\times$100/0.85 for visible light and $\times$15/0.32 and $\times$40/0.5 for UV light. Long distance objectives ($\times$20/0.4 and $\times$50/0.5) allow temperature dependent measurements. The lateral resolution is given by the spot size, determined from the wavelength and the properties of the objective, typically of the order of 1 µm. An optical camera included in the

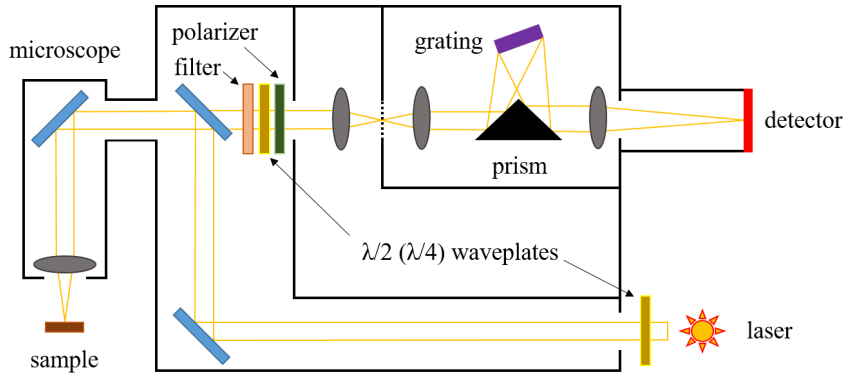

Figure 2.1: Sketch of the Renishaw inVia confocal Raman microscope.

optical microscope enables to visualize the surface and optimize the focus point. Light scattered by the sample takes the same light path as the incident light. After filtering of the Rayleigh peak, an optical grating disperses the scattered light for spectral analysis. The signal is detected by a CCD (charged-coupled device) with a spectral resolution of 2 cm^{-1} to 0.4 cm^{-1} depending on the grating and wavelength of the laser line (gratings: 1200, 1800 and 2400 grooves per mm). The detector is directly connected to a computer for data processing and analysis.
The polarization of the laser can be rotated by 90°. The polarization of the analyzed light can be chosen parallel or perpendicular to the polarization direction of the laser beam. For visible light, the Raman microscope has a built-in silicon sample for calibration of the frequency. For measurements under UV-light, a diamond is used for calibration.

2.1.2 Porto's notation

We have seen in chapter 1.2 that the orientation of the crystal with respect the polarization and propagation direction of the incident and scattered laser light is crucial for the correct interpretation of the acquired spectra. S.P.S. Porto introduced in 1966 a notation that allows to describe the scattering geometry:[108]

$$A(BC)D \tag{2.1}$$

where A and D are the directions of propagation, and B and C are the directions of polarization of the incident and scattered laser light, respectively. In a backscattering geometry, an overline indicates that the incident and analyzed light propagate in opposite directions, e.g. $A(BC)\overline{A}$. The directions

A–D are usually given with respect to axes linked to the spectrometer. If the crystal orientation is known, they can be expressed in a suitable crystallographic system, and directly used for application of the Raman selection rules and determination of the mode symmetries.

2.1.3 Corrections of the Raman spectrum

The scattered light intensity depends on external factors such as temperatures, response of the spectrometer or scattering volume of the sample. If the investigations involve the scattered intensities, the Raman spectra need to be corrected against these factors.

Thermal occupation factor

The intensity in Eq. 1.16 depends on the Bose-Einstein thermal occupation factor $n(\omega)$:

$$n(\omega) = \frac{1}{\exp(\hbar\omega/k_B T) - 1} \tag{2.2}$$

where ω describes the frequency of the scattered light, T the temperature and k_B the Boltzmann factor. When comparing intensities at different temperatures a correction of the Bose-Einstein factor as $(n(\omega)+1)$, as it appears in Eq. 1.16, is necessary. The "+1" expresses the creation of one phonon. Therefore, second-order spectra need to be corrected by $(n(\omega)+1)(n(\omega)+2)$ for overtones or $(n(\omega_1)+1)(n(\omega_2)+1)$ for two phonons of different frequency.[77] In practice, it is however difficult to differentiate between the two cases unless a clear assignment of the second-order features is given.

Effect of the exciting wavelength

When measuring Raman spectra with different excitation wavelength, the wavelength dependence on the experimental setup needs to be taken into account. On the one hand, the intensities of different exciting lasers are not the same. On the other hand, the spectrometer response is strongly wavelength dependent. I.e. mirrors, lenses, filters, gratings as well as the CDD absorb, reflect and transmit light differently depending on the wavelength. There are two possibilities to overcome these problems.
First, the exciting light intensity can be measured and the spectra normalized accordingly. The instrument response can be calibrated using a tungsten white lamp (or similar) with a well-known optical spectrum. The calibration needs to be performed with care, since calibrations lamps tend to

be sensitive to external parameters and lifetime. In addition, the measured intensity needs to be corrected against the ω^4 dependence on the incident laser light (see Eq. 1.16).
A second possibility is the use of a reference sample. This reference material should have a high band gap and show no strong absorption or resonance phenomena in the energy range of interest, i.e. usually from 1.4 to 3.8 eV. If resonance and absorption phenomena are negligible, the variations of the scattered intensity for different laser wavelength are due to the different intensity of the incident light, the spectrometer response and the general ω^4 frequency dependence of the scattered intensity. By normalizing the spectra to the intensity of the reference sample, we correct against all these three effects at the same time[109]. For measurements in micro-Raman mode, it is important the keep the optical focus point on the sample constant, since the focus point is crucial for the scattered intensity.
A commonly used reference material is CaF_2 with a band gap of 11.2 showing only small resonance phenomena in the optical light spectrum[109,110]. CaF_2 possesses only one Raman-active vibrational mode of T_{2g} symmetry[82].
In CaF_2 strong fluorescence bands stemming from rare-earth impurities may complicate the fitting process of the only Raman band for some exciting wavelengths, giving rise to large error bars. Fig. 2.2 illustrates the spectra under excitation of 532 nm and 442 nm laser light. In the case of the 532 nm the Raman band is surrounded by fluorescence lines, whereas in the spectrum under the excitation of 442 nm, the Raman band is not disturbed by fluorescence.

Eq. 1.16 shows that the scattered intensity depends on the scattering volume. The scattering volume is wavelength dependent since, for example, the penetration depth of the light into the material is linked to the wavelength-dependent absorption coefficient. We define an as-measured efficiency $S^* = I_s/I_i$, where I_i and I_s are the measured incident and scattered intensities, respectively, and an efficiency S, which is corrected against wavelength-dependent scattering losses due to absorption and reflection at the surface. S and S^* are related as follows[110,111]:

$$S^* = S\frac{1-\exp\left[-\left(S+\alpha_i+\alpha_s\right)L\right)]}{S+\alpha_i+\alpha_s}\left(1-R_i\right)\left(1-R_s\right) \tag{2.3}$$

where L is the thickness of the crystal, α_i and α_s are the absorption coefficients and R_i and R_s the reflectivities for the incident and scattered radiation, respectively. If we neglect the reflectivity and assume that L is

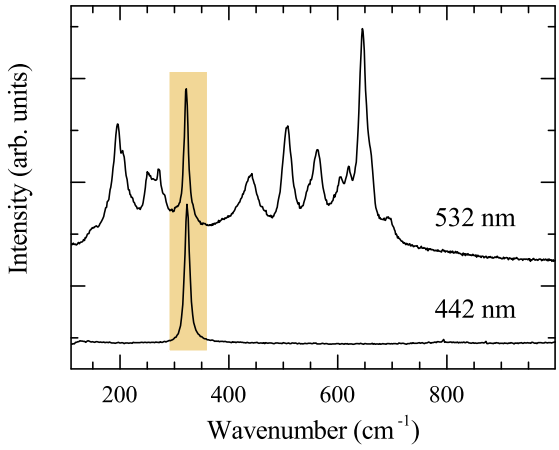

Figure 2.2: Raman spectra of CaF_2 measured under the excitation of 442 nm and 532 nm laser lines. The Raman-active T_{2g} vibration mode of CaF_2 is indicated by the orange rectangle. The remaining bands in the spectrum measured with the 532 nm laser are fluorescence lines.

sufficiently large and α_i and α_s larger than S, Eq. 2.3 becomes

$$\frac{I_s}{I_i} = S^* = \frac{S}{\alpha_i + \alpha_s}. \tag{2.4}$$

Therefore, it is common to correct the wavelength-dependent volume effects by multiplication of the scattering intensity with 2α, in backscattering configuration.[110,111]

These corrections do not allow to calculate the total scattered intensity, but only the ratio between different spectra.

2.2 Optical birefringence - Metripol setup

Birefringence is an optical property of materials with an anisotropic refraction index, i.e. the refraction index depends on the polarization and propagation direction of the light. Birefringence is highly sensitive to changes of the crystalline system and, therefore, an ideal mean to probe structural phase changes.
The velocity of an optical wave passing through a medium is given by: $v = c/n$, where c is the vacuum light-velocity and n is the refractive index. In an optically anisotropic medium, another wave with a polarization direction perpendicular to the first one will be slowed down differently due to a different refractive index n_2. Than the (linear) birefringence is given by[112]:

$$\Delta n = n_1 - n_2 \tag{2.5}$$

Therefore, changes of the birefringence under variation of external parameters reflect changes of the crystallographic plane perpendicular to the propagation direction to the optical wave. The refractive index for all propagation and polarization directions is represented by an ellipsoid, the optical indicatrix. For an isotropic material all axes of the ellipsoid have the same length and the ellipsoid becomes a sphere. In case of uni- or biaxial systems the axes lengths are given a = b $\neq$ c or a $\neq$ b $\neq$ c, respectively.
The phase shift δ of the optical wave depends, furthermore, on the thickness L of the sample and the wavelength λ of the light[112]:

$$\delta = \frac{2\pi}{\lambda}\Delta n L \tag{2.6}$$

Birefringence measurements presented in this work were performed in Prof. Dr. P.A. Thomas' group, Warwick University, UK, togehter with Dr. Steven Huband using a Metripol system (see Fig. 2.3). The system consists of a white light source followed by a filter to extract a certain wavelength and a rotating polarizer to assure linearly polarized light. The polarized light passes the sample and second polarizer, which acts as analyzer, before the intensity of the light is recorded by a CCD. The measured light intensity depends on the transmitted intensity I_0, the orientation of the indicatrix axis ϕ and the phase shift δ with respect to the polarizer and analyzer. These three parameters can be disentangled numerically by measuring the intensity for multiple configurations of polarizer and analyzer. So that the recorded intensity can be expressed as[113]:

$$I = \frac{1}{2} I_0 \left(1 + \sin(2(\theta - \phi)) \sin\delta\right), \tag{2.7}$$

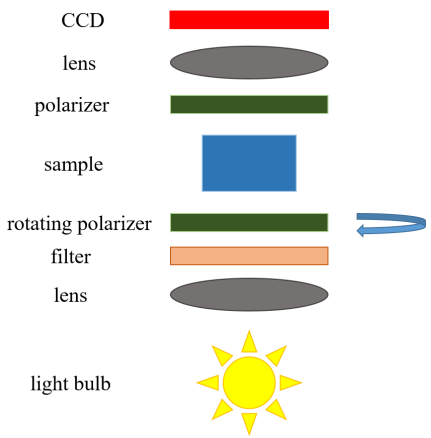

Figure 2.3: Sketch of the Metripol setup.

where θ is the angle of rotation of the polarizer. Rotation of the polarizer allows to calculate the transmittance I_0, the orientation angle ϕ of one of the axes of the indicatrix and the quantity $|\sin\delta|$, which is a function of the phase shift and thus a measure for the optical anisotropy.
Since the parameters are measured at the same time, they depend on each other, such that, if the orientation ϕ is not known in advance, only $|\sin\delta|$ can be determined and the absolute value of the sin-function will be reflected when calculating Δn. In turn, if $|\sin\delta|$ is not known, the value of ϕ can be off by 90°. Due to this fact, it occurs with changing $\sin\delta$ during a measurement series that the orientation ϕ experiences a shift by 90° which is without any physical meaning.
Finally, the result is decomposed into three images per measurement point for the three parameters. Regions of interest can be analyzed for changes under variation of external parameters.
Fig. 2.4 illustrates the images of $|\sin\delta|$ and ϕ of a zeolites dodecasil-3C crystal for temperatures below (Fig. 2.4(a) and (b)) and above (Fig. 2.4(c) and (d)) a tetragonal-to-cubic phase transition [114]. At room-temperature the crystal is optically anisotropic and shows a strong birefringence (Fig. 2.4(a)). The orientation is relatively uniform (Fig. 2.4(b)). Above the phase transition, the birefringence becomes zero (or close to zero) (Fig. 2.4(c)) indicating the optical isotropy of the cubic structure of the sample at high temperatures. A small remaining birefringence due to internal strain, gives rise to the radial coloring in Fig. 2.4(d) [114].

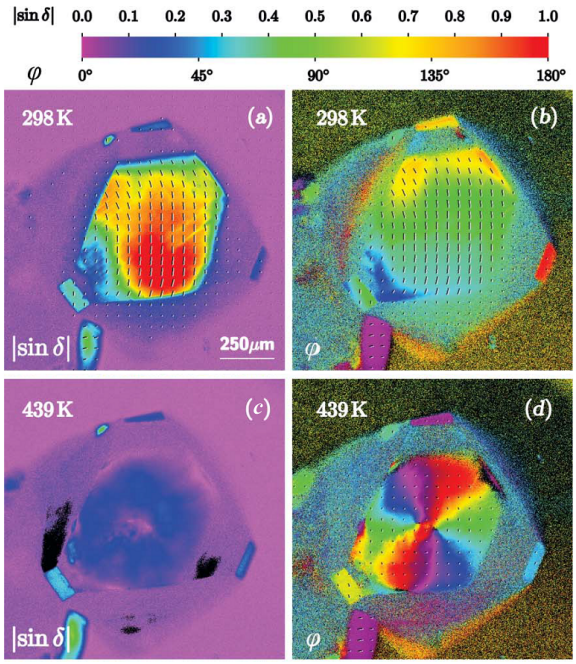

Figure 2.4: Images of $|\sin\delta|$ and ϕ of a zeolites dodecasil-3C crystal for different temperatures around a structural anomaly. Reproduced from Ref. 114.

A technical issue is the displacement of the sample during a measurement in particular if cooling pumps are connected to the sample holder. This problem was solved by comparing two subsequent intensity images, such that second image was artificially shifted step-wise on a rectangular grid of ca. 30×30 pixel. For every shift, the correlation value between first image and the shifted second image was calculated using Pearson's correlation function. The position of the second image was corrected according to the point of highest correlation. This procedure was repeated for every fifth image to take subtle displacements of less than one pixel per measurement point into account. A sample rotation during the measurement series can not be corrected and the series becomes unusable.

2.3 Temperature dependent measurements

Temperature dependent Raman spectroscopy and birefringence measurements were performed with a commercial Linkam stage THMS600 which allows a temperature range from 87 to 900 K (Fig. 2.5). Inside the cell the sample is placed on a ceramic block. The temperature is controlled via resistive heating of this ceramic block. Water cooling prevents the cell from overheating during high temperature measurements. For low-temperature measurements, the cell is cooled with liquid nitrogen.
The temperature cell can be positioned on the microscope stage. Incident and scattered light can pass through a glass window. In addition transmission measurement are enabled by a hole of about 2 mm in the middle of the ceramic.

Figure 2.5: Linkam Stage THMS600. Reproduced from Ref. 115.

2.4 Resonant ultrasound spectroscopy (RUS)

Resonant ultrasound spectroscopy (RUS) enables to probe elastic properties of a material. Elastic properties are highly sensitive to structural changes at an atomic level due to external parameters like temperature, pressure, electric or magnetic fields. Obvious candidates are solid-to-solid phase transition, but more subtle changes such as modifications of the magnetic structure can also affect the elastic constants.
The RUS measurements were performed in collaboration with Prof. Dr. M. Carpenter and Dr. D. McEvans, Earth Science Department, University of Cambridge, UK.
During a RUS measurement the sample is positioned between two piezoelectric transducers. One piezo-element vibrates at a frequency that is sweeped from 100 kHz to 2 MHz. The second piezo-element acts as detector. If the frequency of the signal coincides with the frequency of a natural vibration mode of the sample, there is a resonant enhancement of the sample vibration amplitude, which is then detected and recorded by the second piezo-element. The resonance frequency depends on the shape, density and elastic constants of the sample. The shape is not supposed to change during the measurement and the changes of the density can be considered small and continuously following the thermal expansion. Therefore, following the evolution of the resonance frequency with respect to a varying external parameter allows the direct tracing of an "effective" elastic constant. This effective elastic constant usually involves a linear combination of all the elastic constants of the material, unless very specific and controlled shapes are chosen. Besides, experience shows that RUS is mostly sensitive to shear moduli.[116]
When treating the data, measured peaks are fitted with a Lorentzian assuming a driven harmonic oscillator as

$$y(f) = y_0 + \frac{A}{(f - f_0)^2 + B}, \tag{2.8}$$

where y_0 defines a linear baseline, f_0 the resonance frequency and A and B are constants defining the shape of the Lorentzian. In practice, from an experimental point of view it is preferable to use an asymmetric Lorentz function, such that only the ratio of A/B differs for $f < f_0$ and $f > f_0$.[116]
There are two quantities extracted and analyzed. First, the square of the resonance frequency f_0^2 is proportional to the elastic constant to the corresponding acoustic mode. Second, we define a mechanical quality factor Q

by

$$Q = \frac{f_0}{\Delta f} \tag{2.9}$$

where Δf is full-width-at-half-maximum (FWHM) given as $\sqrt{B}$[116]. The inverse quality factor Q^{-1} is a measure of the mechanical dissipation of the acoustic wave in the sample. Anomalies in both factors, f_0^2 and Q^{-1}, are indications of a coupling between mechanical strain and a physical phenomenon in the material making RUS a powerful tool to investigate impacts on the crystal structure.[116]

Resonant ultrasound spectroscopy measurements are exemplified in Fig. 2.6 showing segments of RUS spectra of $KMnF_3$ for a temperature range from 11 to 290 K. Clear changes of the band evolutions appear at structural phase transitions at 83 ($Cmcm \rightarrow Pnma$; phase transition from high to low temperatures) and 185 K ($Pm\bar{3}m \rightarrow I4/mcm$)[117]. The phase transition $I4/mcm$ to $Cmcm$ at 87 K is less clear. The structural change at 185 K, ($Pm\bar{3}m \rightarrow I4/mcm$), is structurally the same phase transition as the earlier discussed transition in $SrTiO_3$ induced by octahedra rotation.

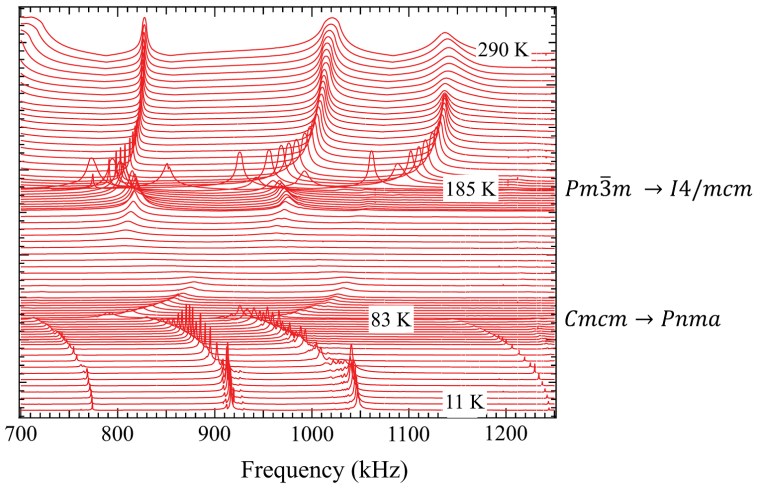

Figure 2.6: Segments of RUS spectra of $KMnF_3$ for a temperature range from 11 to 290 K. Changes of the band evolutions appear at structural phase transitions at 83 ($Cmcm \rightarrow Pnma$; phase transition from high to low temperatures) and 185 K ($Pm\bar{3}m \rightarrow I4/mcm$). Reproduced from Ref. 117.

Chapter 3

Raman scattering on rare-earth orthoferrites $R\mathrm{FeO}_3$ (R = La, Sm, Eu, Gd, Tb, Dy)

The work presented in the following has been submitted for publication to *Physical Review* ***B***, an APS journal. Major parts of the chapter are identical in word and content with the submitted draft. The density functional theory (DFT) calculations in this chapter were performed by Jorge Íñiguez and Hong Jian Zhao, Luxembourg Institute of Science and Technology, and are not part of the present work.

Introduction

In the past, rare-earth orthoferrites ($R\mathrm{FeO}_3$) perovskites have attracted considerable interest due to their remarkable magnetic properties[13,118,119]. At ambient conditions, all $R\mathrm{FeO}_3$ adopt an orthorhombic *Pnma* structure, hence their common name orthoferrites. Most members of the family possess a canted antiferromagnetic structure arising from spin moments of the Fe^{3+} cations. The antiferromagnetic ordering of the iron ions occur at a Néel temperature T_N around 650 to 700 K. Several orthoferrites show a spin reorientation towards lower temperatures. In contrast to the Fe^{3+} cations, the magnetic moments of the R^{3+} rare-earth ions order below 10 K[13]. Interestingly, a so-called compensation point where moments of the two sublattices

cancel has been reported for several $R\mathrm{FeO_3}$ [13]. More recently, orthoferrites have regained a considerable attention with a focus on spin-ordering processes of the rare-earth ions [120–122] and the interaction between magnetism and crystal lattice [8,14,16,19,123]. Within this context, the role of spin-lattice coupling in multiferroic properties has attracted a particular attention. Octahedra tilts are the main structural parameters to tune the band overlap and thus the physical properties related to the $\mathrm{FeO_6}$ octahedra. Unfortunately, octahedra tilt angles are chronically difficult to probe, specifically in thin films, because they require in-depth diffraction experiments needing at best large-scale instruments using neutron or synchrotron radiation. Alternatively, Raman spectroscopy is a well-known technique to follow tilt-driven soft-mode phase transitions [64,92,104]. More recently, it has been shown that Raman spectroscopy is also an appropriate probe for the investigation of lattice distortions and slight changes in octahedra rotations when exchanging the A cation [124]. As discussed in section 1.1.1, the size and physical properties of the A cation are crucial for the octahedral rotation systems and angles. Raman spectroscopy was used to trace the impact of different A cation sizes on the tilt angle for example for series of rare-earth manganites [125], chromites [126], or scandates [127].
All such investigations rely on thorough reference spectra, the knowledge of how the structural distortions can be derived from the phonon modes and more specifically on the proper band vibrational assignment. The present chapter aims at providing this fundamental knowledge by investigating a series orthoferrites and by proposing a consolidated view of this new data together with available literature data on other members of the family.

3.1 Rare-earth orthoferrites - structure

Rare-earth orthoferrites crystallize in an orthorhombic *Pnma* structure at ambient conditions. With respect to the parent cubic perovskite phase $Pm\bar{3}m$, the *Pnma* phase in orthoferrites can be derived by octahedral rotations. These octahedral rotations lead to an multiplication of the unit cell with respect to the cubic $Pm\bar{3}m$ space group and contains four formula units. In Fig. 3.1 the orthorhombic cell is given by the solid lines whereas the dashed lines illustrate the pseudo-cubic setting.
Octahedral tilts are the predominant type of distortion in rare-earth ferrites. In Glazer's notation the octahedra tilt system is expressed as $a^-b^+a^-$ [30] or in pseudo-cubic settings as rotations θ, ϕ and Φ around the $[101]_{\mathrm{pc}}$-, $[010]_{\mathrm{pc}}$-

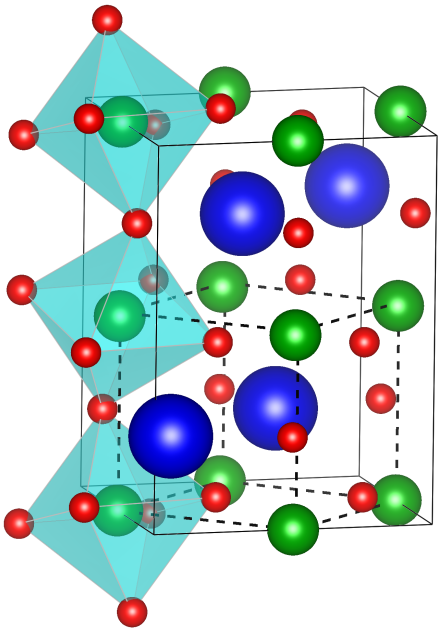

Figure 3.1: Rare-earth orthoferrite *Pnma* structure[128]. Oxygen atoms are given in red, iron in green and the rare earth elements in blue. Solid lines describe the orthorhombic unit cell. The dashed lines depict the pseudo-cubic setting. Three FeO_6 octahedra are depicted in pale gray.

and $[111]_{pc}$-axis, respectively[27]. Megaw has shown that θ and ϕ are sufficient to describe the octahedral rotations of the *Pnma* phase assuming that the octahedral tilts a_x^- and a_z^- are approximately equal[29]. Then, the rotation Φ can be expressed via $\cos\Phi = \cos\theta\cos\phi$[27]. Thus, the octahedral rotations represent the order parameters for a hypothetical second-order phase transition to the cubic $Pm\bar{3}m$ phase.

Like in other perovskites with a similar *Pnma* structure, such as orthomanganites $R\mathrm{MnO_3}$, orthochromites $R\mathrm{CrO_3}$, orthonickelates $R\mathrm{NiO_3}$, or orthoscandates $R\mathrm{ScO_3}$, we can assume in good approximation that changing the rare earth affects negligibly the chemical bonding of the material. However, the size of the rare earth impacts on the distortions of the structure, as measured for example by the tilt angles or the spontaneous strains, and can be continuously tuned by the size of the R^{3+} rare earth. The octahedral rotations are most reliably calculated from atomic positions (under the assumption that the octahedral tilts a_x^- and a_z^- are approximately equal, the

angle θ can be derived in two different ways)[129]:

$$\begin{aligned}\theta &= \tan^{-1}\left[4 \cdot \frac{\sqrt{w_{O(1)}^2 + u_{O(1)}^2}}{b}\right] \\ &= \tan^{-1}\left[4\sqrt{2} \cdot \frac{v_{O(2)}}{\sqrt{c^2 + a^2}}\right] \\ \phi &= \tan^{-1}\left[4 \cdot \frac{\sqrt{w_{O(2)}^2 + u_{O(2)}^2}}{\sqrt{c^2 + a^2}}\right]\end{aligned} \tag{3.1}$$

where a, b and c are the orthorhombic lattice parameters and u, v and w are the fractional ionic displacements from the special positions in the *Pnma* unit cell. The fractional coordinates are given in Table 3.1.

Table 3.1: Fractional coordinates for the *Pnma* space group.

	x	y	z
R	u_R	0.25	$1 - w_A$
Fe	0.5	0	0
O(1)	$0.5 - u_{O(1)}$	0.25	$w_{O(1)}$
O(2)	$0.25 - u_{O(2)}$	$v_{O(2)}$	$0.75 - w_{O(2)}$

Table 3.2 summarizes the structural specifications of all the members of the RFeO$_3$ family (lattice parameters and atomic positions are taken from Ref. 128,130). In order to illustrate the structural distortion throughout the series Fig. 3.2 presents the evolution of the tolerance factor t, the pseudo-cubic lattice parameters and the unit cell volume. From both, pseudo-cubic lattice parameters and tolerance factor, we find that with increasing ionic radius of the rare earth, from lutetium to lanthanum, the structure approaches a cubic metric, accompanied with a continuous increase in unit cell volume. Notably, LaFeO$_3$ appears to be closest to a cubic structure. Accordingly, the tolerance factor approaches unity for increasing rare-earth ionic-radius. Nevertheless, the *Pnma* structure is very stable and orthoferrites do not show a orthorhombic-to-cubic second-order phase transition for increasing temperatures.

In the literature orthoferrites are often discussed in *Pbnm* settings instead of *Pnma*. However, both notations describe the same crystal structure. In the space *Pbnm* setting the long orthonormal axis is defined as the c-axis

Table 3.2: Structural characteristics of RFeO$_3$: Lattice parameters in the orthorhombic *Pnma* setting (Ref. 128,130), R^{3+} ionic radii ($r_{R^{3+}}$ values given in an eightfold environment from Ref. 131), the tolerance factor t calculated from the ionic radii following Eq. 1.1 and octahedral tilt angles (ϕ[010], θ[101]) calculated from atomic coordinates (Ref. 128,130).

	Lattice parameters						FeO$_6$ octhahedra tilt angle	
	$r_{R^{3+}}$	a (Å)	b (Å)	c (Å)	V (Å^3)	t	$\phi_{[010]}$ (°)	$\theta_{[101]}$ (°)
LaFeO$_3$	1.160	5.563	7.867	5.553	243.022	0.934	7.127	12.216
PrFeO$_3$	1.126	5.578	7.786	5.482	238.085	0.921	9.575	13.617
NdFeO$_3$	1.109	5.584	7.768	5.453	236.532	0.915	10.024	14.467
SmFeO$_3$	1.079	5.584	7.768	5.400	234.233	0.904	11.172	15.575
EuFeO$_3$	1.066	5.606	7.685	5.372	231.437	0.899	11.623	15.977
GdFeO$_3$	1.053	5.611	7.669	5.349	230.172	0.894	11.948	16.165
TbFeO$_3$	1.040	5.602	7.623	5.326	227.442	0.889	12.135	16.920
DyFeO$_3$	1.027	5.598	7.623	5.302	226.255	0.884	12.605	17.284
HoFeO$_3$	1.015	5.598	7.602	5.278	224.611	0.880	12.702	17.694
ErFeO$_3$	1.004	5.582	7.584	5.263	222.803	0.876	12.927	18.217
TmFeO$_3$	0.994	5.576	7.584	5.251	222.056	0.872	12.936	18.587
YbFeO$_3$	0.985	5.557	7.570	5.233	220.134	0.869	13.382	18.958
LuFeO$_3$	0.977	5.547	7.565	5.213	218.753	0.866	13.240	19.455

whereas in *Pnma* settings the b-axis is long axis. The notations can be transformed into one or the other by permutation:

$$a_{Pnma} \leftrightarrow b_{Pbnm}$$
$$b_{Pnma} \leftrightarrow c_{Pbnm}$$
$$c_{Pnma} \leftrightarrow a_{Pbnm}$$

3.2 Sample description

The samples used in this study where synthesized in several external groups. SmFeO$_3$ single crystals were grown in an optical-floating-zone furnace by Cao and co-workers (for a detailed description see Ref. 121). Three single domain platelets were oriented along the three orthorhombic directions, with the edges parallel to crystallographic axes, and polished down to a thickness of ∼100 µm. The single domain state was verified by XRD and

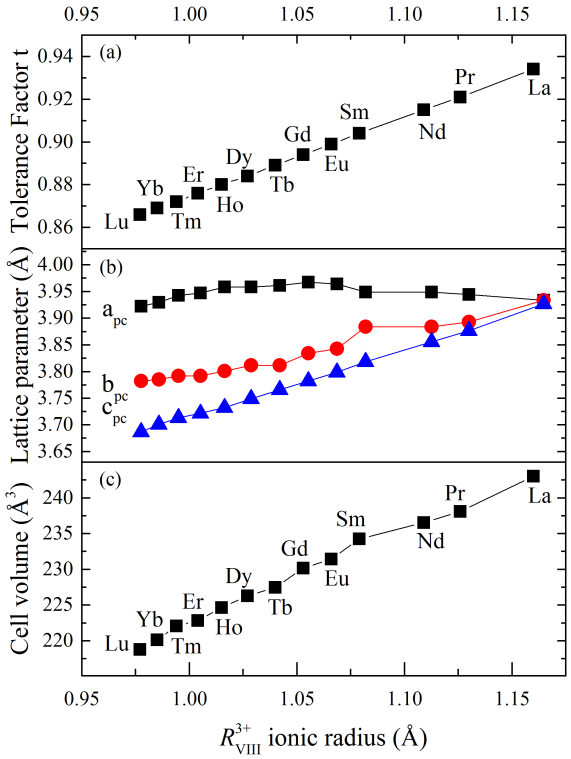

Figure 3.2: Variation of the pseudocubic cell parameters and orthoromic unit-cell volume as a function of the R^{3+}_{VIII} ionic radius[131]. The lattice parameters are taken from Ref. 128,130.

polarized light microscopy. A $SmFeO_3$ crystal was manually grinded to acquire a homogeneous powder. $LaFeO_3$ and $EuFeO_3$ powders were obtained by conventional solid-state reactions by R. Haumont (Universit Paris Sud). $GdFeO_3$ and $DyFeO_3$ powder samples were prepared by E. Queiros and P.B. Tavares (University of Trás-os-Montes e Alto Douro) using the urea sol-gel combustion method, reported elsewhere[132]. Their quality was checked by XRD and SEM. $TbFeO_3$ samples were prepared by M. Mihalik jr., M. Mihalik, and M. Zentkova (Slovak Academy of Sciences) via floating-zone method in a FZ-T-4000 (Crystal Systems Corporation) mirror furnace. As starting materials, Fe_2O_3 (purity 2N, supplier: Sigma Aldrich), and Tb_4O_7 (purity 3N; supplier: Alpha Aesar) were used. They were mixed in a Tb:Fe stoichiometric ratio, cold pressed into rods and sintered at 1100°C for 12 to 14 hours in air. Their quality was checked by X-ray powder diffraction and by energy dispersion X-ray analysis, confirming the single perovskite phase.

3.3 Raman scattering on rare-earth orthoferrites

3.3.1 Raman spectra and mode assignment

The orthorhombic *Pnma* structure gives rise to 24 Raman-active vibrational modes[85], which decompose into $\Gamma_{\text{Raman}} = 7A_g + 5B_{1g} + 7B_{2g} + 5B_{3g}$:

$$\begin{pmatrix} a & & \\ & b & \\ & & c \end{pmatrix} \quad \begin{pmatrix} & d & \\ d & & \\ & & \end{pmatrix} \quad \begin{pmatrix} & & e \\ & & \\ e & & \end{pmatrix} \quad \begin{pmatrix} & & \\ & & f \\ & f & \end{pmatrix}$$

$$A_g \qquad B_{1g} \qquad B_{2g} \qquad B_{3g}$$

Schematically, the vibration modes below 200 cm^{-1} are mainly characterized by displacements of the heavy rare-earth ions. Above 300 cm^{-1}, motions of the light oxygen ions dominate; in the intermediate frequency range, vibration patterns involve both ions. Note that iron ions are occupying centers of inversion in the *Pnma* structure and, therefore, vibrations with Fe^{3+} motions are not Raman active, as discussed in section 1.2.1. Fig. 3.3 shows the Raman spectra of six rare-earth orthoferrites $R\text{FeO}_3$ (R = La, Sm, Eu, Gd, Tb, Dy) recorded under excitation of the 633 nm laser line. All spectra were measured at 80 K in order to reduce thermal broadening and ease the mode identification. Thanks to well-defined spectra, we identify between 18 and 21 vibration bands, depending on the compound. The remaining predicted modes are either masked by band overlap or their intensity is below the detection limit. The Raman spectra of SmFeO_3, EuFeO_3, GdFeO_3, TbFeO_3 and DyFeO_3 present a similar overall spectral signature which allows to follow the evolution of particular bands throughout the series. The spectral signature of LaFeO_3 is distinctly different as explained by the size difference between La^{3+} and the closest Sm^{3+} and also its proximity to the cubic structure (see Fig. 3.2). This is similar to observations for other rare-earth perovskites, where the Raman spectrum of the lanthanum member is systematically different when compared to the remaining series[125,126,133]. This will be elaborated in the later discussion.

In order to go further in the mode assignment, we performed a polarized Raman study of the SmFeO_3 single crystals. In the following, we use X, Y, Z to indicate the crystallographic axes in *Pnma* settings. From the Raman tensors (see above), we find that for the orthorhombic *Pnma* structure A_g can exclusively be observed, if the polarization of the analyzed light is in

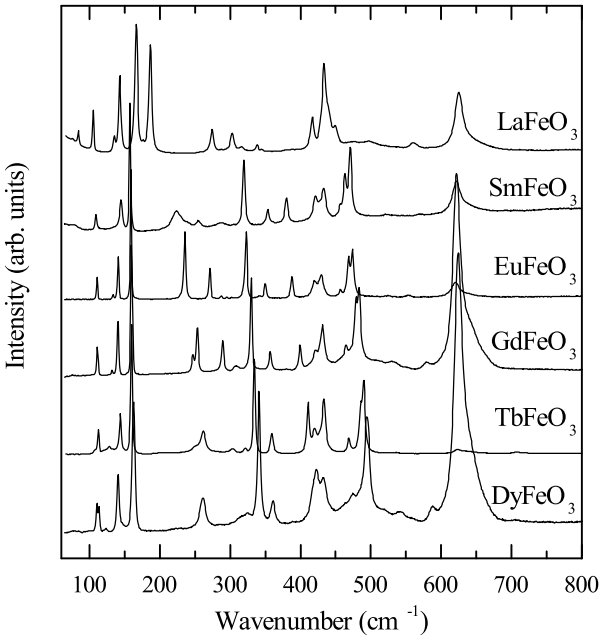

Figure 3.3: Raman spectra at 80 K of six rare-earth orthoferrites $R\mathrm{FeO_3}$ (R = La, Sm, Eu, Gd, Tb, Dy) collected with a 633 nm He-Ne laser line.

parallel with the exciting laser polarization and a crystalline axis, i.e. (XX), (YY) and (ZZ), in Porto's notation[134] (see section 2.1.2). The vibration modes of B-type symmetries are solely visible for configurations where the polarizations of exciting and analyzed light are perpendicular to each other and parallel to specific crystal axes (for B_{1g}: $\mathrm{Z(XY)\overline{Z}}$, B_{2g}: $\mathrm{Y(XZ)\overline{Y}}$, B_{3g}: $\mathrm{X(YZ)\overline{X}}$)[85].

Figure 3.4 presents the obtained results for $\mathrm{SmFeO_3}$ single crystals for twelve scattering configuration. Fig. 3.4(a) shows the Raman spectra for A_g configurations modes, while spectra exhibiting B_{1g}, B_{2g} or B_{3g} modes are given in Fig. 3.4(b). In total, we identify all expected A_g, six B_{2g} modes and four out of five B_{1g} and B_{3g} modes (see Table 3.3). The band between 600 and 650 $\mathrm{cm^{-1}}$ in Fig. 3.4(a) is not attributed to a first-order Raman mode, as will be discussed separately.

In the next step, DFT calculations of phonon modes for all compounds performed by Jorge Íñiguez and Hong Jian Zhao, Luxembourg Institute of Science and Technology, are used to confirm the mode symmetries and associate vibrational patterns for each mode. A summary of all theoretical and experimental band frequencies with their symmetry and main atomic

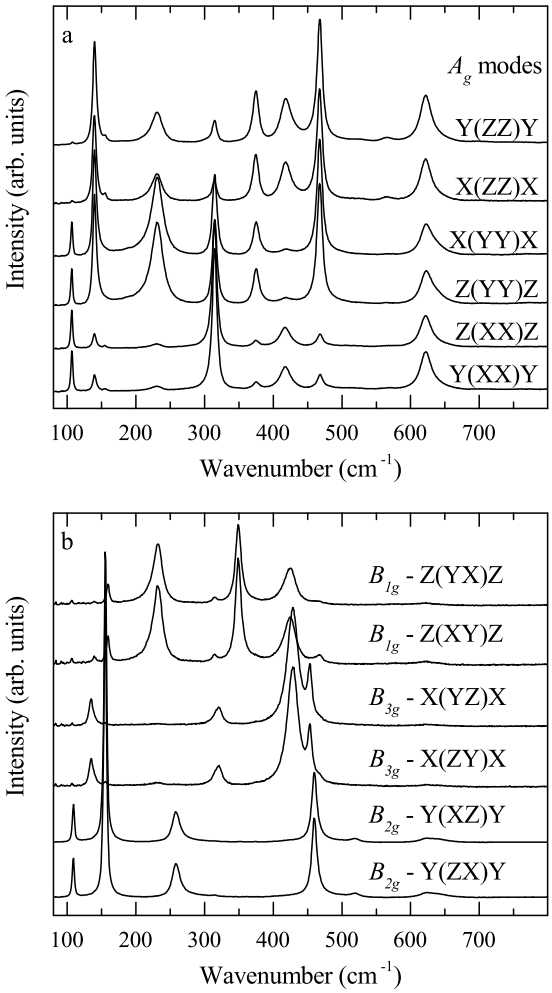

Figure 3.4: Polarized Raman spectra of $SmFeO_3$ at ambient conditions. The measurement configurations are given in Porto's notation, in a) for the vibration modes of A_g symmetry and in b) for the vibration modes of B_{1g}, B_{2g} and B_{3g} symmetries. X, Y and Z correspond to the orthorhombic axes in the *Pnma* space group.

motions are given in Table 3.3. The calculated frequencies are in very good agreement with our experimental values and confirm the continuous evolution of the spectral signature. For $LaFeO_3$ the changes to the spectral signature are too drastic with respect to the other members of the series. Therefore, DFT calculations are essential to correctly assign the Raman phonon modes of $LaFeO_3$ to the corresponding symmetries and vibrational patterns.

Table 3.3: Experimental and theoretical band positions, the corresponding symmetry assignment and main atomic motions of the observed and calculated Raman modes in $R\mathrm{FeO_3}$. The main atomic motions are extracted from DFT calculations.

Symmetry	$LaFeO_3$		$SmFeO_3$		$EuFeO_3$		$GdFeO_3$		$TbFeO_3$		$DyFeO_3$		main atomic motion
	80 K	calc.	80 K	calc.	80 K	calc.	80 K	calc.	80 K	calc.	80 K	calc.	
$A_g(1)$	84.5	88.5	109.5	109.1	110.9	112.1	111.1	111.4	107.7	111.9	110.6	111.7	R(x), in-phase in x-z, out-of-phase in y
$A_g(2)$	135.3	127.3	144.2	138.1	140.7	140.1	140.4	136.6	143.9	136.2	140.5	135.27	R(z), out-of-phase
$A_g(3)$	186.6	182.5	223.9	243.9	235.1	252.4	253.2	254.9	261.9	259.3	261.5	262.31	$[010]_{\mathrm{pc}}$ FeO_6 rotation, in-phase
$A_g(4)$	274.2	272.7	319.1	320.4	323.2	324.92	329.9	330.3	334.5	330.3	341.1	332.31	O(1) x-z plane
$A_g(5)$	302.8	306.1	379.5	382.8	387.8	397.1	399.4	405.1	410.9	410.4	422.4	422.18	$[101]_{\mathrm{pc}}$ FeO_6 rotation, in-phase
$A_g(6)$	449.8	433.3	420.7	413.1	419.6	414.2	420.9	416.4	420.1	416.3	417.3	414.8	Fe-O(2) stretching, in-phase
$A_g(7)$	433.3	412.6	470.7	467.9	474.0	475.5	483.6	480.2	490.1	484.3	496.8	490.2	O(1)-Fe-O(2) scissor-like bending
$B_{1g}(1)$		169.3	160.7	151.3		149.1		142.6		138.9		134.7	R(y) in-phase in x-z, out-of-phase in y
$B_{1g}(2)$		147.5	238.7	232.5	236.4	243.01	247.1	244.0	251.9	248.3		250.3	$[010]_{\mathrm{pc}}$ FeO_6 rotation, out-of-phase
$B_{1g}(3)$	338.1	327.7	353.3	351.7	350.0	355.7	357.0	356.4	359.2	356.4	360.9	358.8	$[010]_{\mathrm{pc}}$ FeO_6 rotating, out-of-phase
$B_{1g}(4)$	442.3	424.5	426.4	421.8	425.8	423.7	428.8	425.9	427.7	424.7	427.4	427.2	Fe-O(2) stretching, out-of-phase
$B_{1g}(5)$	560.9	583.7		593.7		597.1		595.3		592.0		593.2	Fe-O(1) stretching
$B_{2g}(1)$	105.5	103.2	109.8	109.3	110.9	111.1	111.1	109.1	112.5	109.1	113.3	108.5	R(z), in-phase in x-z, out-of-phase in y
$B_{2g}(2)$	143.0	143.5	157.4	158.9	159.3	162.5	159.9	160.5	160.1	161.1	162.8	160.8	R(x), out-of-phase
$B_{2g}(3)$	166.5	171.7	255.0	277.7	271.1	290.6	289.3	298.9	302.7	304.8	324.9	310.8	$[101]_{\mathrm{pc}}$ FeO_6 rotation, in-phase
$B_{2g}(4)$		329.1		346.0		347.8		348.7		349.2		350.6	O(1) x-z plane
$B_{2g}(5)$	416.8	401.2	462.8	460.2	468.2	469.1	478.9	474.0	485.6	477.7	493.7	482.4	O(1)-Fe-O(2) scissor-like bending
$B_{2g}(6)$		481.4	521.5	512.6	524.5	521.0	531.7	527.5	535.8	528.4		534.3	O(2)-Fe-O(2) scissor-like bending, in-phase
$B_{2g}(7)$	625.1	621.6	640.5	609.5	638.1	612.7	640.5	611.6		610.5	624.2	612.2	Fe-O(2) stretching, in-phase
$B_{3g}(1)$		136.7	145.0	134.5	133.6	134.1	132.2	128.6		125.8		122.9	R(y), out-of-phase in x-z, y
$B_{3g}(2)$	316.8	299.5	322.8	312.5		314.8		311.9		311.1		311.1	O(1)-Fe-O(2) in-phase
$B_{3g}(3)$	436.0	424.5	432.7	423.7	429.9	424.0	431.5	425.8	433.3	422.0	433.1	423.5	octahedra squeezing in y
$B_{3g}(4)$	428.6	407.6	455.9	446.5	456.7	452.2	465.0	454.5	468.8	456.7	473.7	459.8	O(2)-Fe-O(2) scissor-like bending, out-of-phase
$B_{3g}(5)$	641.9	650.2		640.5		642.8		640.0		636.9	639.4	637.2	FeO_6 breathing

Last, the band between 600 and 650 cm^{-1} shows a peculiar behavior and needs a specific discussion. First, as can be seen in Fig. 3.3, its frequency seems to be independent of the rare earth. Besides, it shows intensity variations from sample to sample that contrast with the other bands, and also exhibits a strong asymmetry. For $SmFeO_3$, Fig. 3.4 shows that bands appear in the region with very low intensity in crossed polarization, but the intensity is much stronger for the feature in parallel configuration, which would rather point to a A_g symmetry. However, as can be seen in Table 3.3, the calculations predict two bands of B_{2g} and B_{3g} symmetry in this region, but no A_g Raman mode, and all A_g modes are already conclusively attributed. Therefore, we conclude that this band is not a first-order Raman mode of intrinsic origin.

Similar features have been reported in other perovskite oxides, very often with unclear assignments and conflicting reports. As an example, Iliev *et al.* discussed it for $LaCrO_3$ [135] and demonstrated that its intensity can be reduced by annealing the sample in vacuum. Therefore, it seems likely that it is related to chemical defects of the lattice [135]. Here, we note that $DyFeO_3$ and $GdFeO_3$, where this band is stronger, were produced by a chemical metal-organic process, whereas the other samples ($LaFeO_3$, $SmFeO_3$, $EuFeO_3$ and $TbFeO_3$) were synthesized by solid-state reaction. A difference in defect chemistry originating from different growth processes is therefore plausible. A defect-activated, Raman-forbidden, infrared (IR)-active mode can be excluded, since DFT calculations do not reveal any IR-active bands in this spectral range. A possible hypotheses is the activation of the band by Jahn-Teller distortion induced through defects. Perovskites of *Pnma* space group showing Jahn-Teller distortion have been found to display bands of strong intensity in the spectral region of 600 and 700 cm^{-1}. It was found that all rare-earth orthomanganites show an extremely strong band in this wavenumber area when comparing to the rest of the spectrum [136] (Mn^{3+} is a Jahn-Teller-active cation). An extensive study on the solid solution $LaFe_{1-x}Cr_xO_3$ reveals a very interesting behavior of the band between 600 and 700 cm^{-1} [137–139]. The band is of low intensity for the end members of the solid solution, $LaCrO_3$ and $LaFeO_3$. However, smallest amounts of iron or chromium lead already to a dramatic intensity increase of the band. A $Fe^{3+}Cr^{3+}$ to $Fe^{4+}Cr^{2+}$ charge transfer proposed by Andreasson and coworkers would allow a Jahn-Teller distortion [137]. This fits with the scenario that the band between 600 and 700 cm^{-1} is Jahn-Teller activated.

3.3.2 Phonon modes vs. ionic radii and octahedra tilt angle

In this section we analyze the evolution of the band positions with changing rare-earth ions. A special focus is put on relation between the octahedra tilting vibrations and order parameter. Here, we wish to go beyond the common picture of the linear relation between octahedra tilt angle and vibration frequency by considering the changes of octahedra rotations in the context of Landau theory. Fig. 3.5 presents the evolution of the band po-

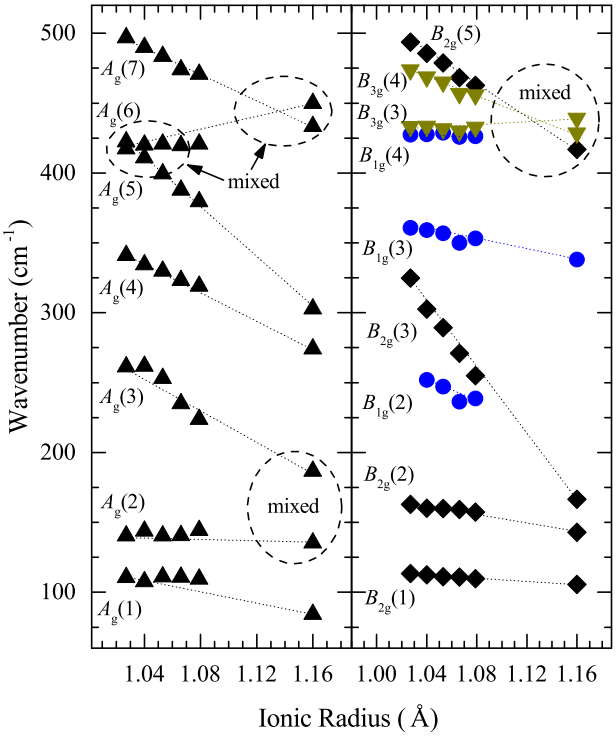

Figure 3.5: Raman phonon wavenumbers of $R\mathrm{FeO_3}$ as a function of the rare earth R^{3+} ionic radius. All lines are guides to the eye only. The encircled areas indicate mode mixing regions.

sitions for the different orthoferrites as a function of the ionic radii of the rare-earths. Symmetries and band evolution are based on the symmetry and mode assignment discussed above (Table 3.3). Overall, Raman bands shift to lower frequencies with increasing $\mathrm{r}_{R^{3+}}$, which naturally correlates with the increase of the volume, and therefore of most bond lengths. It can be seen that the $\mathrm{r}_{R^{3+}}$-dependent shift in wavenumber varies significantly among the different Raman modes. This is understood in the context of structural

instabilities in the *Pnma* structure.
In the framework of Landau theory for second-order phase transitions, the two octahedra rotations represent the two order parameters for a second-order phase transition to the high-symmetry parent cubic perovskite phase. This is equivalent with the change of the octahedra tilt system $a^-b^+a^-$ (*Pnma*) to the cubic $a^0a^0a^0$ (see Fig. 1.3). Accordingly, the soft-modes of the system adapt vibrational patterns of octahedral rotations, as discussed in section 1.2.5 which can experience very large shifts.
Thus our Raman data across the RFeO$_3$ family exhibits patterns that provide useful insights into the relations among structural order parameters and associated phonon frequencies driven by the R^{3+} cation. Before analyzing the experimental data, we intend to find a connection between the size of the rare-earth cation and the soft-mode frequency. This we base on Landau theory which is in accordance with the soft-mode-to-order-parameter relation for temperature driven phase transitions introduced in section 1.2.5.
The structural order parameter η may correspond to FeO$_6$ rotations either around the $[010]_{\mathrm{pc}}$ or the $[101]_{\mathrm{pc}}$ axis. Let ϵ be the isotropic strain of the material. We assume that $\eta = \epsilon = 0$ corresponds to the ideal cubic perovskite. Asuming the simplest Landau potential, the general Landau free energy in Eq. 1.41 becomes

$$F(\eta, \epsilon) = \frac{1}{2}A'(T - T_{\mathrm{c}})\eta^2 + \frac{1}{4}B\eta^4 + \frac{1}{2}\gamma\epsilon\eta^2 \,, \tag{3.2}$$

where the $A'(T-T_{\mathrm{c}})$ and B parameters are defined according to section 1.2.5. Furthermore, the Landau potential also includes the lowest-order coupling between ϵ and η that is allowed by symmetry. We focus on the behavior of the material at temperatures well below the structural transition between the cubic and orthorhombic phases.
We assume that all the RFeO$_3$ orthoferrites present the same parameters quantifying the energetics of η and ϵ, and that the only feature changing from compound to compound is the value of the strain ϵ, as given by the size of the rare-earth cation. More specifically, we define the strain as

$$\epsilon = \kappa(\overline{r} - r), \tag{3.3}$$

where r is the radius of the rare-earth cation for a particular RFeO$_3$ compound; $\overline{r}$ be a reference value for the ionic radii of the R^{3+} cations such that $\epsilon = 0$ in a hypothetical cubic phase, and κ be a proportionality constant. Substituting Eq. 3.3 in Eq. 3.2, we obtain an r-dependent free energy

applicable to the whole family of orthoferrites:

$$F(\eta, r) = \frac{1}{2}[A'(T - T_c) + \kappa\gamma(\bar{r} - r)]\eta^2 + \frac{1}{4}B\eta^4 \ . \tag{3.4}$$

The compound dependence is restricted to the harmonic part of the potential. Further, formally, the ionic radius r plays the exact same role as the temperature.
Let us introduce $\bar{A} = A'(T - T_c) + \kappa\gamma(\bar{r} - r)$. Then, we derive following section 1.2.5

$$\eta_{eq} = \pm(-\bar{A}/B)^{1/2} \tag{3.5}$$

for the equilibrium order parameter at $T \ll T_c$. (At such a temperature, we assume $\bar{A} < 0$ for all relevant r values, see section 1.2.5.) With Eq. 1.50 the associated soft-mode frequency becomes

$$\omega = \sqrt{\frac{2B}{m}}\,\eta_{eq} \ , \tag{3.6}$$

where m is a mass characteristic of the order parameter η. Now, combining these equations we can write

$$\omega = \sqrt{\frac{2B}{m}}\,\eta_{eq} = \left[-\frac{A'(T - T_c) + \kappa\gamma(r - \bar{r})}{m/2}\right]^{1/2} \ , \tag{3.7}$$

which gives us the relation between the compound-dependent parameter (the ionic radius r), temperature T, the relevant structural distortion η, and its corresponding phonon frequency ω. In other words, we expect a linear relation between order parameter η, i.e. octahedra tilt angle, and the corresponding soft-mode frequency ω, which is solely dependent on the ionic radius r of the rare earth and the temperature T. In particular, if we fix the temperature, this expression allows us to compare (and predict the behavior of) the structural and Raman data across the orthoferrite series.

In order to apply this relation to the orthoferrite family, the identification of the soft modes is crucial. As discussed earlier (see section 1.2.5), an order parameter may give rise to several soft modes which do not necessarily need to be Raman active. However, Birman[105] and Shigenari[106] showed that one of the soft modes related to one order parameter has a Raman-active A symmetry in the low symmetry phase. In the *Pnma* structure it is therefore common to focus on the A_g soft-modes. From DFT calculations (see Table 3.3), we find that the $A_g(3)$ and $A_g(5)$ modes are the soft-modes to corresponding $\eta_{[010]_{pc}}$ and $\eta_{[101]_{pc}}$, respectively, where $\eta_{[010]_{pc}}$ and $\eta_{[101]_{pc}}$

are the order parameters of the *Pnma* structure representing the octahedra rotations around the $[010]_{\mathrm{pc}}$ and the $[101]_{\mathrm{pc}}$ axes. The assignment of the $A_g(3)$ as a soft-mode is at variance with earlier work by Todorov and co-workers[124] and underlines the importance of precise calculations to gain full understanding of the experimental findings.
Fig. 3.6 presents the evolution of the soft-modes $A_g(3)$ and $A_g(5)$ against the corresponding octahedra-rotation angle. For completeness and in order to test the general validity of this model, we extend our graph by literature data on orthoferrites with Lu, Tm, Er, Ho and Nd[140–143]. The evolution shows the expected linear relation between the vibrational frequencies and the tilt angles of the $R\mathrm{FeO_3}$. This adds further support to the proposed soft-mode-like relation of tilt frequency and size of the rare earth, not only in the orthoferrites, but also for other families where this behavior has been experimentally verified: orthomanganites[125], orthochromates[126], orthoscandates[127] among others[124]. However, at variance with these previous experimental data, our work on orthoferrites show two additional features that have to be commented on, namely that i) the two tilt modes follow two different lines and ii) $\mathrm{LaFeO_3}$ deviates significantly from the general linear behavior.

The octahedral-rotation angles and soft-mode frequencies do not present the same scaling for the different order parameters. The rotation $\eta_{[010]_{\mathrm{pc}}}$ around $[010]_{\mathrm{pc}}$ reveals a scaling factor of 21.1 cm^{-1}/deg whereas the slope of the rotation $\eta_{[101]_{\mathrm{pc}}}$ around $[101]_{\mathrm{pc}}$ gives 23.9 cm^{-1}/deg. This is natural and expected when bearing in mind that the two soft-modes are associated with two independent order parameters. The relation in Eq. 3.7 needs to be separately considered for each of the relevant order parameters (in-phase and anti-phase $\mathrm{FeO_6}$ rotations in our case), and there is no reason to expect that the values of the coefficients in our Landau potential will be the same for different order parameters. However, this difference was never pointed out in previous investigations[124–127]. This probably comes from a combination of factors including experimental difficulties in mode assignment and frequency determination, scattered data from a more limited number of compounds; and possibly the differences in scaling factors are too small to be resolved experimentally. Even though the two scaling factors might be coincidentally equal within experimental uncertainties for a given family of compounds, it is very likely that a careful (re)investigation of the other series would reveal this difference.

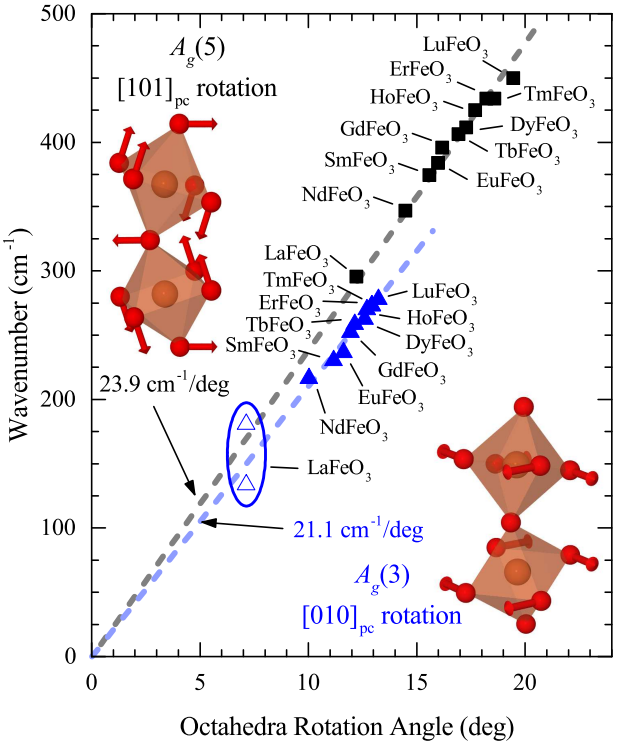

Figure 3.6: RFeO$_3$ soft-mode wavenumbers at ambient conditions as a function of octahedra-tilt angles for $A_g(3)$ [blue triangles] and $A_g(5)$ [black circles] modes. Raman band positions for NdFeO$_3$ [143], HoFeO$_3$, TmFeO$_3$ [141], ErFeO$_3$ [142] and LuFeO$_3$ [140] are taken from the literature. The blue oval points out the mode-mixing zone of the $A_g(2)$ and $A_g(3)$ modes of LaFeO$_3$. The open triangles indicate this exceptional mode-mixing case.

Mode mixing in LaFeO$_3$

Last, we investigate the case of LaFeO$_3$ in more details. For LaFeO$_3$, no A_g Raman mode actually follows the scaling of the $\eta_{[010]_{pc}}$-rotation given by the other members of the series. Instead, the $A_g(2)$ and $A_g(3)$ modes, plotted as open triangles in Fig. 3.6, fall below and above the scaling line respectively. On the other hand, we have already pointed out that the band positions in LaFeO$_3$ differ significantly from the other orthoferrites and do not seem to follow the continuous evolution of the other spectra. In order to rationalize this comparatively exotic behavior, we analyzed in detail the vibrational patterns given from first-principle calculations for LaFeO$_3$ and SmFeO$_3$. This analysis reveals several mode crossing and mode mixing situations.

Mode crossing is only allowed for vibrational modes of different symmetries. Mode mixing can occur when modes of the same symmetry approach, while vibrations of the same symmetry are not allowed to cross but will mix and exchange their vibrational character. In $LaFeO_3$, the mode mixing occurs in the regions between 100 and 200 cm^{-1} and 400 and 450 cm^{-1} where several vibrational modes are found. These mode mixings are indicated in Fig. 3.5 by dashed circles. In particular, it strongly affects the lower soft-mode $A_g(3)$ as it approaches the lower lying $A_g(2)$. For Sm^{3+} and smaller cations, these two modes have very distinguishable atomic displacement patterns: the $A_g(2)$ mode is dominated by R^{3+} displacements, while $A_g(3)$ is dominated, as already pointed out, by octahedral rotations. In contrast, in $LaFeO_3$, the two modes have significant contributions from both La^{3+} displacement and octahedral rotations. It is therefore no longer possible to identify any of them as the soft-mode of interest associated with octahedral tilts only. The soft-mode frequency for a hypothetical unmixed-state would lie between the two positions. This in turn enables us to understand why the Raman spectrum of $LaFeO_3$ is significantly different as a whole from the others members of the series, since the mode coupling will affect band positions and intensities. This behavior *par excellence* has been reported by Iliev *et al.* in orthomanganites[144], but was also found in $(La_xSm_{1-x})CrO_3$ solid solutions[133] and is probably a general phenomenon occurring in orthorhombic *Pnma* perovskites in the limit of small tilt angles, where distortions of the octahedra have to be taken into account[145].

3.4 Conclusion

We have presented a Raman scattering study of a series of six members of the rare-earth-ferrite family $R\mathrm{FeO_3}$ (R = La, Sm, Eu, Gd, Tb, Dy). A symmetry assignment of the observed modes has been presented on the basis of a single-crystal study of $\mathrm{SmFeO_3}$, DFT calculations and by taking advantage of the continuous changes in the Raman spectra across the whole $R\mathrm{FeO_3}$ series. This careful assignment has allowed to relate most of the vibration modes to their vibrational pattern and symmetries. Based on this, we can follow the structural evolution across the series and we have namely shown that the $A_g(3)$ and $A_g(5)$ modes are the soft-modes of A_g symmetry which correspond to the octahedral-rotation order-parameters $\eta_{[010]_{\mathrm{pc}}}$ and $\eta_{[101]_{\mathrm{pc}}}$. In this framework we demonstrated the proportionality of soft-mode frequency and order parameter. Furthermore, we showed that for rare-earth orthoferrites (and similar series) the change of the soft-mode frequency depends only on the size of the rare earth (for a fixed temperature). This work provides reference data for structural investigation of the orthoferrite family $R\mathrm{FeO_3}$, and will be helpful for further studies of phenomena in orthoferrites including structural instabilities, possible ferroelectricity and multiferroicity, and rare-earth magnetism at low temperature via spin-phonon coupling.

Chapter 4

Temperature dependent structural investigations of samarium ferrite $SmFeO_3$

Introduction

Much research is devoted to identify multiferroic materials that possess strongly coupled ferroic properties - preferably close to ambient conditions, a "room temperature multiferroic". On the one hand, a major focus is set on the "type I" multiferroic $BiFeO_3$ which possesses magneto-electric coupling at room-temperature and strong polarization ($100\ \mu Ccm^{-2}$)[20]. On the other hand, "type II" multiferroics attract interest for the magnetically-induced ferroelectricity providing direct coupling of both properties. The most investigated "type II" multiferroic is $TbMnO_3$[54,146,147] where the cycloidal ordering of the Mn^{3+} spins below 27 K breaks the symmetry and induces a ferroelectric displacement[148]. However, the induced ferroelectricity is small ($0.08\ \mu Ccm^{-2}$)[146] in comparison with $BiFeO_3$.
In the context of "type II" multiferroics, another group of materials has recently attracted attention: rare-earth orthoferrites, $RFeO_3$. For several rare-earth orthoferrites "type II" multiferroelectricity was reported[8,14,15]. At variance with $TbMnO_3$, the "type II" multiferroelectricity in $RFeO_3$ does not require a cycloidal spin structure, but arises from the magnetic ordering of both, iron *and* rare-earth cations.
In general, the rich magnetic landscape of rare-earth orthoferrites, including high Néel temperatures (600 K and 700 K), spin reorientations, ordering

of the rare-earth sub-lattice and compensation of the two spin lattices[13], makes these materials potential candidates for magneto-electric coupling.
Building up on the general understanding of vibrational and structural properties of rare-earth orthoferrites in the previous chapter, we investigate in more detail one member of the family, $SmFeO_3$, which has especially high magnetic transitions temperatures in comparison with other RFeO$_3$. We are particularly interested in the coupling of different magnetic orders with the crystal lattice. Multiferroic properties in bulk $SmFeO_3$ have been controversially discussed[16–19]. Most studies focus only on the high temperature region above room temperature. However, recent studies suggest an ordering of the Sm^{3+} spin sublattice at surprisingly high ~ 140 K[122,149] which was initially expected below 10 K[13]. In this study, we investigate a large temperature range from 80 to 830 K with a focus on spin-lattice interactions.
In order to detect and follow coupling phenomena, we use three complementary techniques as a function of temperature: Raman spectroscopy, resonant ultrasound spectroscopy and optical birefringence.

4.1 Review of magnetic properties of $SmFeO_3$

At first we review the magnetic transitions of $SmFeO_3$ which are summarized Fig. 4.1(a). The iron Fe^{3+} spins order at the Néel temperature $T_N = 680$ K in a G-type antiferromagnetic structure with the spins along the c-axis[121]. A slight spin canting leads to a net magnetic moment in b-direction as illustrated in Fig. 4.1(b).
The high-temperature magnetic structure is stable down to 480 K (T_{SR-1}), where a spin reorientation occurs. The antiferromagnetic moments rotate continuously in the b-c plane by 90° from the c to the b direction, such that the net magnetic moment is aligned along the c-axis[13]. The reorientation process is completed at $T_{SR-2} = 450$ K* (Fig. 4.1(c)). The reorientation of the iron-spin lattice has been explained by a temperature dependent anisotropy of the samarium moments which triggers the reorientation process through a Fe^{3+}-Sm^{3+} spin interaction[13]. The samarium-iron interaction is much weaker than the iron-iron interaction but polarizes the Sm^{3+} spins "quasi-paramagnetically" in the exchange field of the net magnetic moment of the iron magnetism[13]. In general, in RFeO$_3$ the alignment of the rare-

*The values of the spin-reorientation temperatures vary slightly in the literature. We refer to the temperatures measured by Cao *et al.*[121] since our $SmFeO_3$ samples originate from the same source.

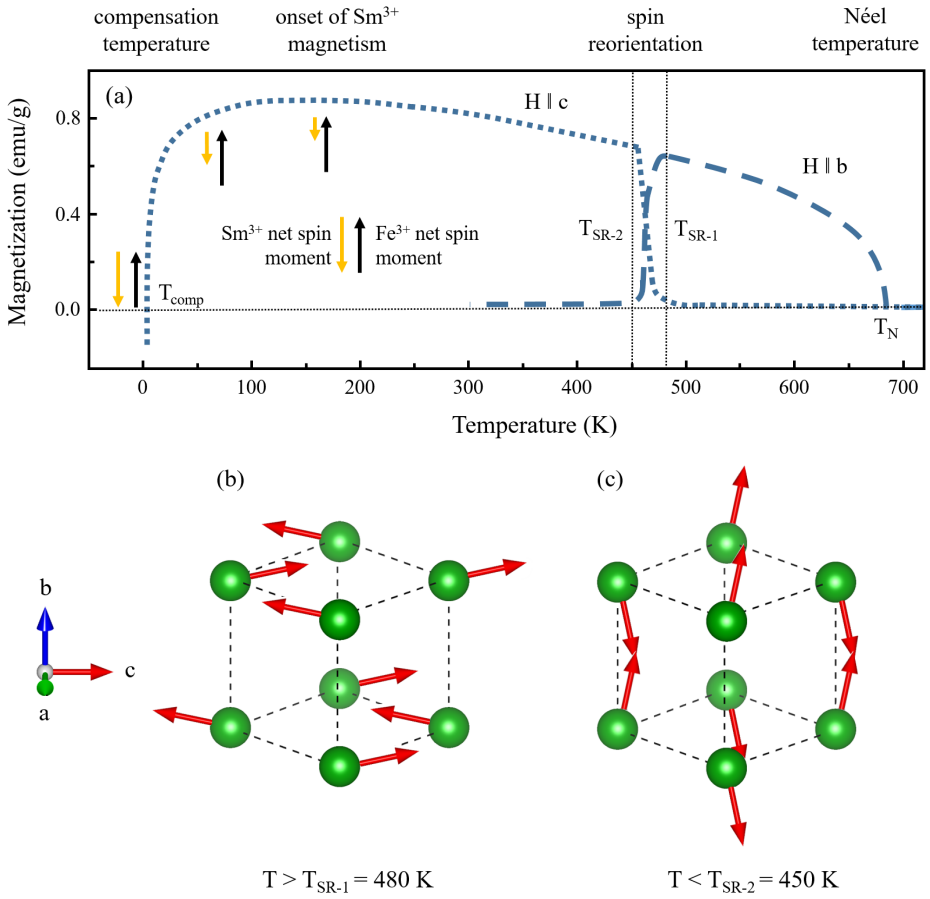

Figure 4.1: (a) Temperature dependent magnetization of $SmFeO_3$. Dashed and dotted lines show the magnetization along b- and c-axis, respectively. Black and yellow arrows represent the net magnetic moment of the Fe^{3+} and Sm^{3+} sublattices, respectively; the length of the arrow indicates the strength of the magnetization. T_N, T_{SR-1}, T_{SR-2} and T_{comp} indicate the Néel temperature, start and end temperature of the spin reorientation and the compensation temperature. Reproduced from Ref. 121. Spin structure of the Fe^{3+} sublattice above (b) and below (c) the spin reorientation [118].

earth spins can be either parallel or antiparallel to the net magnetic moment of the iron sublattice [120]. Antiparallel spin ordering can lead to a compensation temperature T_{comp} where the magnetic moments cancel and the net magnetic moment becomes zero [13,120].

Samarium ferrite is the only rare-earth orthoferrite with a spin reorientation at such high temperatures. For other members of the orthoferrite family the

iron spins reorientate below room temperature (such as $NdFeO_3$: T_{SR-2} = 170 K to T_{SR-2} = 107 K[150]; $ErFeO_3$: T_{SR-1} = 96 K to T_{SR-2} = 87 K[13], $TmFeO_3$: T_{SR-1} = 93 K to T_{SR-2} = 85 K[151]) or do not show a spin reorientation such as the magnetically inert cations La^{3+}, Y^{3+} or Lu^{3+} but also $GdFeO_3$ or $EuFeO_3$[13,120].

The onset of the long range ordering of the Sm^{3+}-Sm^{3+} spin-sublattice at lower temperature is found at $T_{Sm^{3+}}$ = 140 K by Marshall et al.[122] and at $T_{Sm^{3+}}$ = 135 K by Jeong et al.[149] (indicated by the smallest yellow arrow in Fig. 4.1). The onset of this ordering was determined as the temperature at which the net magnetization decreases.

The reported ordering temperatures of the samarium sublattice is high in comparison to other $R FeO_3$ which order commonly below 10 K[13]. To the best of our knowledge, to date neutron measurements have only been reported above room temperature[19]. Low temperature neutron scattering data could reveal more information about the ordering temperature and the exact structure of the samarium sublattice.

With decreasing temperatures the Sm^{3+} magnetic moment increases leading to a compensation temperature at T_{comp} = 3.9 K where the net magnetic moments of the iron and the samarium sublattices compensate[121]. For temperatures lower than T_{comp} the magnetic moment reemerges with opposite sign[121,149]. This behavior shows that samarium and iron net magnetic moments order antiparallelly.

Zhao and co-workers proposed a model that explains the antiparallel ordering of Sm^{3+} and Fe^{3+} by a trilinear coupling process of the magnetic moments of samarium and iron and the octahedra tilt system. Following this coupling mechanism, they suggest a C_yF_z[†] magnetic ordering of the Sm^{3+} spin sublattice for a given $(C_xG_yF_z)$-Fe^{3+} spin structure as in the present case[120]. This spin system has been confirmed by DFT calculation for $NdFeO_3$ showing identical magnetic properties as $SmFeO_3$[150], which makes it likely that both materials shared the same magnetic structure. However, to prove this argument, DFT calculation and low-temperature neutron-scattering experiments for $SmFeO_3$ are necessary.

[†]The notation of the magnetism is such that the magnetic structure is given with respect to the projections of the spin moments along the three spacial directions indicated by the subscript.

4.2 $SmFeO_3$ samples

The $SmFeO_3$ samples used in this study are identical with those discussed in section 3.2 crystallizing in the orthorhombic *Pnma* structure (see section 3.1). Fig. 4.2 shows images of the three samples oriented along the three crystallographic axes recorded by an optical polarized-light microscope. Independent of the orientation of the light polarization to the crystalline axes, the image of the crystals remain unicolor indicating the mono-domain state of the crystals. The orientations were confirmed by X-ray diffraction.

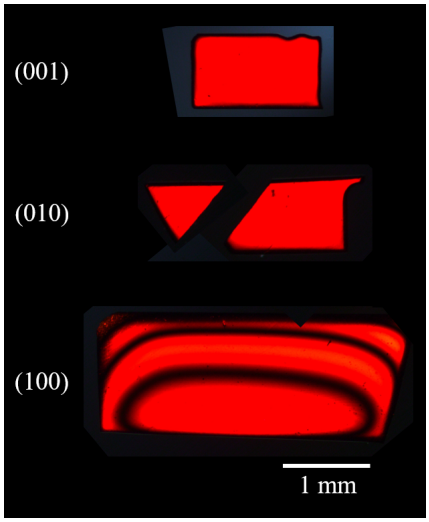

Figure 4.2: Image of $SmFeO_3$ samples oriented along the three orthorhomic axes as indicated in the image recorded by on optical polarized-light microscope. The rings of the (100) oriented sample are interference fringes due to different thicknesses of the sample.

4.3 Results

In this section, the experimental observations are described for each measurement technique over the full investigated temperature range. The discussion of these results will follow in section 4.4.

4.3.1 Raman scattering

The room temperature Raman spectra of $SmFeO_3$ were presented in the previous chapter in Fig. 3.4. To study the impact of temperature changes, notably when passing through magnetic-ordering temperatures, the $SmFeO_3$ crystals were measured in $X(ZZ)\overline{X}$, $Z(YX)\overline{Z}$, $Y(XZ)\overline{Y}$ and $X(YZ)\overline{X}$ configurations to probe the A_g, B_{1g}, B_g and B_{3g} modes, respectively, in a temperature range from 78 to 853 K.

The evolution of the samarium ferrite vibration bands with the temperature is presented for six A_g, four B_{1g}, five B_{2g} and B_{3g} modes in Fig. 4.3(a) - (d). Fig. 4.3(e) and (f) depict the evolution of the band position and FWHM of silicon as a reference to visualize the 'ideal' evolution under the absence of structural anomalies.[‡]

High-temperature range

First, we inspect the range of Néel temperature T_N and spin reorientation temperatures T_{SR-1} and T_{SR-2}. Fig. 4.4 shows the evolution of the band positions and FWHM of the $A_g(3)$ and $A_g(4)$ modes from 300 to 860 K. In this temperature range the band positions evolve without any anomaly or deviation from a standard behavior. In particular, no anomalous behavior can be found at T_N and T_{SR-1}/T_{SR-2}. This situation is found for all Raman-active vibration modes. However, the FWHM, which represents the damping of the phonon mode, experiences a decrease after T_N. More remarkable is the step-like change in the spin reorientation regime to higher FWHM. This behavior is not reflected in all Raman modes and is most pronounced in the here presented $A_g(3)$ and $A_g(4)$ modes. Overall, the ordering processes of the iron spin moments do not appear to have a strong effect on the Raman spectrum.

[‡]With increasing temperature the band position and FWHM decreases and increase, respectively. The shape of these evolutions is explained by temperature dependent anharmonic terms of the potential in Eq. 1.22[152]. Cubic and quadric terms give rise to a damping constant Γ (see Eq. 1.18). The damping constant depends on the temperature and leads the changes in frequency and FWHM.

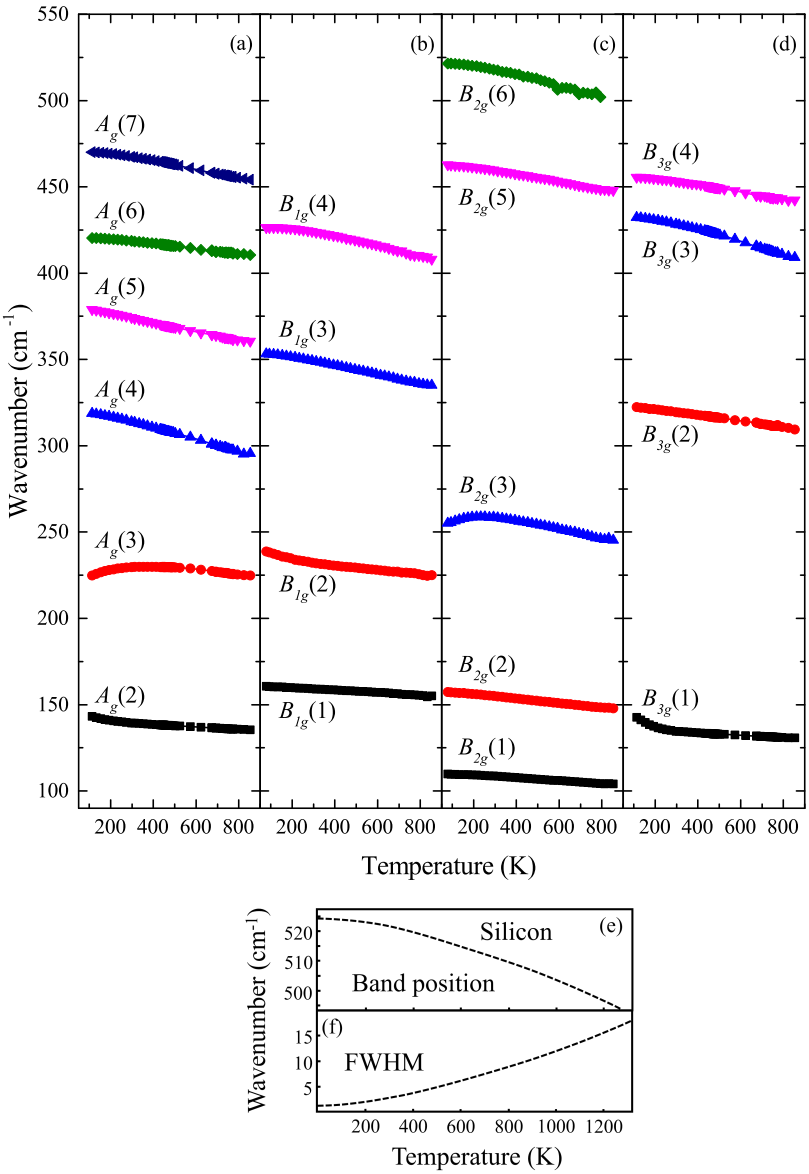

Figure 4.3: Evolution of vibrational modes of (a) A_g, (b) B_{1g}, (c) B_{2g} and (d) B_{3g} symmetry with the temperature. As reference of an evolution without anomaly, the temperature evolution of band position and FWHM of silicon is given in (e) and (f), respectively.

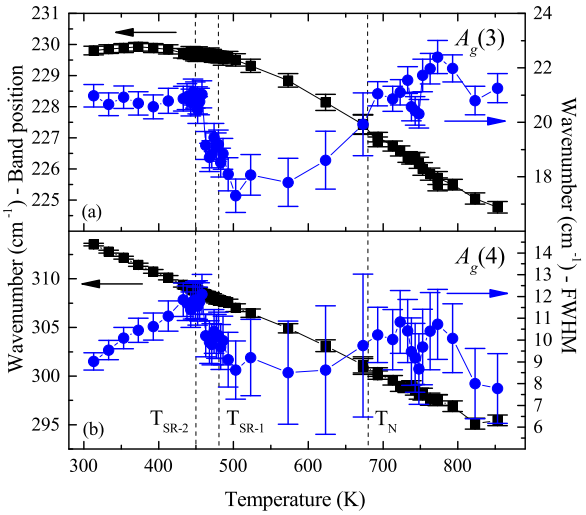

Figure 4.4: Evolution of the band position and FWHM of the $A_g(3)$ and $A_g(4)$ modes in the temperature range from 300 to 900 K.

Last, around 740 K, the FWHM for both peaks shows a small but well-defined dip, that does not correspond to any reported anomaly. This signature may appear tiny, however, anticipatorily it should be mentioned that an anomaly is found in the same temperature region by RUS discussed below.

Phonon anomalies at low temperatures

Now, we have a closer look at the low temperature region of the Raman spectra. Fig. 4.3 already indicates changes of the spectral positions of certain bands towards lower temperatures. Fig. 4.5 presents the Raman modes showing the most significant changes at low temperature (other bands show no or a change at the limit of the spectral resolution). There are two types of anomalies in comparison with the above described model-silicon:
(1) The evolution of band positions of the $B_{3g}(1)$ (a), $A_g(2)$ (b) and $B_{1g}(2)$ (c) show a sudden increase in slope.
(2) The band position of the $A_g(3)$ (d) and $B_{2g}(3)$ (e) modes decrease towards lower wavenumbers.
(3) The FWHM of $B_{3g}(1)$ mode shows a clear maximum at the turning point of the band position. The anomalies of other bands are not pronounced in the FWHM.
The dashed vertical line labeled $T_L = 223$ K (where 'L' stands simply for

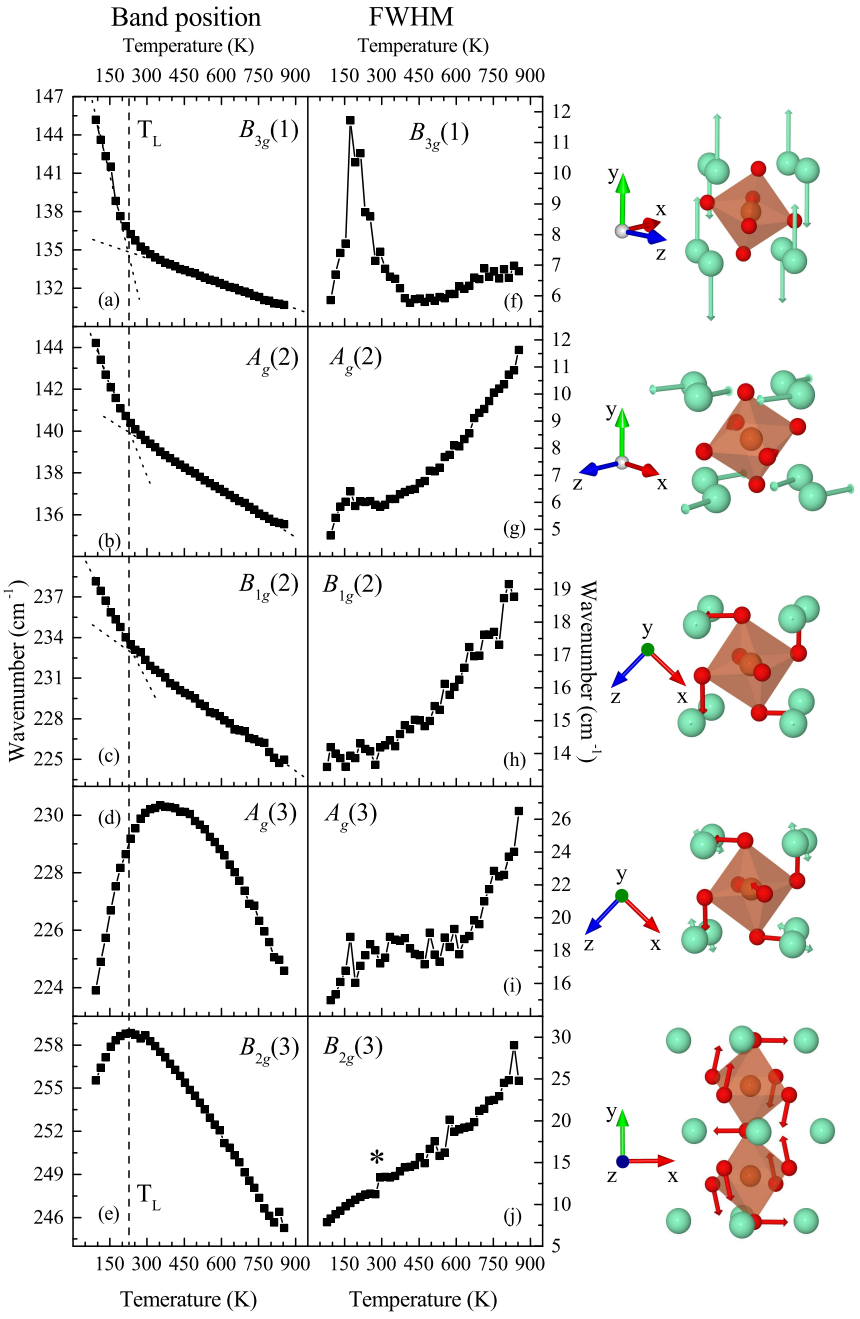

Figure 4.5: Temperature dependence of band positions (a)-(e) and FWHM (f)-(j) for five different vibration bands showing an anomalous evolution at low temperatures. In addition, the corresponding vibrational displacements are shown on the right. [The asterisk in (j) indicates a jump which is due to the fitting of a neighboring additional band.]

'low') in Figs. 4.5(a)-(e) indicates the possible temperature that corresponds to the appearance of the anomaly. T_L was determined as the intersection point of the linear interpolations of the regime before and after the change in slope in Figs. 4.5(a)-(c) (indicated by dotted lines) and at the same time represents the point of inflection of mode $B_{2g}(3)$ (Fig. 4.5(e)). This is at variance with the changes of the $A_g(3)$ mode which shows a point of inflection at 350 K.
All five bands shown here include Sm^{3+} displacement as discussed in chapter 3 (see in particular Table 3.3). The lower lying $B_{3g}(1)$ and $A_g(2)$ modes are pure samarium vibration modes along the y- and z-axis, respectively (see Table 3.3). $B_{1g}(2)$, $A_g(3)$ and $B_{2g}(3)$ are all octahedral rotation modes with a significant contribution of samarium displacement. Vibration modes higher than 300 cm^{-1}, which are dominated by oxygen displacements do not show any sign of anomalous behavior towards low temperatures.

Emergence of new peaks at low temperatures

In addition to the anomalous behavior of certain vibrational bands, we find three new, polarization-dependent peaks appearing in the Raman spectra at low temperatures. Fig. 4.6 presents Raman spectra for $Y(XZ)\overline{Y}$ and $Z(XY)\overline{Z}$ configuration at 78 K and at room temperatures. The features at 115, 135 and 287 cm^{-1} (values for 78 K) are characterized by a broad and asymmetric shape in particular when comparing with the neighboring, sharp vibrational bands. Fig. 4.6(e) and (f) illustrate the evolution of the features at 135 and 287 cm^{-1} with temperature. In both cases the intensity decreases drastically with increasing temperature (Fig. 4.6(e)) such that the features are not longer observable above 153 K and 213 K for the 135 and 287 cm^{-1} bands, respectively. In order to quantify this evolution, the integrated intensity of the feature at 287 cm^{-1} normalized to the vibrational mode at 255 cm^{-1} was plotted against temperature (Fig. 4.6(f) black squares). The ratio decreases strongly from roughly 1.4 (78 K) to 0.4 at 213 K where the presence of this peak can only be guessed from the asymmetric baseline of the neighboring vibrational band at 255 cm^{-1}. It is, thus, difficult to determine a clear temperature for the appearance of these additional features. From the visual inspection of the spectra we approximate a rising of the new bands below 213 K. In Fig. 4.6(f) (blue circles) we also find a strong shift of this band of more than 10 cm^{-1} over 200 K.

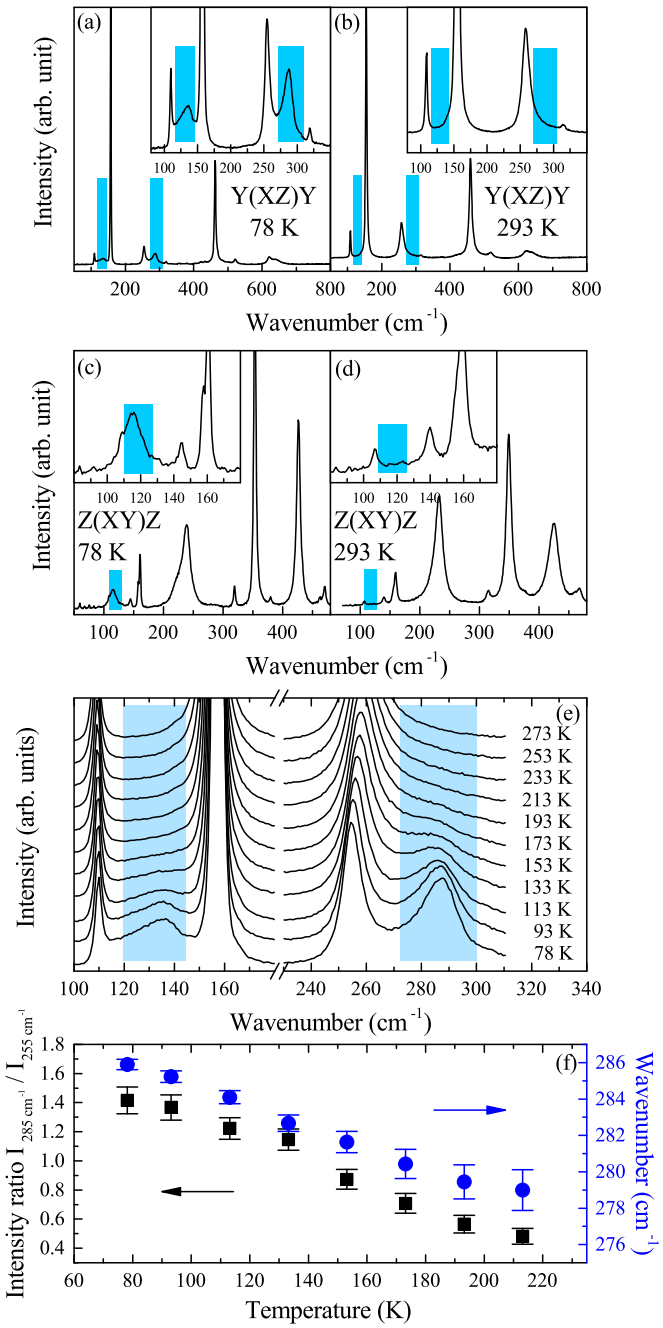

Figure 4.6: Raman spectra for Y(XZ)$\overline{\text{Y}}$ ((a) and (b)) and Z(XY)$\overline{\text{Z}}$ ((c) and (d)) configuration at 78 and 293 K, respectively. The insets give close-ups of the spectral region of interest. (e) Temperature dependent Raman spectra in Y(XZ)$\overline{\text{Y}}$ configuration. (f) Intensity ratio of the new peak at 287 cm^{-1} against the Raman mode at 255 cm^{-1} (black squares) and the evolution of the band position of the additional feature at 287 cm^{-1} (blue dots). The blue bands indicate the additional features.

Magnetic excitations

In a next step, we investigate the temperature dependence of a magnetic excitation (magnon) of the iron sublattice. The first-order magnon spectrum has been investigated in detail above room temperature by White and co-workers and the evolution around the spin reorientation and the T_N is well-known[118]. In principle, $SmFeO_3$ possesses, like all orthoferrites, two magnon branches originating from the ordered iron spin lattice[118]. However, the single-magnon band at lower frequency is difficult to detect due to its low intensity and frequency[118]. Fig. 4.7 shows the temperature evolution of high frequency magnon band extending the work of White *et al.* towards lower temperatures. We find a linear increase of the magnon frequency with decreasing temperatures. No anomalies are found in the magnon spectra of the iron-spin lattice.

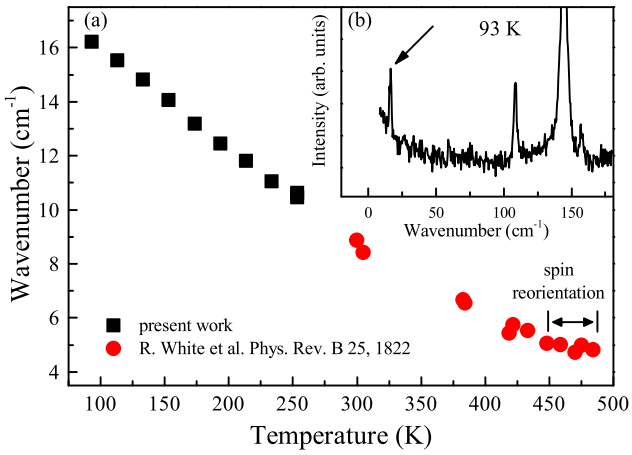

Figure 4.7: (a) Temperature dependent evolution of the first-order magnetic excitation at 16 cm^{-1} (at T = 93 K). The data represented by black squares and red circles are from this work and data taken from literature[153], respectively. (b) Low frequency Raman spectrum at 93 K. The arrow indicates the magnetic excitation band.

4.3.2 Resonant ultrasound spectroscopy (RUS)

Fig. 4.8 shows an excerpt of the RUS spectra of $SmFeO_3$ from 290 to 703 K. There are several mechanical resonance peaks visible in this range, such as the bands at 968, 1045 and 1130 kHz (values for 290 K), but also features that originate from the internal resonance of the experimental setup, for example in region between 950 and 980 kHz or 1110 and 1135 kHz. All mechanical resonance peaks are shifting to lower frequencies for increasing temperatures. Interestingly, in the temperature regime of the spin reorientation T_{SR} the mechanical resonance peaks experience a very strong shift. At T_N there is no such deviation observable at first sight.
We start inspecting the high temperature region in detail including T_N and T_{SR} before focusing on the low temperature region. Anticipatively, it should be mentioned that the particularities of the resonance bands presented in the following figures are common to all resonance bands in the spectra. The

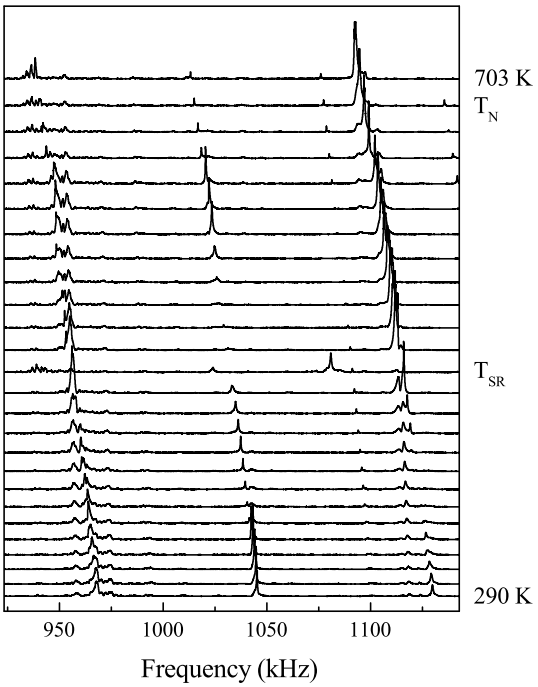

Figure 4.8: Temperature dependent RUS spectra of the high temperature region from 290 to 703 K. T_N and T_{SR} indicate the Néel and spin reorientation temperatures. The spectra are spaced in proportion to the measurement temperature.

bands were chosen for absence of interfering peaks of the measurement setup. The measurement setup for high and low temperature measurement is not the same and crystals of different shapes were used. Therefore, the resonant frequencies for high and low temperature measurements are not the same.

Néel temperature region

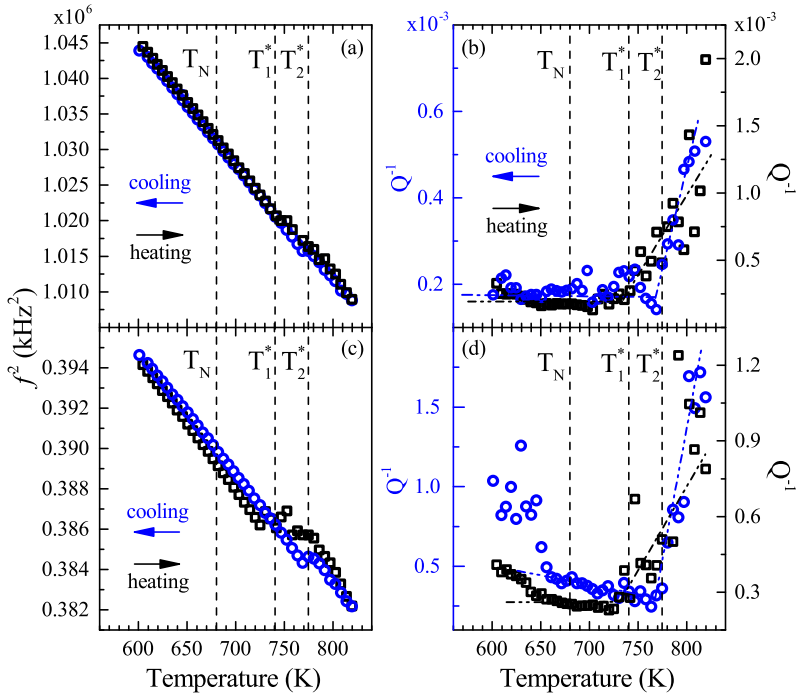

Figure 4.9: Temperature evolution of f^2 ((a) and (c)) and Q^{-1} ((b) and (d)) of the resonance bands at 628 and 1022 kHz (at 581 K), respectively, from 580 to 800 K. Black squares represent to data of the heating process, blue circles the data for cooling. T_N refers to the Néel temperature; T_1^* and T_2^* are discussed in the text.

Beginning with the highest temperature region, f^2 and Q^{-1} for two different mechanical resonance peaks (where f is the mechanical resonance frequency and Q the quality factor of the peak defined in Eq. 2.9) at 1022 and 628 kHz are presented in Fig. 4.9(a and c) and (b and d), respectively, in a temperature range from 594 to 820 K. Both bands change linearly in f^2 up to about 740 K. No changes are observed at T_N neither in f^2 nor in Q^{-1}. However, we find an anomaly at higher temperatures: f^2 shows a jump to higher values at $T_1^* = 740\ K$ when heating. This step-like change is accompanied by

an increase of the Q^{-1} parameter. Towards higher temperatures the elastic resonances continue to decrease with the same slope as before the step. When cooling the jump, in this case to lower f^2 values, appears at a higher temperature $T_2^* = 775$ K. This anomaly has, to the best of our knowledge, not been reported before.

Spin reorientation region

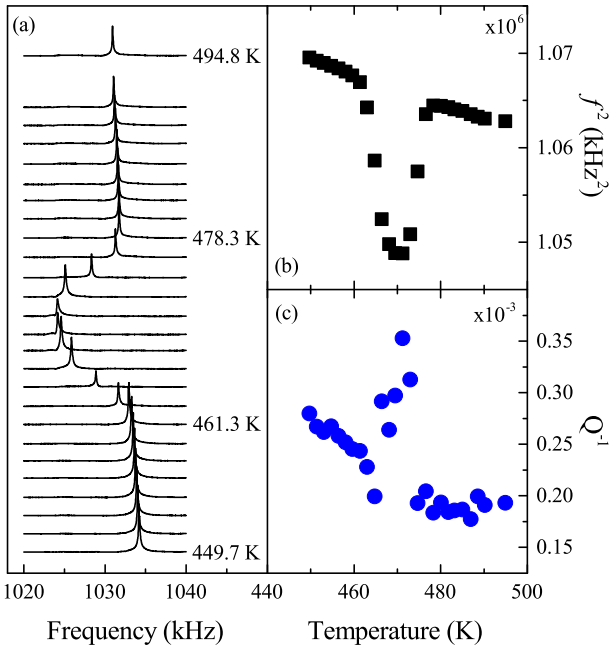

Figure 4.10: (a) RUS spectra, (b) f^2 and (c) Q^{-1} of the temperature range of the spin reorientation for the band at 1034 kHz (value for 449.7 K).

Next, we have a closer look at the spin reorientation region. Fig. 4.10 presents the spectra (a), f^2 (b) and Q^{-1} (c) of the resonance band at 1034 kHz (value for 449.7 K) for the temperature range of 450 to 495 K. Starting from about 461.3 K the band shifts continuously to lower frequencies. The shift is maximal at 470 K. With further increase of the temperature the band position changes back to higher frequencies, until at 478.3 K resuming the linear trend towards lower frequencies. The decrease before and after the transition temperatures, 461.3 K and 478.3 K, follows the same linear slope. The behavior is equally represented by the losses. The damping given by Q^{-1} possesses a maximum between 469 K and 478 K (Fig. 4.10(c)).

Low temperature region

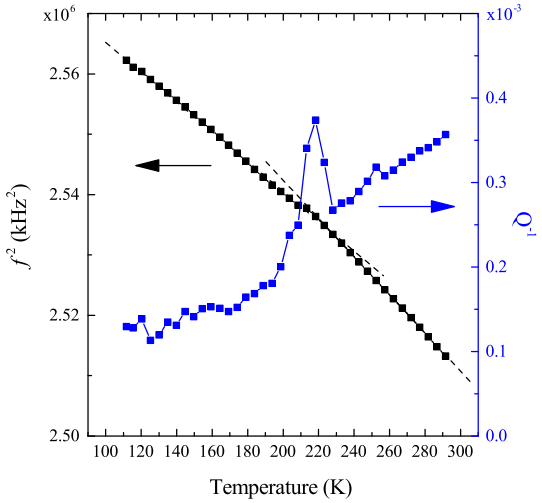

Figure 4.11: Evolution of f^2 (black squares) and Q^{-1} (blue squares) of the resonance band at 1600 kHz for a temperature range between 112 and 292 K.

Fig. 4.11 shows the evolution of f^2 and Q^{-1} of the resonance band at 1600 kHz for a temperature range between 112 and 292 K. The elastic constants associated with this band increase linearly with decreasing temperatures down to 213 K. Here, the evolution reveals a kink between two linear evolutions. The different slopes on either side of the kink are indicated by dashed lines in Fig. 4.11. The change in slope is accompanied by a maximum of the Q^{-1} parameter. The kink is observable in most resonance bands, however the maximum in Q^{-1} is not seen for all bands. In general the observed change at low temperatures is very small and at the limit of detection.

4.3.3 Birefringence measurements

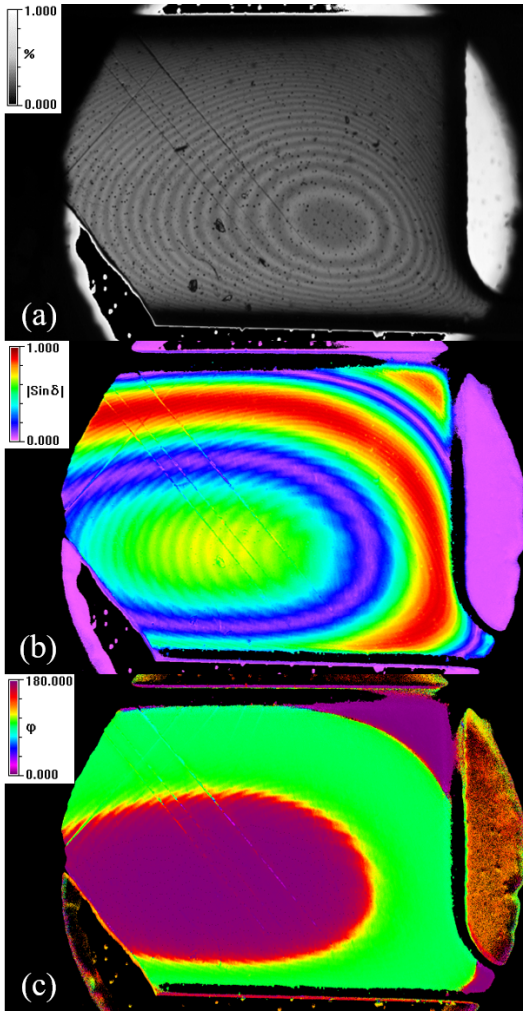

Figure 4.12: Metripol measurement of a $[010]_o$ oriented $SmFeO_3$ crystal at 83 K, where (a), (b) and (c) are the images for intensity I_0, $|\sin\delta|$ and orientation ϕ, respectively.

We performed birefringence measurements on all three crystalline orientations for a temperature range from 83 to 303 K. Following the introduction to birefringence in section 2.2, birefringence measurements give access to three parameters: the transmitted intensity, the orientation ϕ and the birefringence Δn, in form of $|\sin\delta|$ with $\delta = \frac{2\pi}{\lambda}\Delta nL$. Fig. 4.12 depicts the measured quantities for the $[010]_o$-oriented sample at 83 K. In the intensity image (a) the shape of the sample is illustrated best. The interference fringes

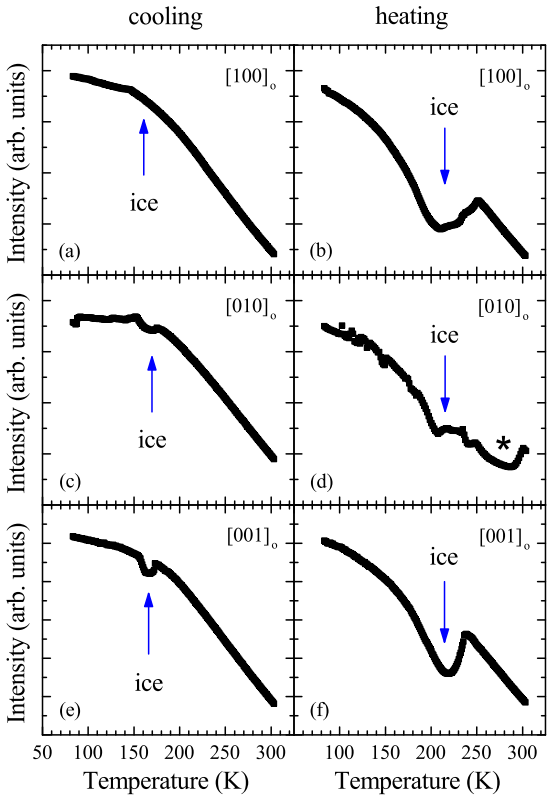

Figure 4.13: Intensity I_0 as a function of temperature for the three crystalline orientations for cooling (left) and heating processes (right). The arrows indicate the formation or disappearance of ice crystals on the sample surface leading to artifacts in the measurement. The asterisk is discussed in the text.

are due to the fact, that the sample is not perfectly flat on the sample holder and the reflections between both are causing the fringes. The smaller and bigger spots on the sample surface are ice-crystals and dust particles.
In Fig. 4.12(b) $|\sin\delta|$ is given in a colour scale from 0 to 1. In a mono-domain crystal only one birefringence value is expected. However, since δ depends on the thickness, the change in value of $|\sin\delta|$ is due to a continuous thickness change from the (approximate) center of the sample to the edges. Same accounts for the orientation ϕ in Fig. 4.12(c); because both values are calculated in dependence on each other (see Eq. 2.7), the orientation shows a jump of 90° when $|\sin\delta|$ goes to zero. During temperature dependent measurements the birefringence changes, such that the ring-like shapes in (b) and (c) move accordingly. Depending on the region of interest and temper-

ature range, these changes are reflected by 90° jumps in ϕ and a zig-zag-like shape in Δn with minima for $|\sin\delta| = 0$ and maxima for $|\sin\delta| = 1$. As discussed in section 2.2, these changes do not have any physical meaning and reflect only the uneven thickness of the sample. It is only possible discuss the trend of the birefringence but not the exact values.
For the temperature span of the experiments, it was not possible to choose an area that does not exhibit a jump in ϕ and zero/one transition in $|\sin\delta|$. Therefore, the region of interest in the images of the sample was chosen such that the 90° jump and zero/one-crossings in $|\sin\delta|$ appears at a temperature which does not coincide with anomalies found by Raman spectroscopy and RUS. (This will be more illustrative when discussing the evolution with the temperature below.)

The intensity evolution with the temperature is given in Fig. 4.13: (a), (c) and (e) present the cooling (b), (d) and (f) the heating processes for crystals of the three different orthorhombic directions. The intensity shows a general trend towards lower transmission for higher temperatures reflecting a stronger absorption of the light for higher temperatures. Intensity curves differ significantly for cooling and heating. This is due to the formation of ice on the sample surfaces. Since the liquid-to-solid (or gas-to-solid) phase transition is of first-order, we find the formation at different temperatures when heating or cooling. The shape of the heating curve of the $[010]_o$ shows more irregularities (see asterisk in Fig. 4.13(d)) which are attributed to changes of the air layer under the sample due to small strain releases between sample and sample holder.
Since effects extrinsic to $SmFeO_3$ dominate the intensity change with the temperature, no conclusions can be drawn from the intensity.

Fig. 4.14 presents the orientation of the axes of the indicatrix in dependence on the temperature. The orientation can be seen as constant for all crystallographic orientations for both heating and cooling processes. Only towards room temperature the orientations change over a short temperature range by 90°. This is an effect arising from the numerical determination of the quantities, intensity I_0, orientation ϕ and $|\sin\delta|$, and has no physical meaning, as mentioned above and in section 2.2. No indications for a phase transition that involves an orientation change of the crystalline axes are found.

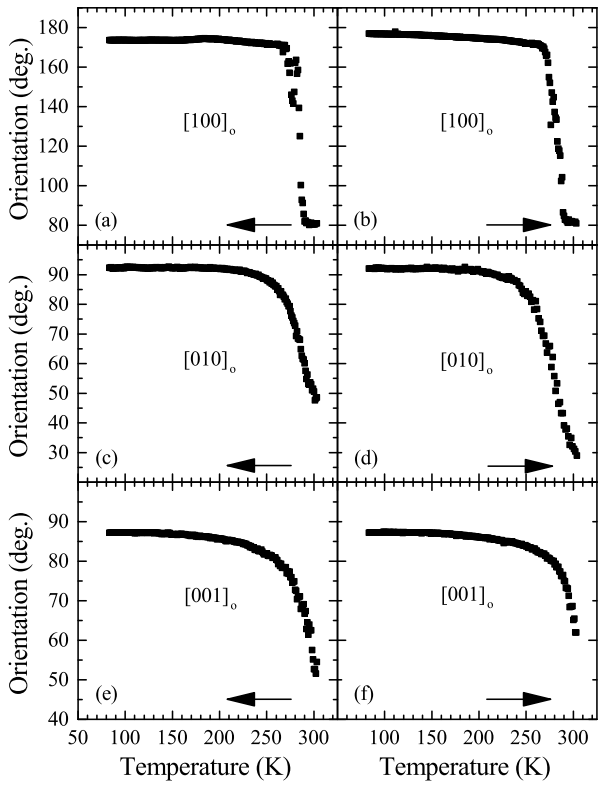

Figure 4.14: Evolution of the orientation ϕ of the indicatrix with temperature of the three crystalline orientations for cooling (left) and heating processes (right).

In Fig. 4.15 the changes of the birefringence Δn are presented for the three crystal orientations for heating and cooling procedures.
Δn changes linearly with temperature for the absence of anomalies. That means both sides of the minimum-point should be symmetric according to $|\sin\delta|$. To visualize small deviations from an unperturbed trend, the symmetric evolution is indicated by blue lines in Fig. 4.15. By this means, a slight deviation of the symmetric birefringence evolution can be observed for the crystal oriented in $[100]_o$-direction (Fig. 4.15(a) and (b)). This indicates a change in the y-z plane of the orthorhombic unit cell. For the $[010]_o$-oriented crystal (Fig. 4.15(c) and (d)) we find a distinct deviation from the linear curve characterized by a clear change in slope. This deviation points to a change in the x-z plane. The birefringence of the $[001]_o$-oriented crystal (Fig. 4.15(e) and (f)) shows a change with a constant slope on either side of the discontinuity. Since changes in the birefringence represent the variations

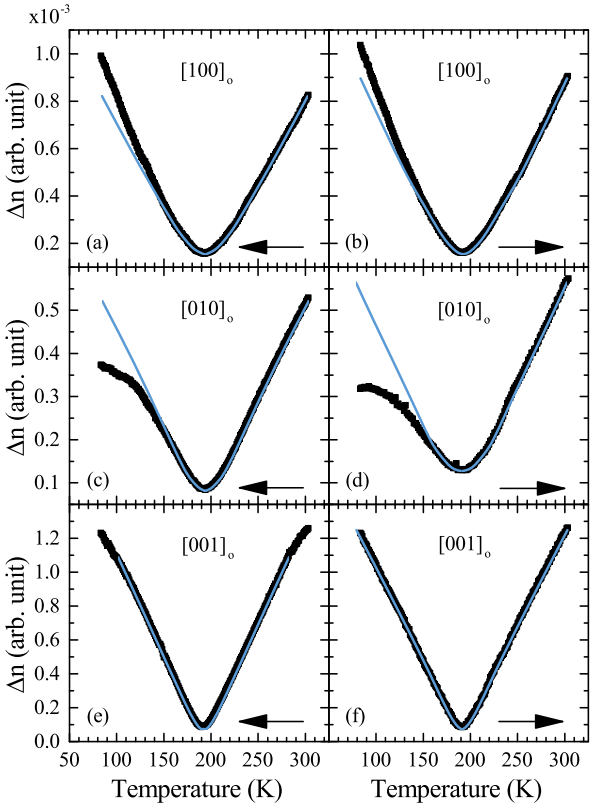

Figure 4.15: Evolution of the birefringence Δn with temperature of the three crystalline orientations for cooling (left) and heating processes (right). The fine blue lines indicate an undisturbed linear change of Δn by mirroring the evolution from 300 K to the minimum to the low temperature part.

in the plane perpendicular the sample orientation, this indicates that the x- and y-axis changing evenly with the temperature.
We can conclude, that there is a small but distinct change in slope of the birefringence for crystal orientations that enable to probe a plane that includes the z-axis. x- and y-axis do not appear to be affected. The homogeneous change of the birefringence is substantially stronger for the orientations $[100]_o$ and $[001]_o$ when compared to the $[010]_o$ direction.
For all orientation $SmFeO_3$ behaves in the same way for heating and cooling processes.
Since the deviation is not abrupt it is difficult to determine a clear onset temperature. We approximate the onset temperature around 150 K.

4.4 Discussion

Fig. 4.16 summarizes the anomalies probed by Raman spectroscopy, RUS and birefringence measurement in the present study and the magnetic transitions reported in literature. Now, we discuss the different findings reported above grouped by (i) known phenomena such as Néel temperature and spin reorientation and (ii) unknown phenomena, i.e. the anomalies at high and low temperatures.

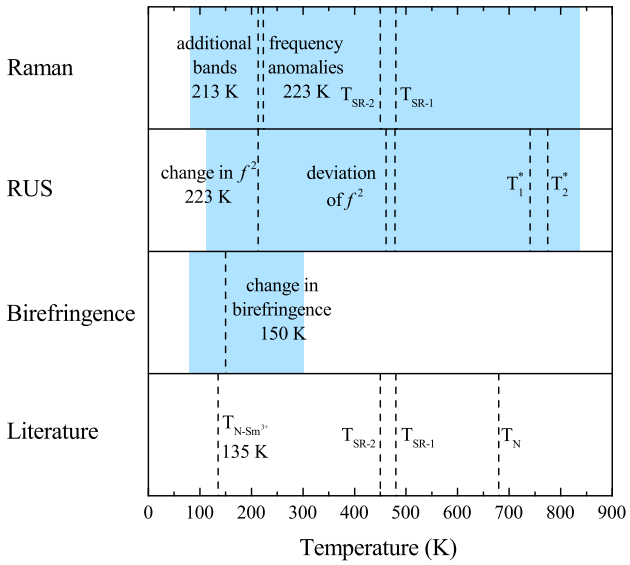

Figure 4.16: Summary of the anomalies found by Raman spectroscopy, RUS and birefringence measurements compared to known phenomena reported in literature. The blue zones indicate the temperature range that has been investigated for each technique.

4.4.1 Impact of the spin ordering at T_N (680 K) on the lattice

At the magnetic ordering temperature $T_N = 680$ K of the Fe^{3+} spins, there are no changes found in f^2 and Q^{-1} of the RUS data. For few selected Raman bands a change in the line width can be appreciated. However, none of the reported Raman active modes shows discontinuity of the vibration frequency at the transition point. We can therefore assume the spin-lattice interaction to be very weak in $SmFeO_3$ for the ordering of the iron spin moments.

$SmFeO_3$ possesses the *Pnma* structure for high temperatures, down to room temperature. Thus, when the Fe^{3+} spins order, the crystalline symmetry remains unchanged and the iron ions remain in the same position. Whilst the oxygen and samarium ions have a certain freedom in position in the *Pnma* lattice the iron ion possess a distinct position (see Table 3.1). A displacement from its position would immediately lead to a breaking of symmetry. Therefore, the spin ordering at T_N is not related to a displacement of the iron ions.
However, it is expected that the spin interactions, as a result of the spin ordering, impact the elastic constants and the vibration frequencies. Spin-phonon coupling processes have been widely reported in materials structurally close to $SmFeO_3$ such as orthomanganites ($R MnO_3$)[136,154,155] or orthochromites ($R CrO_3$)[156–158]. It was found that the rare-earth cation is of importance for the spin-phonon coupling strength[136,156]. As mentioned earlier (see chapter 3) the B cations occupy a center of inversion symmetry in the *Pnma* structure. Therefore, only vibrational displacements without iron contribution are detectable by Raman spectroscopy. This means in turn that only the influence of the iron-spin ordering on the rest of the lattice can be probed by Raman spectroscopy. Fe^{3+} is a Jahn-Teller inactive ion due to its half filled 3d orbitals (Fe^{3+}: $[Ar]3d^5 4s^0$)[159] leaving the FeO_6 octahedron undistorted at difference to the Jahn-Teller active cations Mn^{3+} ($[Ar]3d^4 4s^0$) [and Cr^{3+} ($[Ar]3d^3 4s^0$)]. Loosely speaking, we may assume that the B-cation spins communicate through the Jahn-Teller effect with the oxygen anions. This coupling process is comparably weak in $SmFeO_3$ without Jahn-Teller effect. Thus, the mediation of the iron spin ordering to the rest of the lattice can be considered little and the spin-phonon coupling is thus consistently below the detection limit of Raman spectroscopy.
The same reason can be assumed for the absence of an anomaly at T_N in the RUS data. Since the reported anomaly of $Sm_{0.6}Y_{0.4}MnO_3$ at T_N is weak[160], it does not come surprising that the magnetic ordering of Fe^{3+} spins is not reflected in the elastic constants based on the proposed scenario.

In summary, the magnetic ordering of the Fe^{3+} spins at the T_N has no measurable impact on the crystal lattice. This could be explained by a negligible electro-elastic coupling of the Jahn-Teller inactive iron ions.

4.4.2 Anomalies during the spin-reorientation (450 - 480 K)

During the spin reorientation between T_{SR-1} = 480 K and T_{SR-2} = 450 K the antiferromagnetic spin moments rotate continuously from the c-axis to the b-axis[13].
The Raman spectra reflect this behavior only by an increase in linewidth. This can be understood by the lack of sensitivity to iron displacement in the *Pnma* structure following the scenario at T_N described above.
On the other hand, the RUS data show a strong deviation during the spin reorientation. This experimental finding points towards a general softening of the elastic constants of $SmFeO_3$ during the spin reorientation through a change in magnetoelasticity.
Reports on magnetostrictive effects under an external magnetic field seem indeed to support a general softening of the lattice[161]. Size changes of the crystal under a magnetic field appear only between T_{SR-1} and T_{SR-2}. The magnetostrictive effect depends strongly on the degree of rotation of the spin system. Approaching the spin reorientation regime from high temperatures, an elongation of the x- and z-axis and a shortening of the y-axis are found for a magnetic field along the z-axis. Half way through the reorientation process, this magnetostriction drops to zero, whereas for a magnetic field along the y-axis a magentostriction arises with opposite elongation and shortening properties[161]. While the spin reorientation process is triggered by the Fe^{3+}-Sm^{3+} interaction, the origin for magnetostriction appears to be related to an anisotropy of the Fe^{3+} spins[161]. The strength of the size changes are similarly strong for different rare-earth cations and appear even without a magnetic rare earth such as in $YFe_{1-x}Co_{x/2}Ti_{x/2}O_3$ ($x \leq 0.012$)[161]. The magnetic states for $T > T_{SR-1}$ and $T < T_{SR-2}$ are compatible with the *Pnma* structure[13]. However, it is possible that the symmetry is lowered during the spin reorientation process due to the magnetostriction under an external field[13]. Overall, this shows a sensitivity for structural changes in the spin reorientation regime.
Our Raman spectroscopy results contradict with a report by Chaturvedi *et al.* claiming a change in vibration frequency due to spin-phonon coupling in $SmFeO_3$ at T_N and T_{SR}[162]. However, the published data stems from measurements on powder samples which makes it difficult to distinguish single bands at high temperature. Furthermore, the temperature resolution was too low for an adequate interpretations (i.e. insufficient data points).

In conclusion, the spin reorientation regime is accompanied by a softening of the lattice, well identified in the RUS data but less pronounced in the Raman spectra. This lattice softening opens perspectives for exploring of coupling phenomena.

4.4.3 High temperature anomaly ($\sim$ 740 K)

The high temperature anomaly is tiny, but consistently observed both in Raman spectroscopy and RUS. In RUS measurements the anomaly appears at $T_1^* = 740$ K and $T_2^* = 775$ K for heating and cooling, respectively. It shows a hysteresis-like behavior. However, it is surprising to find that the temperature of the anomaly is lower for the heating process than for the cooling process. Classical first-order transitions show an inverse behavior where the structure remains in its state to higher or lower temperatures for heating or cooling, respectively (see e.g. $BaTiO_3$ [163]). Furthermore, a drastic phase change is unlikely since f^2 evolves with the same slope before and after the jump. Q^{-1} increases strongly above T_1^* and T_1^*, indicating a freezing of loss mechanisms below the transition temperatures. Interestingly, the FWHM of the Raman data shows a small but distinct minimum in the same temperature range.
This behavior was, to the best of our knowledge, never reported before and is not observable as changes in the lattice constants at high temperatures reported by Kuo *et al.* [19]. Measurements reported in literature where rarely performed at such high temperatures, so that it is possible that this anomaly has just been overlooked. However, further measurements sensitive to subtle structural changes need to be performed to confirm the existence of this anomaly, as well as its origin.

4.4.4 Low temperature anomalies ($\sim$ 220 K)

The low temperature region is rich in anomalies which have to the best of our knowledge not been reported so far. The deviations in f^2 and Q^{-1} from the RUS measurement and Δn in the birefringence data are small but distinct. In contrast, the changes in the Raman spectra are pronounced. From the literature, we know that the ordering of the Sm^{3+} spins give a measurable contribution to the net magnetization from about 135 to 140 K [122,149].
The onset of the anomalies found in the Raman spectroscopy and RUS data lies by 213 to 223 K, significantly higher than the literature data from the magnetic measurement, whereas the deviation of birefringence appears in the

vicinity of the reported ordering temperatures. The onset of spin-phonon coupling in Raman spectra has often been reported to occur at temperatures significantly higher than T_N [136,154]. However, it is unclear at this stage why the anomaly in the RUS data coincides with the Raman data whereas the deviation of the birefringence appears at lower temperatures. Since the appearance of the anomalies in all measurement techniques including magnetic measurements in literature is rather gradual than abrupt, the determination of a clear onset is difficult.
In section 4.3.3 we found that the birefringence changes at low temperatures only if the refractive index alone the z-axis is probed. The z-axis, in turn, coincides with the direction of net magnetization of the Sm^{3+} spin sublattice.
From the Raman data, we can divide vibrational bands that present a deviation from the expected evolution into two groups according to their vibrational displacement (see Table 3.3): the $B_{3g}(1)$ and $A_g(2)$ modes are pure samarium displacements. Modes $B_{1g}(2)$, $A_g(3)$ and $B_{2g}(3)$ represent mainly octahedral rotation displacements with a small samarium contribution (Fig. 4.5). In particular the modes $B_{3g}(1)$ and $A_g(2)$ point to a change in the Sm^{3+}-Sm^{3+} interaction.
Both, Raman and birefringence data indicate that the low temperature anomalies are directly related to samarium. Therefore, we propose to assign the low-temperature anomalies to a spin-lattice coupling due to the ordering of the samarium spin sublattice reported at 135 - 140 K [122,149].

Only two out of the six pure Sm^{3+}-Sm^{3+} vibrations show an anomalous evolution. Depending on the symmetry of the samarium spin sublattice not all of the Sm^{3+}-Sm^{3+} displacements are affected by the spin interactions. It is to be expected that the anomalies of the samarium vibrations are representative for the ordering type of the underlying spin sublattice. That means only vibrational displacements that are affected by the spin-spin interactions show an anomalous behavior.
At first sight, it is less intuitive to relate the change of the octahedra-tilt vibrations $B_{1g}(2)$, $A_g(3)$ and $B_{2g}(3)$ to the spin ordering of the samarium sublattice. However, these changes can be understood by the trilinear coupling model of Fe^{3+} magnetic moments, Sm^{3+} magnetic moments and octahedra-tilt system that leads to the ordering of Sm^{3+} spin system as proposed by Zhao and co-workers [120]. This coupling allows a direct interaction between the Sm^{3+} spins and the octahedra rotations which is reflected in

the octahedra-tilt vibrations in the Raman spectra. Furthermore, according to Zhao *et al.* only specific octahedral rotations are able to couple with the magnetic moments depending on the magnetic system [120]. This may explain that not all octahedra-tilt modes show an anomalous behavior.
To confirm this picture for the anomalies of particular Raman-active modes, the knowledge of the spin structure is crucial which could be acquired experimentally by neutron scattering or theoretically by DFT calculations.

Interestingly, Rovillain *et al.*[164] report a similar anomaly for a low lying phonon mode (around 113 cm^{-1}) in $TbMnO_3$ well-above $T_N(TbMnO_3)$= 42 K. This is surprising inasmuch as T_N is attributed to the ordering of the Mn^{3+} spins. However, since $TbMnO_3$ crystallizes like $SmFeO_3$ in the *Pnma* structure, this phonon mode is a pure Tb^{3+} vibration. The evolution of this Tb^{3+} vibration reported by Rovillain and co-workers is illustrated in Fig. 4.17.

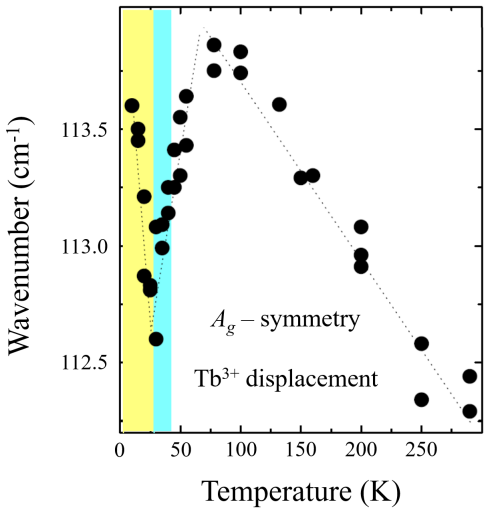

Figure 4.17: Temperature dependent evolution of the band position of a low frequency A_g mode of $TbMnO_3$. Below T_N = 42 K the Mn^{3+} spins order in an incommensurate antiferromagnetic structure depicted by the blue area. The yellow area indicates the temperature range of the cycloidal spin structure. Reproduced from Ref. 164.

Infrared measurements on $TbMnO_3$ [165] and $GdMnO_3$ [154] revealed an anomaly of a low frequency infrared active mode (114 and 116 cm^{-1}, respectively) arising approximately 20-30 K above T_N. For these infrared absorption

measurement the situation is more complex as, in contrary to Raman-active modes of the *Pnma* structure, infrared-active low-frequency modes show certain contribution of B-cation displacements. Nevertheless, these two examples raise the question if the phonon anomalies of the present study are characteristic for $SmFeO_3$ only or if this is a more common phenomenon.

It is interesting to note that, although the anomaly is small, the effect of the ordering of the Sm^{3+} spin sublattice on the elastic constants is more pronounced than the ordering of the Fe^{3+} spins at T_N.

Furthermore, the ordering of the samarium moments does not appear to influence the iron spin lattice. The frequency of the single magnon resulting from the iron-spin sublattice (see Fig. 4.7) evolves linearly at low temperature. Therefore, we conclude that there is no measurable impact of the samarium spin ordering on the iron spins.

In conclusion, the anomalies in the Raman spectra, RUS and birefringence data are assigned to spin-lattice interactions as a result of the magnetic ordering of samarium.

Origin of the new Raman bands

The most striking feature of the low temperature Raman spectra are the additional bands (Fig. 4.6) which appear below 213 K simultaneously with the Raman vibration band anomalies and the kink in the RUS spectrum. Thus, we assume that the new features in the Raman spectrum result from the same origin as the above discussed anomalies.
We discuss three possible sources of the addition features:
(i) new vibration bands,
(ii) samarium crystal-field excitations,
(iii) two zone-edge-magnons.

(i) New bands in Raman spectra are often an indication for a structural phase transition accompanied by a symmetry lowering. If the potential low symmetry structure is a non-polar, new vibrational Raman bands are expected to be similarly sharp and symmetric like the already existing vibrational bands. However, the additional features are highly asymmetric and broad.
On the contrary, oblique modes resulting from Raman-active polar vibra-

tions can show broader shapes. The appearance of oblique modes is correlated with a phase transition away from *Pnma* to a polar space group that allows polar vibration modes to be detectable by Raman scattering. Birefringence measurement show that the orientation of the crystal axis is constant below room temperature down to 83 K. Therefore, only a orthorhombic-orthorhombic phase transition is plausible. The appearance of oblique modes would be a strong indication for the rising ferroelectricity in $SmFeO_3$ induced by the magnetic ordering of the samarium spins. At this point, it is unclear if such a structural changes did not show stronger signatures in further Raman bands, as well as in the birefringence and RUS data.

(ii) Electronic crystal-field transitions have been reported for Sm^{3+} ions earlier in samarium garnets (Sm^{3+}:$Y_3Al_5O_{12}$)[166–168]. The lowest lying absorption bands were found at 146 and 249 cm^{-1}. These values do not perfectly coincide with the frequencies of features in the Raman spectrum, but Raman scattering process may give access to different electronic excitations than absorption spectroscopy[82] and samarium in $SmFeO_3$ is unlikely to behave like Sm^{3+} as an impurity on the garnet matrix. Königstein and co-workers demonstrated Raman scattering on crystal-field excitations and phonon bands simultaneously in terbium aluminum garnet[169]. It was found that terbium crystal-field excitations and vibrational bands of $Tb_3Al_5O_{12}$ overlap in the Raman spectrum which makes a separation difficult. However, the low frequency crystal-field excitations show barely any frequency shift with temperature (approximately 1 cm^{-1} between RT and liquid nitrogen temperature)[166]. In contrast, the new feature in the $SmFeO_3$ spectrum found at 280 cm^{-1}, for instance, shifts significantly with the temperature (see Fig. 4.6(f)). Furthermore, in samarium garnets the crystal-field excitation are measurable at room temperature. The additional features in the $SmFeO_3$ spectra, however, are suddenly appearing towards low temperatures.
Following the spin ordering of the rare earths, R^{3+}-R^{3+} spin interactions have been reported to split crystal-field absorption bands for $ErFeO_3$ or $DyFeO_3$[13,170,171]. This split, however, is weak and with 10 cm^{-1} of much lower energy than the new peaks in the Raman spectrum of $SmFeO_3$.

(iii) Two-magnon bands result from scattering of two magnetic excitations at the zone boundary. Therefore, second-order magnons might be detectable even if the frequency of first-order magnons is below the spectral cut-off.

Two-magnon scattering bands are often found below 300 cm^{-1}. As typical for second-order processes, two-magnon bands show often a broader and asymmetric shape than first-order processes. Strong softening behavior has been reported close to the magnetic transitions. Classical examples for two-magnon processes are NiF_2, $RbMnF_3$ [172,173]. These specifications are in agreement with the properties found for the additional features of $SmFeO_3$ Raman spectra. In addition, the scenario of two-magnon scattering due the Sm^{3+}-Sm^{3+} spin ordering does not necessarily demand a symmetry breaking as it is likely to happen for the above discussed cases.

Overall, it appears to be the most likely scenario that the additional features result from two-magnon scattering. However, polar/oblique modes which may result from a phase transition to a polar structure, can not be fully excluded. On the other hand, crystal-field excitations can be ruled out as source of the new peaks.
Nevertheless, further measurements are necessary to confirm this picture, such as Raman scattering under magnetic/electric field, polarization measurements or zone-edge-magnon neutron scattering.

Interestingly, similar additional bands have been reported in Raman and THz spectra of $TbMnO_3$ [164,165,174]. There are two types of additional bands in $TbMn0_3$, those below 100 cm^{-1} and one feature at about 130 cm^{-1}. Takahashi *et al.* assign these feature as single magnons and two-magnons, for the latter [165]. The ones below 100 cm^{-1} appear at around $T_N(TbMnO_3)$ and indicate a direct relation with the magnetic ordering of the manganese spins. The feature at 130 cm^{-1} starts evolving at much higher temperatures (roughly 100 K higher). The appearance is correlated with the anomaly reported for the phonon mode at 113 cm^{-1}. This behavior is very similar to anomalies found in the Raman spectra of $SmFeO_3$. However, Rovillain *et al.* assign this band (reported here at 125 cm^{-1}) to a crystal-field excitation of terbium [164]. This conclusion is drawn from the fact that no other $RMnO_3$ has been reported to show a comparable feature and thus the band needs to be related to terbium [164]. Fig. 4.18 shows the temperature dependent Raman spectra measured by Rovillain and co-workers [164].
The measurements of the single Fe^{3+} magnon evolution show linear evolution of the magnetic excitation with the temperature. This indicates that the iron-spin system is not affected by the low temperature anoma-

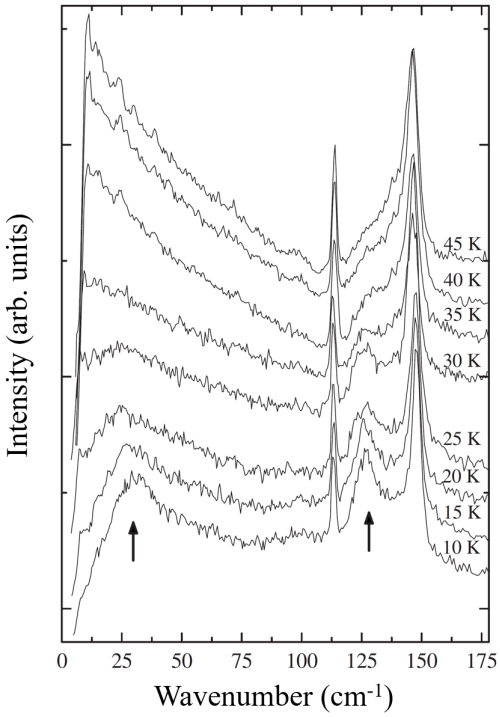

Figure 4.18: Temperature-dependent Raman spectra of $TbMnO_3$ from 10 to 45 K. The arrows indicate two additional features at low temperature. The evolution of the phonon band at 113 cm^{-1} is depicted in Fig. 4.17. Reproduced from Ref. 164.

lies. Transition temperatures of the iron and samarium spin sublattices are well separated, unlike in orthochromites or orthomangaites where the B-site magnetic moments order at low temperatures or other orthoferrites where a spin reorientation appears below room temperature. In the light of the close similarities of the low temperature anomalies of $SmFeO_3$ to $TbMnO_3$ or also $GdMnO_3$, samarium ferrite becomes particularly interesting and may act as a role-model material to understand and disentangle the magnetism arising from A-site and B-site magnetism in similar compounds.

4.5 Conclusion

We have investigated the structural evolution of $SmFeO_3$ by three different analysis techniques over a wide range of temperature. Besides the well-known magnetic ordering at the Néel temperature T_N and the spin reorientation, we found two anomalies, at high and low temperatures, that have not been reported before.
The ordering of iron spins at T_N was found to show barely any signature in the structural probe techniques used in this study. During the spin reorientation, however, the elastic constants soften clearly. In combination with the reported magnetostrictive effect, it is certainly of interest to investigate $SmFeO_3$ for a potential magnetic field induced phase transition in the spin reorientation regime.
The origin of the high temperature anomaly found in the RUS spectra is unclear and demands for further experimental investigations.
We assigned the structural anomalies at low temperature to a spin-lattice coupling of crystalline and magnetic structure due to the Sm^{3+}-Sm^{3+} spin ordering. The additional features were assigned to two-magnon excitations of the samarium spin system. However, polar/oblique modes can not be fully excluded. Further measurements and calculations are desirable to confirm this picture.
In the future, it will be interesting to investigate if the spin-lattice interaction triggered by the samarium spin ordering may lead to a ferroelectric phase at low temperatures.
The similarities between certain features in the Raman spectra of $SmFeO_3$ and $TbMnO_3$ may ask for a detailed re-investigation of the magnetic system of $TbMnO_3$. Since the magnetic transitions of Sm^{3+} and Fe^{3+} are far separated in temperature, $SmFeO_3$ may act as a model system for a better understanding of the spin-lattice interaction which finally gives rise to the multiferroic properties in $TbMnO_3$.

Overall, $SmFeO_3$ shows a rich landscape of lattice anomalies of different origin and coupling strength. These structural instabilities are triggered by different magnetic ordering processes and give rise to a multiplicity of possible coupling phenomena, for example under external fields or under strain in thin films.

Chapter 5

Temperature evolution of the band gap in $BiFeO_3$

The work in this chapter has been published in *Physical Review B* (**93**, 125204, 2016)[175]. Major parts of the following chapter are identical in content and word with this publication.

Introduction

The research topics of multiferroics and photoferroelectrics are currently receiving significant attention. In both research fields bismuth ferrite $BiFeO_3$ is occupying a predominant position, being, on the one hand, the most promising multiferroic material[53,176–179] and, on the other hand, for its above-band gap photovoltages, anomalous photovoltaic effects, photoconductive domain walls etc.[22,23,48,180,181]. Yet, the electronic structure in $BiFeO_3$ in general and its band gap in particular, in spite of their importance for photoferroelectric effects, remain rather poorly understood experimentally and theoretically. According to absorption studies on single crystals[182] and thin films[183–186], the optical band gap at ambient conditions lies at approximately 2.7 eV. It is also experimentally established that the optical band gap of $BiFeO_3$ shrinks with increasing temperature down to 1.3 eV at 1200 K where it then closes abruptly showing an insulator-to-metal phase transition concomitant with a structural transition to the so-called γ-phase[187]. Both, the rapid shrinking of the optical band gap, e.g. three times steeper than in $BaTiO_3$[188], and the insulator-to-metal transition set $BiFeO_3$ apart from conventional non-magnetic ferroelectrics. It is not yet understood how this gradual shrinking of the optical band gap relates

to the electronic structure. One of the reasons for the lack of knowledge is that the experimental investigation of band-to-band transitions is difficult to address experimentally in ferroelectric and multiferroic oxides because the absorption onset is broad, especially when compared to the generally sharp transitions in classical semiconductors. The appearance of Urbach tails, notably at higher temperatures, complicates the quantitative analysis and the discrimination of direct and indirect transitions. Other classical techniques are rapidly limited by thermal effects, charging of the insulating samples (ARPES) or require synchrotron sources (resonant inelastic X-ray scattering). In this section, we make use of resonant Raman scattering as introduced in section 1.2.3. These resonant effects have been investigated in many details in semiconductors[82,93,189,190], but much less in perovskite-type oxides. Electronic transitions have been probed by Andreasson and co-workers involving mainly charge transfer phenomena in $LaFe_xCr_{1-x}O_3$[137–139]. Orbital ordering was investigated in $LaMnO_3$ by Kovaleva *et al.*[191] and Kruger *et al.*[192]. Furthermore, resonant Raman scattering was used as a probe for structural properties in particular in systems of high disorder. Disordered systems display broad Raman bands such that subtle changes can often be masked. In such circumstances resonant Raman spectroscopy was shown useful to selectively enhance certain features of the spectrum and to probe e.g. phase transitions in PZT[193,194] or polar nano-region in relaxor ferroelectrics such as $PbSc_{0.5}Ta_{0.5}O_3$ or $PbSc_{0.5}Nb_{0.5}O_3$[195].

In this section, we aim to shed light on the electronic band structure of $BiFeO_3$ and demonstrate the potential of using multiple wavelength Raman spectroscopy as a means to probe electronic levels in multiferroic materials. After an introduction to the crystal structure, the electronic properties and the experimental setup, an overview to the general particularities of Raman scattering on $BiFeO_3$ is given. Afterwards, we investigate the electronic band structure of $BiFeO_3$ by using twelve different excitation wavelengths ranging from deep blue (442 nm or 2.8 eV) to near-infrared (785 nm or 1.6 eV). To investigate the reported strong, and not entirely understood dependence of the band gap on temperature, wavelength-dependent measurements are also conducted as a function of temperature.

5.1 Structure of $BiFeO_3$

Bismuth ferrite crystallizes in the rhombohedral *R3c* structure with a unit cell axis $a_{rh} = 3.965$ Å and an angle of 89.3° at room temperature[20]. It is often convenient to express the structure in a hexagonal settings since the axis of highest symmetry is parallel to the long hexagonal axis which is also the direction of polarization of $BiFeO_3$ and likewise the z-axis of the Raman tensors. In Fig. 5.1 the hexagonal structure is illustrated with the lattice parameters $a_{hex} = 5.58$ Å and $c_{hex} = 13.90$ Å[20]. The square in Fig. 5.1 indicates the pseudo-cubic cell, which is exposed in Fig. 5.2. As we can appreciate from Fig. 5.1 the polar axis is along the $[111]_{pc}$ direction in pseudo-cubic settings as indicated by the arrow in Fig. 5.2.

$BiFeO_3$ crystals can show rich domain patterns. All domain walls depend

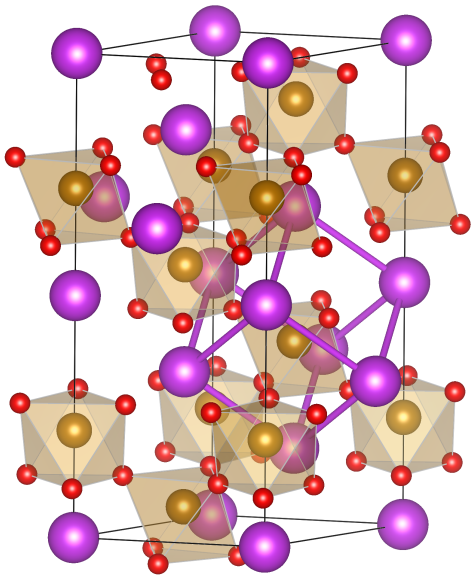

Figure 5.1: Hexagonal representation of $BiFeO_3$. The thin black lines indicate the hexagonal unit cell. The thick purple lines represent the pseudo-cubic settings.[196]

on the orientation change of the polarization direction in two subsequent face-connected unit cells in the pseudo-cubic setting. There are three types of domain walls. Tail-to-tail or head-to-head connections give rise to 71° domain walls, head-to-tail to 109° domain walls and opposite polarizations to 180° domain walls[20].

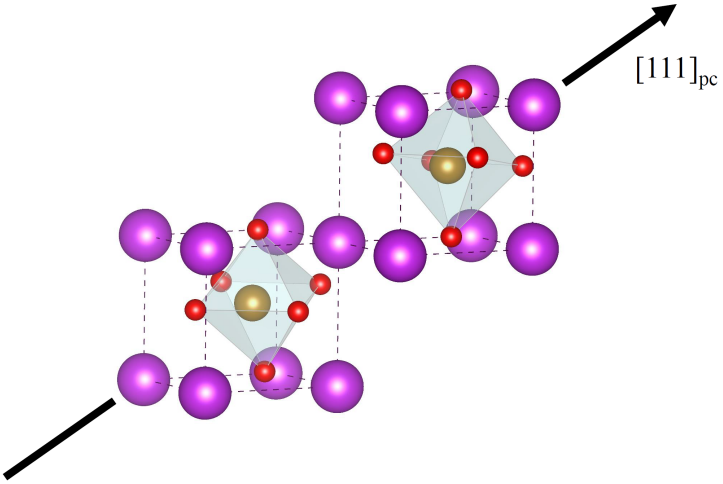

Figure 5.2: Pseudo-cubic representation of $BiFeO_3$. The arrow along $[111]_{pc}$ indicates the polar axis.[196]

5.2 Optical properties and band structure

As indicated in the introduction there are several open questions about the electronic transitions in $BiFeO_3$. From absorption studies on single crystals[182] and thin films[183–186] it is established that the band gap of $BiFeO_3$ has a value of approximately 2.7 eV. Reflectance spectroscopy, however, revealed lower band gap values: Ramachandran *et al.* reported a band gap of 2.5 eV for polycrystalline $BiFeO_3$[197] and the band gap of nano-crystalline samples was found in the range of only 2.2 eV by Bai and co-workers[198]. In contrary, photoluminescence measurements suggest a direct band gap for single crystal $BiFeO_3$ at about 3 eV[199].
The strong shrinking of the band gap with temperature reported by Palai *et al.*[187] (see also Fig. 5.8) has not been confirmed for thin films. Zelezny *et al.* report a change in band gap energy from 2.76 to 2.70 eV between 300 and 550 K[200] and Basu and co-workers found a narrowing of the band gap from 2.70 to 2.55 eV over a range from 4 to 750 K[183]. Both reports show a significantly slower shrinking of the band gap with temperature when compared to the measurements on bulk $BiFeO_3$ of Palai and co-workers.
The situation remains unclear when reviewing the calculated electronic band structures of $BiFeO_3$. Clark and Robertson calculated the band structure by using the so-called screened exchange method (and LSDA)[201,202]. This band structure shows a very flat valence band. However, calculation of

Goffinet *et al.*[203] (LDA, WC (GGA), LDA+U, B1-WC (hybrid) functionals (using CRYSTAL06 except LDA+U (VASP))) or Neaton *et al.*[204] (LSDA) do not find a flat valence band. Goffinet's and Neaton's band structure results are very similar, independent of the technique, but substantially different to the band structures of Clark and Robertson. Temperature dependent electronic band structures are generally difficult to calculate. Some information may be drawn from the band structures of the orthorhombic and cubic high-temperature phases of $BiFeO_3$. Indeed, these calculations indicate a closure of the indirect band gap[187]. However, the calculated band structures (apart from the smaller band gap) remain essentially the same when going from the orthorhombic to the cubic phase, which is not intuitive with respect to the structural reorientation of this phase transition.

5.3 Additional experimental setup and samples

This study has been performed in collaboration with Prof. Dr. M. Cazayous and Dr. C. Toulouse, Université 7, Paris, France. Using the setups of both groups, we have access to twelve different excitation wavelengths: 442, 532, 633 and 785 nm laser lines of the Renishaw Raman microscope described in section 2.1 and 458, 466, 476, 482, 496, 514, 520, 532, 568 and 647 nm laser lines in the laboratory in Paris. The latter lasers are connected to a Jobin Yvon T64000 Raman spectrometer and measurements were performed in macro-Raman mode. The fact that for both setups a 532 nm exciting laser line was available enabled the linking of both measurement series. The wavelength-dependence of the measured intensity was corrected following the description in section 2.1. The Jobin Yvon T64000 is equipped with a white lamp for the calibration of the spectral response and the spectra were corrected for the ω^4 dependence on the exciting laser frequency. The spectra recorded with the Renishaw inVia spectrometer were normalized with respect to a CaF_2 reference crystal following the description in section 2.1. The wavelength-dependent absorption in $BiFeO_3$ was corrected using the data from Ref. 182. For temperature-dependent series the Raman spectra were corrected for thermal occupation (see section 2.1). Since the Raman intensity is strongly dependent on the crystal orientation with respect to the polarization direction of incident and scattered light (see Eq. 1.16 and 1.19), it is absolutely crucial to maintain the same orientations of sample and light polarization for all measurements and preferably the same measurement spot.

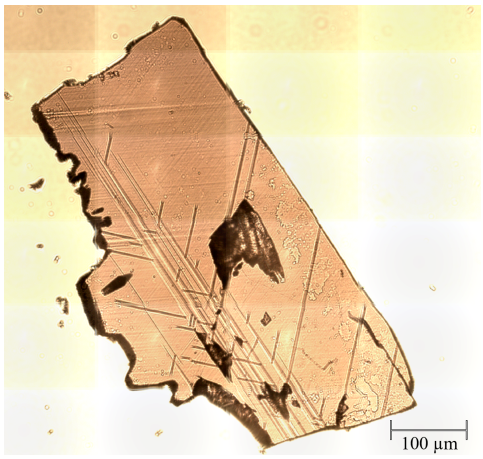

Figure 5.3: Bismuth ferrite sample primarily used in this work with dimensions of $600 \times 300 \times 10$ μm^3. The thick lines are stripe domains imbedded in larger domains. The very fine lines result from the polishing process. Large dark area is due to pieces that broke off while moving the crystal.

The crystals used in this study were grown by R. Haumont and D. Colson via the flux method[205,206]. Both crystals are $[001]_{pc}$-oriented. Fig. 5.3 shows a polarized microscope image of the $BiFeO_3$ single crystal primarily used in this study. It is roughly 600 µm in length, 300 µm in width with a thickness of 10 µm. The domains are sufficiently large to ensure that all measurements are performed for the same crystal orientation. Impurity particles at the surface were used to orientate on the sample and to repeat measurements within a lateral error of 5 µm.

5.4 The Raman spectrum of $BiFeO_3$

Before starting the investigation of the wavelength dependence of Raman-scattering on $BiFeO_3$, we provide a closer insight into the Raman scattering on bismuth ferrite. A conclusive mode assignment is an essential part of Raman spectroscopy, since it links the measured bands to symmetry and vibrational displacement. Thus, it provides an important basis for further studies.

The rhombohedral *R3c* structure of $BiFeO_3$ gives rise to 30 Γ-point vibration modes: $\Gamma = 5A_1 + 5A_2 + 10(^1E + ^2E)^\dagger$. The $5A_2$ modes are silent, and one A_1, ^1E and ^2E modes, respectively, are acoustic modes. The remaining 22 vibration modes are Raman and infrared active: $\Gamma_{\text{Raman/infrared}} = 4A_1 + 9(^1E + ^2E)$.[85,207] All Raman active modes are polar, i.e. the dipole moment changes as a consequence of the vibrational displacement. This leads to a LO-TO splitting of all modes at the Γ-point with respect to the phonon propagation direction.

The Cartesian coordinate system which determines the orthonormal axes of the Raman tensor is defined such that the z-axis is along the direction of the 3-fold axis, which coincides with c_{hex} and the pseudo-cubic $[111]_{\text{pc}}$. x- and y-axis lie in and normal to the mirror plane. Then, the corresponding Raman tensors of $BiFeO_3$ are as follows[85]:

$$\begin{pmatrix} a & & \\ & a & \\ & & b \end{pmatrix} \quad \begin{pmatrix} & c & d \\ c & & \\ d & & \end{pmatrix} \quad \begin{pmatrix} c & & \\ & -c & d \\ & d & \end{pmatrix}$$

$$A_1(\text{z}) \qquad {}^1E(\text{x}) \qquad {}^2E(\text{y})$$

As an addition to the mode symmetry, x, y and z indicate the direction of the electric field that accompanies the polar modes. Modes of E symmetry represent degenerated modes with the same frequencies and vibrational pattern but along different crystalline directions. Hence, both tensors and their polarization directions need to be specified.

Following the discussion about polar modes in section 1.2.4, we summarized the properties and selection rules of the Raman modes of $BiFeO_3$:

(i) Phonons propagating parallelly to the electric field are of longitudinal nature. Transversal optical modes propagate perpendicularly to the electric

[†]The superscripts to the E modes denote the different directions of displacement of the two degenerated modes.

field. Thus, from the Raman tensors, we find that mode assignments of pure symmetries, i.e. non-oblique modes, are possible for the following configuration in Porto's notation (for a backscattering setup): A_1(LO): z(xx/yy)$\overline{\text{z}}$; A_1(TO): x(zz/yy)$\overline{\text{x}}$, y(xx/zz)$\overline{\text{y}}$; E(TO): z(xy/yx)$\overline{\text{z}}$, x(yz/yz)$\overline{\text{x}}$, y(xz/zx)$\overline{\text{y}}$; E(LO): y(xx)$\overline{\text{y}}$. Note, the orientations given such that only one specific symmetry is probed. Solely E(LO) modes cannot be detected individually in backscattering configuration.
(ii) E(TO) can be detected independently of the phonon propagation direction.
(iii) All modes (except of E(TO) modes) are in a mixed state for all configurations which do not allow the phonon propagation-direction to be parallel to either of the three axes, x, y, z.
(iv) Only if the phonons propagate along the z-axis the E modes are degenerated, in all other orientations the degeneracy is lifted as a result of the LO-TO splitting.

There is a tremendous amount of publications on Raman spectroscopy of $BiFeO_3$, reaching from mode assignment[207–209] to the analysis of coupled properties, like spin-phonon coupling[210] or coupling to external parameters[211–214]. Theoretical calculations of the Raman and infrared spectra by Hermet *et al.*[209] and infrared studies by Lobo *et al.*[215] are of great value for the understanding of the phonon spectrum of $BiFeO_3$. Nevertheless, there are still ambiguities concerning the Raman mode assignment in the literature. Those are mainly due to the difficulty of orientating the chronically small crystals with respect to the above noted orientations.[†] Palai *et al.* published a thorough summary about difficulties and mistakes that appear in literature[217]. However, their own mode assignment is questionable, since it is at odds with the calculations by Hermet and co-workers and infrared-absorption measurements. Spectra reported by Fukumura *et al.* of a $[111]_{\text{pc}}$-oriented crystal are unfortunately of too low quality for an complete mode assignment. The same holds for Singh *et al.*[218,219], Yuan *et al.*[220], Yang *et al.*[221] and others. Cazayous and co-workers present a solid mode-assignment, nevertheless it remains unclear why the degeneracy of the lowest lying E mode is lifted for their $[111]_{\text{pc}}$-oriented crystal. Porporati *et al.*[87] and Beekman *et al.*[222] made use of the different angular dependence of the scattered light intensity in order to distinguish A_1 and E modes. However,

[†]More recently, it became possible to grow larger, well-oriented $BiFeO_3$ single crystals via laser-diode heating floating-zone method[216].

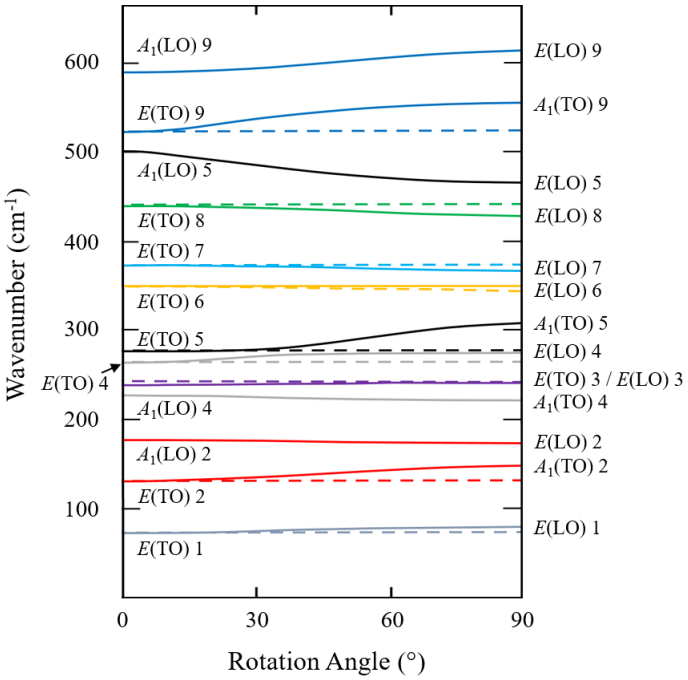

Figure 5.4: Angular phonon dispersion curves of BiFeO3. Full lines represent dispersive mixed modes, dashed lines the purely transverse E(TO) branches. The symmetries are given for 0° and 90° (notations of E(TO) modes are not repeated for 90°). The numbers group the branches by vibrational displacement. Reproduced from Ref. 223.

in both studies the mixed mode situation of the $[001]_{pc}$-oriented crystals was disregarded and the oblique character of the modes was not taken into account.

In a different approach, the evolution of the mixed mode frequencies with respect to the angle between phonon propagation-direction and polar axis was explicitly used by Hlinka *et al.* to perform the mode assignment of $BiFeO_3$ [223]. This was achieved by tracing the evolution of the vibrational bands through many different crystalline orientations from a coarse grained piece of ceramic. This method did not only allow to fully assign the vibration modes for the cases of E(TO), E(LO), A_1(TO) and A_1(LO) modes but simultaneously to follow the different mixed mode states depending on the angle between phonon propagation-direction and polar axis. The result of this work is reproduced in Fig. 5.4, giving the wavenumber as function of the angle of rotation between propagation direction and polar axis. The labeling on either side of the graph defines the symmetry for 0° and 90°.

Table 5.1: Symmetry mode assignment of our $[001]_{pc}$-oriented crystal at 93 K. The first column gives the vibrational frequency in cm^{-1}. In the second column the symmetry is given; modes of mixed symmetry are denoted "oblique". The symmetry mixing of the oblique modes is given in column three. Column four gives the vibrational displacement; the numbers group of displacement as described in the text. The asterisk indicates bands with small LO-TO splitting or very close bands (**), so that the bands cannot be resolved separately.

Frequency	Symmetry	Symmetry mixing	Displacement	
74.5	E(TO)		(1) Bi(x) anti-phase	
80.1	oblique	E(TO) - E(LO)	(1) Bi(x-y) anti-phase	
136.0	E(TO)		(2) FeO_6 displ.(x,y) in-phase	
145.0	oblique	E(TO) - A_1(TO)	(2) FeO_6 displ. in-phase	
175.0	oblique	A_1(LO) - E(LO)	(2) FeO_6 displ. in-phase	
224.6	oblique	A_1(LO) - A_1(TO)	(4) FeO_6 rotation	
241.2	E(TO)		(3) Fe(x-y), O_6 squeezing	*
	oblique	E(TO) - E(LO)	(3) Fe(x-y), O_6 squeezing	
264.8	E(TO)		(4) FeO_6 rotation	
278.0	oblique	E(TO) - E(LO)	(4) FeO_6 rotation	**
	E(TO)		(5) Fe(x-y) anti-phase to O_6(x-y)	
295.1	oblique	E(TO) - A_1(TO)	(5) Fe anti-phase to O_6	
349.7	E(TO)		(6) O_6 bending	*
	oblique	E(TO) - E(LO)	(6) O_6 bending	
373.2	E(TO)		(7) O-Fe-O scissors-like	*
	oblique	E(TO) - E(LO)	(7) O-Fe-O scissors-like	
435.0	E(TO)		(8) Fe(x,y), O_6 Jahn-Teller-like	*
	oblique	E(TO) - E(LO)	(8) Fe(x,y), O_6 Jahn-Teller-like	
472.9	oblique	A_1(LO) - E(LO)	(5) Fe anti-phase to O_6	
523.0	E(TO)		(9) O_6 bending	
542.4	oblique	E(TO) - A_1(TO)	(9) O_6 bending	
608.8	oblique	A_1(LO) - E(LO)	(9) O_6 bending	

In addition to Hlinka's work, we grouped the modes by vibrational displacement indicated by the number behind the symmetry. Since in the cubic phase a displacement triplet corresponds to a single but triply degenerated mode, we can approximate that a set of two E modes and an A_1 or A_2 belong to one type of vibrational displacement but along different crystallographic

axes. The arrangement has been done by visual inspection of the vibrational displacements of the transversal modes; the vibrational vectors were calculated by Yannick Gillet, Université catholique Louvain-la-Neuve, following the procedure of Hermet and co-workers[209]. This information allows to estimate the strength of the LO-TO splitting. Vibration modes which are little affected by the electric field show generally smaller LO-TO splitting. Here, group "3" in shows the smallest LO-TO splitting with only 2 cm^{-1}, whereas the LO-TO splitting is much larger, up to 190 cm^{-1} for group "5". In this case the impact of the electric field is larger than the anisotropy of the force constants. In general, both cases of "oblique" modes exist in $BiFeO_3$, with larger and smaller anisotropy of the force constants compared to the effect of the electric field as discussed in section 1.2.4.

For the present work, the mode assignment is based on the publication of Hlinka *et al*[223]. A Raman spectrum recorded under the excitation of a green - 532 nm - laser at 93 K is given in Fig. 5.5.

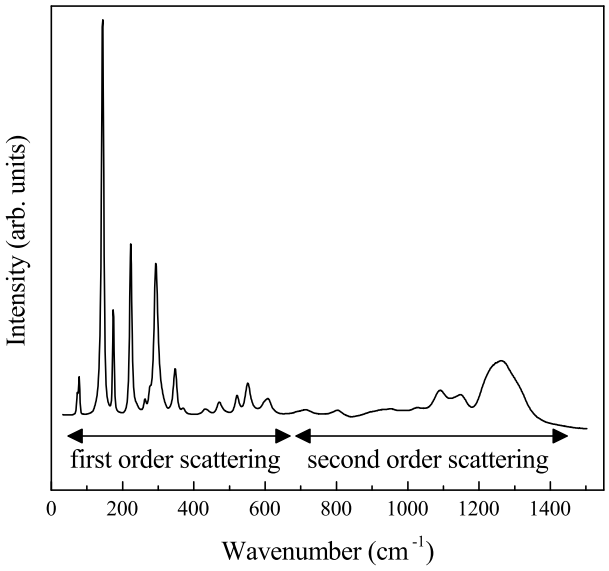

Figure 5.5: Raman spectrum of a $[001]_{pc}$-oriented $BiFeO_3$ crystal recorded under the excitation of a 532 nm laser line at 93 K to enhance the spectral resolution. Single phonon scattering can be observed up to 650 cm^{-1} (first-order) followed by second-order scattering processes up to 1400 cm^{-1}.

As mentioned earlier the crystals used in this work are oriented along the pseudo-cubic $[001]_{pc}$ direction. Thus, 22 Raman modes are expected. The band positions are in excellent agreement with the data of Hlinka and co-workers at an angle of $\sim 55°$ (angle between $[001]_{pc}$ and $[111]_{pc}$ direction). This mode assignment is presented in Table 5.1. All modes apart from E(TO) modes are in an mixed state denoted as "oblique". In column three the discrete symmetries at ends of the oblique mode branches are given.
A similar assignment is not possible for the second-order spectrum due to its continuous nature. There have been attempts for mode assignment of second-order features to overtones of first-order bands[224], however, our low temperature spectrum (Fig. 5.5) allows a higher spectral resolution, and reveals that none of the second-order features represent a clear overtone of a Γ-point first-order Raman mode. Thus the second-order spectrum appears to be more complex and the combination of several vibration modes whose origin is elsewhere in the Brillouin zone, as earlier indicated by Cazayous *et al.*[210]. For the study, a mode assignment of the second-order is not essential.

5.5 Multiwavelength Raman spectroscopy on $BiFeO_3$

After the general understanding of Raman scattering on $BiFeO_3$, we turn now to the wavelength dependent Raman scattering to investigate the electronic transitions in bismuth ferrite.
Figure 5.6(a) shows the well-defined Raman spectra under different excitation wavelengths. For better visibility the spectra are normalized to the integrated intensity of the first-order Raman scattering signal. The most prominent feature of the spectra is that the relative intensity of the different Raman bands greatly depends on the wavelength used. Figures 5.6(b) and 5.6(c) make this more apparent by magnification of two narrow spectral regions: For example, the band at 230 cm^{-1} is very strong at 442 nm but hardly observable at 785 nm; similar changes are observed for almost all modes when carefully considering the full series. The intensity of the second-order Raman spectrum, visible as broad bands in the 1000-1400 cm^{-1} range [see Fig. 5.6(d)], also depends on the exciting wavelength in agreement with previous reports[210].
As discussed in detail in section 1.2.3, variations of the total intensity and intensity ratios between different bands are characteristic features when passing from non-resonant to resonant Raman scattering. It is important to repeat at this point that great care was taken to measure in the same polarization and orientation conditions and the same spot on the sample, so that all 'trivial' effects are excluded.

5.5.1 Wavelength dependence of first-order Raman spectra

In spite of the variations in intensity ratios, all the bands in the spectra of Fig. 5.6 remain visible. Therefore, all bands in $BiFeO_3$ can be considered resonance-Raman-active. Taking advantage of the detailed mode assignment in section 5.4 and the availability of vibrational displacements of the Raman bands, we investigated the intensity ratio changes with respect to particular patterns of the ratio changes. That means, the vibrational bands were analyzed to find out if Raman bands of certain symmetry, vibrational pattern or strength of polar moment are particularly strongly enhanced. At first, we find from the first order spectra in Fig. 5.6(a) that neither the low-wavenumber region, dominated by Bi^{3+} and Fe^{3+} displacements, nor the high-wavenumber region, dominated by O^{2-} displacements, are particularly

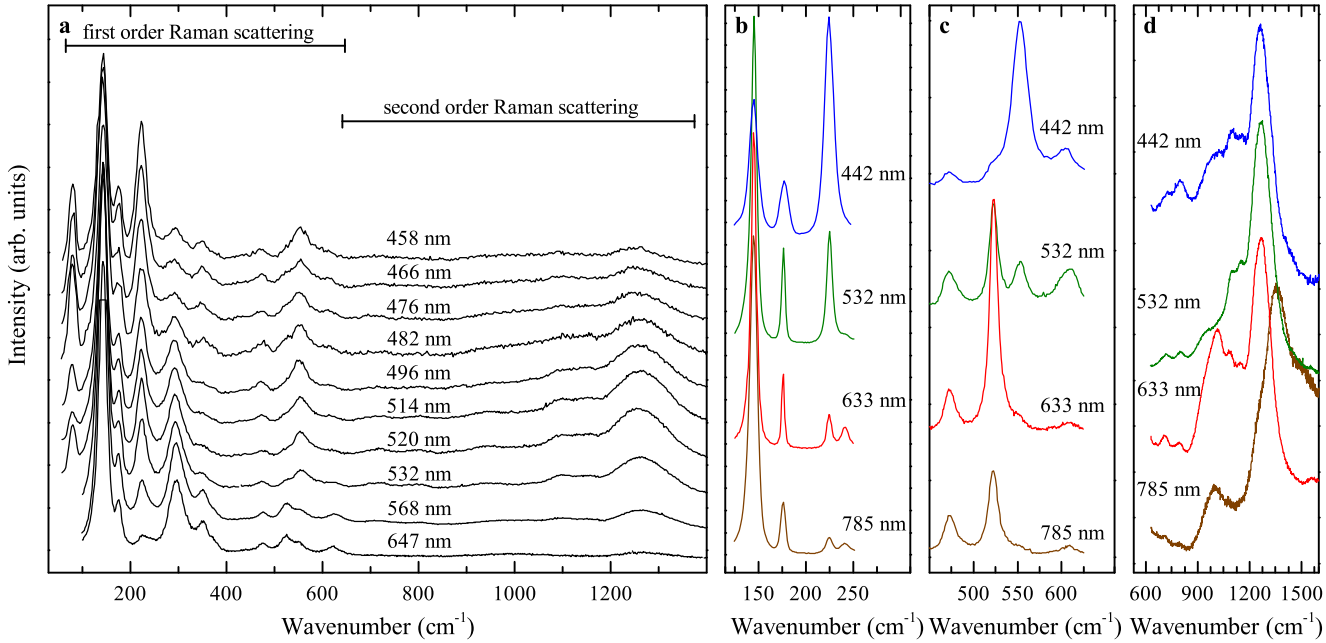

Figure 5.6: (a) Room-temperature Raman spectra for different excitation wavelengths ranging from 458 nm to 647 nm. For better visibility, the spectra were normalized to the integrated intensity of the first-order Raman scattering process. (b), (c) and (d) Zoom into low- and high-wavenumber regions of the first-order spectra, and into the region of the second-order spectra, respectively, for 4 different wavelengths. For a better definition of the Raman bands, the spectra were measured at 93 K.

strongly enhanced. The participation of certain atoms in the vibration does not seem to be necessary or favor the resonance effect. Let us have a look at the importance of symmetry, transversal and longitudinal proportion of the vibrations (see Fig. 5.6 and Table 5.1). The band at 542.4 cm^{-1} of mixed E(TO)-A_1(TO) symmetry becomes comparably strongly enhanced towards higher laser energies. However, the band at 295.1 cm^{-1} with the same symmetry properties decreases in intensity. Modes of primarily longitudinal character do not show any particular behavior such as the modes at 175.0 and 608.8 cm^{-1} (A_1(LO)-E(LO)). Further inspection reveals no pattern which could be responsible for significant intensity enhancements in the wavelength-dependent spectra of $BiFeO_3$. Thus, we conclude that the ratio changes are due to many factors including the actual vibrational displacements. Precises DFT calculations of the band intensities depending on the exciting wavelength will be necessary to disentangle the contributions.

The resonance enhancement can be quantified by integrating the intensity over the full first-order spectral range (i.e. up to 650 cm^{-1}). This integrated intensity is plotted in Fig. 5.7 for all wavelengths, revealing intensity changes by up to two orders of magnitude across the series. It remains constant between 785 and 568 nm, but then increases sharply when approaching the green laser lines leading to a first maximum at around 520 nm. Towards higher energies (smaller laser wavelengths), the integrated intensity decreases slightly before a very strong, second enhancement occurs under excitation with blue laser light (465 nm or 2.67 eV). This strong increase correlates with the reported value of 2.7 eV for the band gap. The intensity maximum at approximately 520 nm (2.38 eV) shall then correspond to a resonance process involving in-gap electronic states. Defect states related to oxygen vacancies are obvious candidates and, indeed, have been reported experimentally at 2.45 eV[186], which is also consistent with the 2.2 eV value predicted by first-principles calculations[202]. We therefore assign this second resonance enhancement at 520 nm with a valence-band-to-defect transition involving oxygen vacancies.
When comparing the Raman spectra at different excitation wavelengths, one should bear in mind that the absorption by the sample is also wavelength dependent, so that a change in the exciting laser wavelength leads to a change in penetration depth. In materials having a skin layer with different structural properties from the bulk, such as ferroelectrics in general and $BiFeO_3$ in particular[225], this effect can in principle affect the very

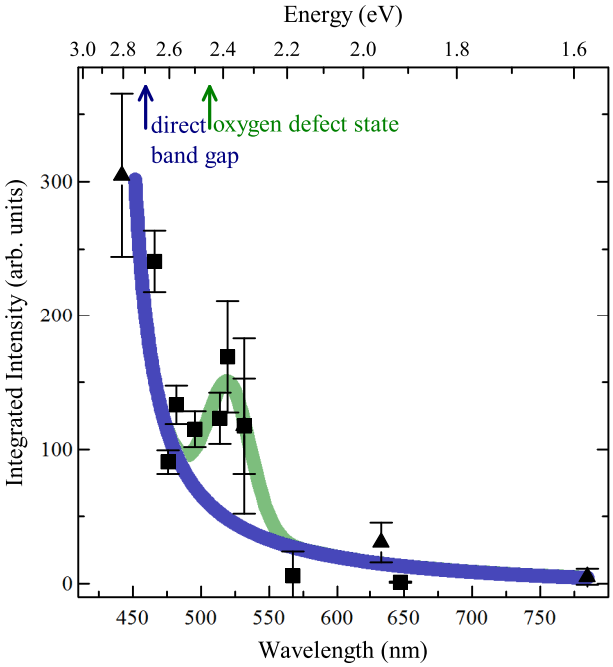

Figure 5.7: Evolution of the integrated intensity of the first-order spectra from 100 cm^{-1} to 650 cm^{-1} at room temperature. Triangles and squares are spectral data measured with the Renishaw and Jobin Yvon spectrometer, respectively. Appropriate spectrometer and absorption corrections have been applied as explained in section 2.1.3. The integrated intensity of the 647 nm spectrum (which represents the lowest intensity) has been set to one; other spectra where normalized accordingly, to provide a measure for the enhancement. Solid lines are guides for the eye.

shape of the Raman signature. However, this effect can be safely ruled out in our study considering that: (i) a structural distortion would be expected to cause shifts of the Raman frequencies, which are not observed and (ii) the skin layer in $BiFeO_3$ is not thicker than 10 nm [225,226], whereas changes of the Raman spectrum are visible for lasers penetrating much deeper in the bulk: Applying Beer-Lamberts law with the absorption data of Xu et al. [182] gives several micrometers for near-infrared to red light, several hundreds of nanometers for green light (532 nm), and 60-80 nm for blue light (442 nm).

5.5.2 Tracing the temperature dependence of the band gap

Because changes of the band transitions imply changes in the Raman resonance conditions, resonant Raman spectroscopy can now be used to track its temperature evolution, with the objective to elucidate the intriguing shrinking of the optical gap at high temperatures. This principle is illustrated in Fig. 5.8, where the band gap values determined by Palai *et al.*[187] are displayed together with the energies of three selected laser lines used in this study. Strong changes in the resonance conditions are expected when the

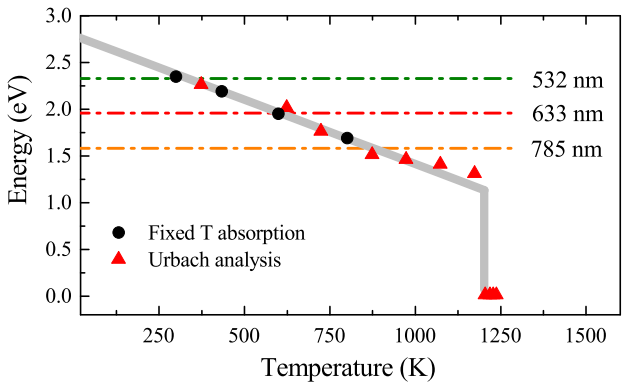

Figure 5.8: Band gap values versus temperature taken from Ref. 187, together with the energies of the 532 nm, 633 nm, and 785 nm laser lines.

laser energy is close to the reported band gap, which should be reflected in the intensity and the shape of the Raman signature.

First-order Raman scattering - direct transitions

Figures 5.9(b)-(d) show the first-order Raman spectra for temperatures ranging from 93 K to 723 K and for laser excitation wavelengths 532 nm, 633 nm, and 785 nm, i.e. for energies that coincide with the reported band gap at different temperatures. In all cases, the temperature evolution of the Raman spectra follows a typical behavior characterized by thermal broadening and a generalized low-frequency shift of all bands with increasing temperature. The intensity ratios between modes do not change significantly compared to the intensity ratio changes observed for different excitation wavelengths (see Fig. 5.6). This is underlined in Fig. 5.10 which shows a zoom into the low wavenumber region of Fig. 5.9. The bands highlighted in

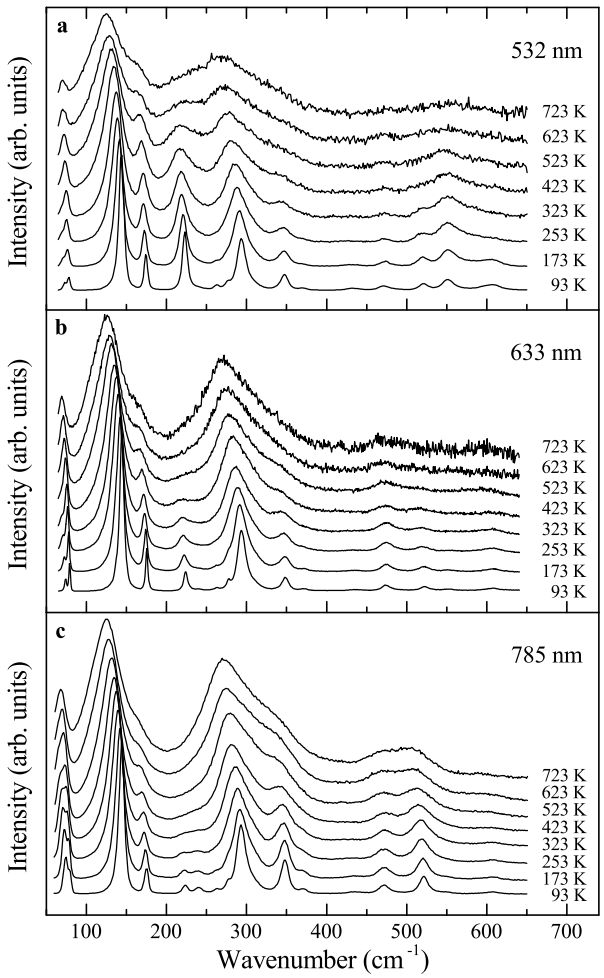

Figure 5.9: Temperature-dependent Raman spectra in the first-order frequency region for the 532 nm, 633 nm, and 785 nm laser lines.

blue (at frequencies of 172 and 222 cm^{-1}) represent two bands of significant change in intensity ratio for changing wavelengths as an example. This is quantified in Fig. 5.11 that shows the evolution of the intensity ratio for the two highlighted vibrational bands. In blue, red and black the evolution of the intensity ratios is given for the excitation laser lines of 532 nm, 633 nm and 785 nm, respectively. For comparison, this ratio evolution with respect to the wavelength change is indicated by the open squares. For changing temperature this ratio does not show any sign of the dramatic increase that characterizes the resonant regime that would be expected at high temperatures when the laser energy coincides with the reported optical band gap.

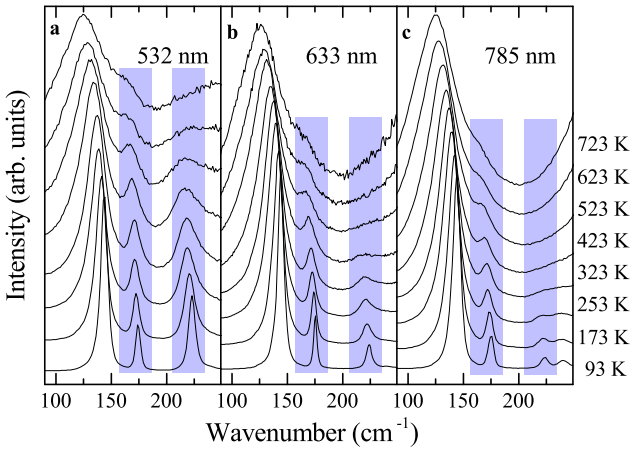

Figure 5.10: Temperature-dependent Raman spectra in the low-frequency region for the 532 nm, 633 nm, and 785 nm laser lines. The bands around 172 and 223 cm^{-1} are highlighted since the intensity ratio has been found to change dramatically in Fig. 5.6.

This leads to the at first sight surprising conclusion that the resonance conditions at a given wavelength do not change with temperature. Considering that only direct electronic transitions can be involved in first-order Raman resonances, we come to the following conclusions: (i) the temperature evolution of the optical band gap cannot be related to a shrinking of a direct electronic band gap and (ii) the electronic levels underlying the resonant Raman effect under illumination with 442 nm (assigned to direct electronic transitions) and 532 nm (oxygen vacancies) are nearly temperature independent.

Second-order Raman scattering - indirect transitions

In a second step, we have scrutinized the second-order Raman spectra. Figures 5.12(a) and (b) present the temperature evolution of the second-order Raman spectra for excitation under 532 nm and 633 nm light. The figures show a strong qualitative change in the intensity signature, which is particularly apparent when comparing the relative intensities of the broad peaks at 1010 and 1260 cm^{-1} under excitation by the 633 nm laser line. The band at 1010 cm^{-1} is strongly reduced at higher temperatures and the shape of the spectrum gradually becomes similar to the spectrum obtained for 532 nm laser at ambient temperature, albeit with differences due to different thermal

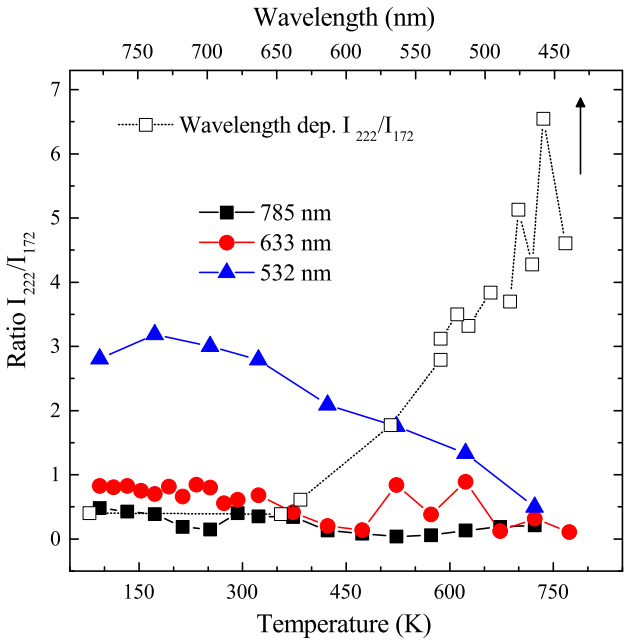

Figure 5.11: Evolution of the intensity ratio of the bands located around 172 and 223 cm^{-1} (highlighted in Fig. 5.10(a)-(c)) with temperature (bottom axis), and with excitation energy at ambient temperature (top axis).

broadenings. Conversely, the 532 nm laser line spectra at low temperatures revealed a small but distinct band at 1010 cm^{-1} [indicated by the arrow in Figs. 5.12(a) and (b)]. These qualitative changes were accompanied by a change in the overall intensity, which we quantify by the ratio between the integrated intensity (I_2) of the second-order spectrum divided by the intensity of the first-order spectrum (I_1). For both excitation wavelengths, I_2/I_1 exhibited a maximum in their temperature dependence. The observed maxima at 573 K for 633 nm and at 223 K for 532 nm retrace the temperature dependence of the reported optical band gap[187]. These changes in shape and intensity of the second-order Raman signature contrasts with the temperature-independent shape of the first-order spectrum. Because any strong change in the energies of direct electronic transitions was ruled out, the observed maxima of the ratio I_2/I_1 can be related to a temperature evolution of an indirect gap.

Other possible phenomena are more difficult to reconcile with the experimental observations. Notably, the Franck-Condon mechanism explaining the resonance behavior reported in past studies[138,227] does not have the same

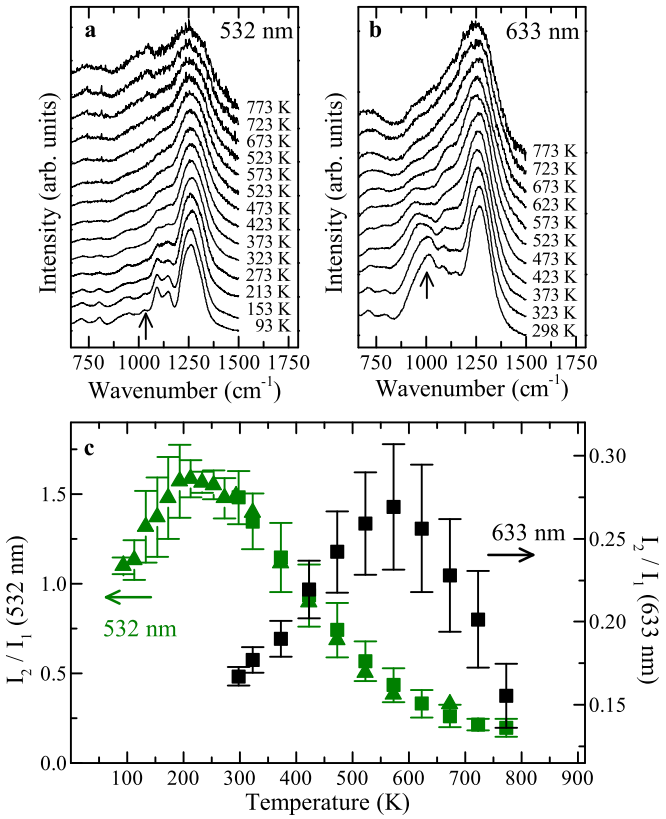

Figure 5.12: Temperature-dependent Raman spectra in the low-frequency region for the 532 nm, 633 nm, and 785 nm laser lines.

signature, both at ambient condition (e.g. no third-order scattering is observed in our studies) and as a function of temperature. Also, a magnetism-related change in the electron-phonon coupling could be admittedly hypothesized from the observation that the maximum for I_2/I_1 at 633 nm lies in the vicinity of T_N. However, it is not clear then how to explain the wavelength dependence of this maximum, and the fact that no such anomaly is observed in the vicinity of T_N in the related compound $LaFe_{0.96}Cr_{0.04}O_3$ [138].

Summary and discussion of experimental findings

Our experimental observations lead to the conclusion that the shrinking of the optical band gap is related to a temperature evolution of an electronic band gap with indirect character. This supports the view that $BiFeO_3$ is an indirect semiconductor, at least above room temperature. On the other hand, the energies of direct electronic transitions show no temperature dependence, which implies in turn non-trivial temperature modifications of the electronic band structure. Even though only hypotheses can be formulated at this stage for the details of this temperature dependence, we note that the hypothesis of a strong electron-phonon coupling inducing an important renormalization of the electronic levels is consistent with the fact that the highest valence band originates predominantly from the oxygen p states whereas the lowest conduction band is mainly formed by iron d states. The low relative mass of the oxygen atom then leads naturally to comparatively large nuclear displacements in the corresponding phonon modes, and hence the largest temperature dependence of oxygen-based bands, i.e. the bands of the FeO_6 octahedra[204]. In Fig. 5.13 a schematic sketch of the change of the electronic band structure evolution from low to high temperatures is depicted. In this scenario the conduction band minimum M_2 is lowered for higher temperatures with respect to the conduction band minimum M_1 leading to a shrinking of the indirect band gap, whereas the direct transition remains stable. It needs to be emphasized at this point that this scenario only represents one possibility for the closure of the band gap and no specific shapes of the electronic bands were taken into account. In fact, the difficulty of describing the closure of the band gap in more detail is partly due to the lack of consistent first-principle calculations of the band structure in literature as mentioned before.

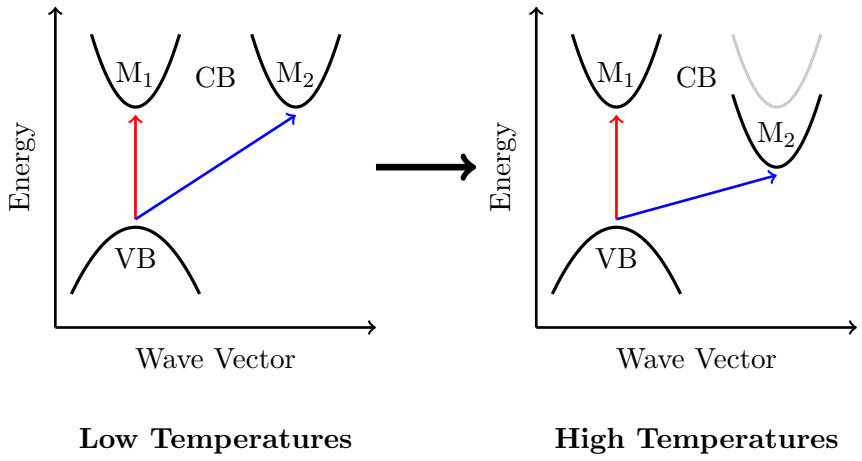

Figure 5.13: Sketch of the electronic band structures in $BiFeO_3$ for low (left) and high (right) temperatures. VB describes the valence band, M_1 and M_2 the band minima of the conduction band (CB). Direct and indirect transitions are indicated by red and blue arrows, respectively.

5.6 Conclusion

Using multi-wavelength dependent Raman scattering we were able to identify direct electronic transitions of $BiFeO_3$ at ambient conditions. It was possible to identify the band gap closure of $BiFeO_3$ as a shrinking process of an indirect band gap. Therefore, we took advantage of the restriction of first-order Raman scattering to direct electronic transitions and the possibility to probe indirect transitions by the second-order Raman scattering process. Further work will be needed to confirm the picture of the band gap closure, including both calculations at finite temperatures and experiments to follow carefully the optical absorption with temperature and to probe electronic levels directly.
More generally, resonant Raman scattering appears as a powerful tool to follow electronic excitations up to relatively high temperatures, in a way that should be applicable beyond $BiFeO_3$ to a broad range of materials showing absorption in the visible range, and thereby to contribute to the understanding of electronic structures in photoferroelectrics.

Conclusion and Perspectives

In the present work, we studied iron-based perovskite-type oxide systems: a series of rare-earth orthoferrites $R\mathrm{FeO_3}$ representing the most common perovskite space group, *Pnma*, with a particular focus on $\mathrm{SmFeO_3}$ and the most investigated multiferroic compound, $\mathrm{BiFeO_3}$.

In the first part of this work, we presented a thorough Raman scattering study of rare-earth orthoferrites $R\mathrm{FeO_3}$. The Raman modes of six rare-earth orthoferrites (La, Sm, Eu, Gd, Tb, Dy) were assigned to the corresponding symmetries and vibrational displacements. We identified the A_g soft modes which are related to the octrahedra tilt system for all compounds. In the framework of Landau theory, we proposed a relation of order parameter, soft mode and size of rare earth. This relation is applicable for all series of perovskite compounds in which only the different sizes of the A cation trigger the degree of octahedra tilting.
This study on rare-earth orthoferrites sets the basis and reference for future work on coupling phenomena or structural changes in orthoferrites, be it in temperature- or pressure- dependent measurements, or for the interpretation of Raman spectra for the series of solid solutions. The precise assignment of the vibrational pattern of the Raman bands will ease investigation and interpretation of Raman data of $R\mathrm{FeO_3}$ thin films, namely to monitor and better understand how the two-dimensional strain/stress is mediated in the film for different substrates or film thicknesses.

In the second part, we applied this knowledge and extended it inspecting the structural properties of $\mathrm{SmFeO_3}$ as a function of temperature by Raman spectroscopy, RUS and birefringence measurements. Besides anomalies at the known magnetic transitions at the Néel temperature and during the spin reorientation process, we found new anomalies above the spin ordering temperature of the iron spins and below room temperature.

The spin ordering of the iron spins at the Néel temperature has no measurable impact on the lattice. During the spin reorientation process, however, the elastic constants show an interesting softening. The anomaly at high temperature is rather subtle and asks for further inspection to confirm its existence and clarify its origin.
The low-temperature anomalies were attributed to a spin-lattice interaction due to ordering of the samarium-samarium spin sublattice. The similarities of these features in the Raman spectra to data of structurally similar materials such as $TbMnO_3$ and $GdMnO_3$ indicate, that this phenomenon is not only restricted to $SmFeO_3$. However, an advantage of $SmFeO_3$ (and potentially of other RFeO$_3$) is the clear separation of the ordering temperatures of the iron and samarium sublattices, in contrast to orthomanganites or orthochromites. This separation in temperature allows to study the ordering processes independently. Furthermore, the high ordering temperature of the samarium spin sublattice is particularly interesting since the magnetism of rare-earths is commonly assumed to order below 10 K. This finding raises the question if high-ordering temperature is a property unique to samarium or $SmFeO_3$, or if other rare-earth components show a similar behavior. Based on the here observed signature, and the Sm^{3+}-spin ordering scenario, we suggest in-depth investigations of the magnetic structure at low temperatures, e.g. by neutron scattering, and first-principle calculations, to confirm or evoke new scenarios.
As a perspective, both structural instabilities, during spin reorientation and at low temperatures, offer various possibilities for spin-lattice coupling interactions. Naturally, the question raises if the ordering of the samarium spins can induce a ferroelectric displacement as it has been found in $GdFeO_3$, or if an additional magnetic field will give rise to ferroelectricity such as in $DyFeO_3$[15]. Equally it is of interest to investigate the process of spin reorientation under an external magnetic or electric field in order to trigger a potential structural phase transition. Additionally, in $SmFeO_3$ thin films, different strain states depending on the substrate may act in favour of certain magnetically induced phase changes. Similarly, heterostructures of $SmFeO_3$ and an either strongly magnetic or polar material are of interest to be investigated if they can trigger multiferroic properties.
Overall, $SmFeO_3$ offers a large "playground" with a wide range of spin-lattice coupling possibilities worth investigating.

Finally, we have traced the closure of the electronic band gap with the temperature in $BiFeO_3$ using multi-wavelength Raman spectroscopy. This investigation reveals an interesting and complex signature, well beyond what is generally discussed in literature. The complexity is due to both in-band gap states and likely a complex electronic structure. Importantly, the comparison of first- and second-order scattering allowed us to demonstrate that the intriguing closure of the band gap of $BiFeO_3$ results from a shrinking of an indirect transition. While we have proposed a first schematic scenario, a detailed understanding asks for future additional investigations, by both theoretical and experimental means. In particular, our studies motivates the reinvestigation of the calculated band structure, also temperature-dependent first-principle calculations could help to understand the closure of the indirect band gap. The experimental investigation of the shape of the valence band and change of the band structure with the temperature by resonant inelastic X-ray scattering shall be helpful to understand the electronic properties of $BiFeO_3$. Furthermore, the role of defect states requires attention, such as the proposed oxygen-defects states. Defects in $BiFeO_3$ have been shown to be of importance for the bulk-photovoltaic effect [228], so that more detailed knowledge on the nature and energy states of the defects will be of value.

Our approach to $BiFeO_3$ is so far unique in the field of multiferroic oxides. More generally, we expect that investigations by wavelength-dependent Raman scattering are of interest for other functional oxides materials. The approach will be namely of value for the investigation of electronic transitions, in particular to distinguish between direct and indirect transitions. Besides functional oxides, the approach may be interesting for the structurally complex organic-inorganic perovskite-solar-cells recently receiving much attention.

Bibliography

[1] Http://www.independent.co.uk/environment/global-warming-data-centres-to-consume-three-times-as-much-energy-in-next-decade-experts-warn-a6830086.html (2016).

[2] Awada, U., Li, K., and Shen, Y. *International Journal of Cloud Computing and services science* **3**(3), 31–48 (2014).

[3] Http://ec.europa.eu/research/industrial_technologies/promotional-material_en.html. (2016).

[4] Bibes, M. *Nature materials* **11**(5), 354–7 may (2012).

[5] Ramesh, R. and Spaldin, N. A. *Nature materials* **6**(1), 21–9 jan (2007).

[6] Khomskii, D. *Physics* **2**, 20 mar (2009).

[7] Hill, N. A. *The Journal of Physical Chemistry B* **104**(29), 6694–6709 jul (2000).

[8] Tokunaga, Y., Furukawa, N., Sakai, H., Taguchi, Y., Arima, T.-h., and Tokura, Y. *Nature materials* **8**(7), 558–562 (2009).

[9] Kreisel, J., Alexe, M., and Thomas, P. A. *Nature materials* **11**(4), 260 apr (2012).

[10] Fridkin, V. M. and Popov, B. N. *Physica Status Solidi (a)* **46**(2), 729–733 apr (1978).

[11] Fridkin, V. M. *Photoferroelectrics*. Springer-Verlag, Berlin Heidelberg New York, (1979).

[12] Fridkin, V. M. *Crystallography Reports* **46**(4), 654–658 jul (2001).

[13] White, R. L. *Journal of Applied Physics* **40**(1969), 1061–1069 (1969).

[14] Cheng, Z., Hong, F., Wang, Y., Ozawa, K., Fujii, H., Kimura, H., Du, Y., Wang, X., and Dou, S. *ACS Applied Materials and Interfaces* (2014).

[15] Tokunaga, Y., Iguchi, S., Arima, T., and Tokura, Y. *Physical Review Letters* **101**(9), 097205 aug (2008).

[16] Lee, J.-H., Jeong, Y. K., Park, J. H., Oak, M.-A., Jang, H. M., Son, J. Y., and Scott, J. F. *Physical Review Letters* **107**(11), 117201 sep (2011).

[17] Johnson, R. D., Terada, N., and Radaelli, P. G. *Physical Review Letters* **108**(21), 219701 may (2012).

[18] Lee, J.-H., Jeong, Y. K., Park, J. H., Oak, M.-A., Jang, H. M., Son, J. Y., and Scott, J. F. *Physical Review Letters* **108**(21), 219702 may (2012).

[19] Kuo, C.-Y., Drees, Y., Fernández-Díaz, M. T., Zhao, L., Vasylechko, L., Sheptyakov, D., Bell, A. M. T., Pi, T. W., Lin, H.-J., Wu, M.-K., Pellegrin, E., Valvidares, S. M., Li, Z. W., Adler, P., Todorova, A., Küchler, R., Steppke, A., Tjeng, L. H., Hu, Z., and Komarek, A. C. *Physical Review Letters* **113**(21), 217203 nov (2014).

[20] Catalan, G. and Scott, J. F. *Advanced Materials* **21**(24), 2463–2485 jun (2009).

[21] Choi, T., Lee, S., Choi, Y. J., Kiryukhin, V., and Cheong, S.-W. *Science* **324**(5923), 63–6 apr (2009).

[22] Yang, S. Y., Seidel, J., Byrnes, S. J., Shafer, P., Yang, C.-H., Rossell, M. D., Yu, P., Chu, Y.-H., Scott, J. F., Ager, J. W., Martin, L. W., and Ramesh, R. *Nature nanotechnology* **5**(2), 143–7 feb (2010).

[23] Kundys, B., Viret, M., Colson, D., and Kundys, D. O. *Nature materials* **9**(10), 803–5 oct (2010).

[24] Longo, V. M., das Graça Sampaio Costa, M., Zirpole Simões, A., Rosa, I. L. V., Santos, C. O. P., Andrés, J., Longo, E., and Varela, J. A. *Physical Chemistry Chemical Physics* **12**(27), 7566 (2010).

[25] Momma, K. and Izumi, F. *Journal of Applied Crystallography* **44**(6), 1272–1276 dec (2011).

[26] Chakhmouradian, A. R. and Woodward, P. M. *Physics and Chemistry of Minerals* **41**(6), 387–391 jun (2014).

[27] Mitchell, R. H. *Perovskites: Modern and ancient.* Almaz Press, Ontario, (2002).

[28] Goldschmidt, V. M. *Die Naturwissenschaften* **14**(21), 477–485 may (1926).

[29] Megaw, H. D. *Crystal structures: A working approach (Studies in physics and chemistry).* W.B. Saunders Co., Philadelphia PA, (1973).

[30] Glazer, A. M. *Acta Crystallographica Section B Structural Crystallography and Crystal Chemistry* **28**(11), 3384–3392 nov (1972).

[31] Glazer, A. M. *Acta Crystallographica Section A* **31**(6), 756–762 nov (1975).

[32] Woodward, P. M. *Acta Crystallographica Section B Structural Science* **53**(1), 32–43 feb (1997).

[33] Woodward, P. M. *Acta Crystallographica B* **53**(1), 44–66 (1997).

[34] Lufaso, M. W. and Woodward, P. M. *Acta Crystallographica Section B Structural Science* **60**(1), 10–20 feb (2004).

[35] Howard, C. J. and Stokes, H. T. *Acta Crystallographica Section B Structural Science* **54**(6), 782–789 (1998).

[36] Howard, C. J. and Zhang, Z. *Acta Crystallographica Section B: Structural Science* **60**(2), 249–251 (2004).

[37] Howard, C. J. and Stokes, H. T. *Acta Crystallographica Section B Structural Science* **60**(6), 674–684 (2004).

[38] Howard, C. J. and Stokes, H. T. *Acta Crystallographica Section A Foundations of Crystallography* **61**(1), 93–111 jan (2005).

[39] Howard, C. J. and Carpenter, M. A. *Acta Crystallographica Section B Structural Science* **66**(1), 40–50 feb (2010).

[40] Carpenter, M. A. and Howard, C. J. *Acta Crystallographica Section B Structural Science* **65**(2), 134–146 apr (2009).

[41] Sangaletti, L., Depero, L. E., Allieri, B., Nunziante, P., and Traversa, E. *Journal of the European Ceramic Society* **21**(6), 719–726 jun (2001).

[42] Goodenough, J. B. *Annual Review of Materials Science* **28**(1), 1–27 aug (1998).

[43] Carpenter, M. A. and Howard, C. J. *Acta Crystallographica Section B: Structural Science* **65**(2), 147–159 (2009).

[44] Burns, P. C., Hawthorne, F. C., Hofmeister, A. M., and Moret, S. L. *Physics and Chemistry of Minerals* **23**(3) apr (1996).

[45] Yoshiasa, A., Nakatani, T., Nakatsuka, A., Okube, M., Sugiyama, K., and Mashimo, T. *Acta Crystallographica Section B Structural Science, Crystal Engineering and Materials* **72**(3), 381–388 jun (2016).

[46] Stokes, H. T., Kisi, E. H., Hatch, D. M., and Howard, C. J. *Acta Crystallographica Section B: Structural Science* **58**(6), 934–938 (2002).

[47] Stølen, S., Bakken, E., and Mohn, C. E. *Physical Chemistry Chemical Physics* **8**(4), 429–47 jan (2006).

[48] Bhatnagar, A., Roy Chaudhuri, A., Heon Kim, Y., Hesse, D., and Alexe, M. *Nature Communications* **4**(May), 1–8 nov (2013).

[49] Huang, H. *Nature Photonics* **4**(3), 134–135 mar (2010).

[50] Glass, A. M., von der Linde, D., and Negran, T. J. *Applied Physics Letters* **25**(4), 233 (1974).

[51] Fraygola, B., Frizon, N., Nascimento, W. J., Coelho, A. A., Garcia, D., and Eiras, J. A. *Ferroelectrics* **470**(1), 221–226 oct (2014).

[52] Evans, D. M., Alexe, M., Schilling, A., Kumar, A., Sanchez, D., Ortega, N., Katiyar, R. S., Scott, J. F., and Gregg, J. M. *Advanced Materials* **27**(39), 6068–6073 (2015).

[53] Lebeugle, D., Colson, D., Forget, A., Viret, M., Bataille, A. M., and Gukasov, A. *Physical Review Letters* **100**(22), 227602 jun (2008).

[54] Goto, T., Kimura, T., Lawes, G., Ramirez, A. P., and Tokura, Y. *Physical Review Letters* **92**(25 I), 257201–1 (2004).

[55] Kenzelmann, M., Harris, A. B., Jonas, S., Broholm, C., Schefer, J., Kim, S. B., Zhang, C. L., Cheong, S.-W., Vajk, O. P., and Lynn, J. W. *Physical Review Letters* **95**(8), 087206 aug (2005).

[56] Lorenz, B., Wang, Y. Q., and Chu, C. W. *Physical Review B - Condensed Matter and Materials Physics* **76**(10), 1–5 (2007).

[57] Smekal, A. *Die Naturwissenschaften* **11**(43), 873–875 oct (1923).

[58] Raman, C. V. and Krishnan, K. S. *Nature* **121**(3048), 501–502 (1928).

[59] Landsberg, G. and Mandelstam, L. *Die Naturwissenschaften* **16**(28), 557–558 jul (1928).

[60] Nobelprize.org. (2014).

[61] Singh, R. *Physics in Perspective* **4**(4), 399–420 dec (2002).

[62] Jermyn, M., Mok, K., Mercier, J., Desroches, J., Pichette, J., Saint-Arnaud, K., Bernstein, L., Guiot, M.-C., Petrecca, K., and Leblond, F. *Science Translational Medicine* **7**(274), 274ra19–274ra19 feb (2015).

[63] Butler, H. J., Ashton, L., Bird, B., Cinque, G., Curtis, K., Esmondewhite, K., Fullwood, N. J., Gardner, B., Martin, P. L., Walsh, M. J., Mcainsh, M. R., Stone, N., Martin, F. L., Butler, H. J., and Martinhirsch, P. L. *Nature Protocols* **11**(4), 1–47 (2016).

[64] Scott, J. F. *Reviews of Modern Physics* **46**(1), 83–128 jan (1974).

[65] Scott, J. F. *Physical Review* **183**(3), 823–825 (1969).

[66] Guennou, M., Bouvier, P., Krikler, B., Kreisel, J., Haumont, R., and Garbarino, G. *Physical Review B* **82**(13), 134101 oct (2010).

[67] Perry, C. and Hall, D. *Physical Review Letters* **15**(17), 700–702 oct (1965).

[68] Guennou, M., Bouvier, P., and Kreisel, J. *Physical Review B* **81**(5), 054115 feb (2010).

[69] Tenne, D. A., Bruchhausen, A., Lanzillotti-Kimura, N. D., Fainstein, A., Katiyar, R. S., Cantarero, A., Soukiassian, A., Vaithyanathan, V., Haeni, J. H., Tian, W., Schlom, D. G., Choi, K. J., Kim, D. M., Eom, C. B., Sun, H. P., Pan, X. Q., Li, Y. L., Chen, L. Q., Jia, Q. X.,

Nakhmanson, S. M., Rabe, K. M., and Xi, X. X. *Science (New York, N.Y.)* **313**(5793), 1614–6 sep (2006).

[70] Weber, M. C., Guennou, M., Dix, N., Pesquera, D., Sánchez, F., Herranz, G., Fontcuberta, J., López-Conesa, L., Estradé, S., Peiró, F., Iñiguez, J., and Kreisel, J. *Physical Review B* **94**(1), 014118 jul (2016).

[71] Sando, D., Agbelele, A., Rahmedov, D., Liu, J., Rovillain, P., Toulouse, C., Infante, I. C., Pyatakov, a. P., Fusil, S., Jacquet, E., Carrétéro, C., Deranlot, C., Lisenkov, S., Wang, D., Le Breton, J.-M., Cazayous, M., Sacuto, A., Juraszek, J., Zvezdin, a. K., Bellaiche, L., Dkhil, B., Barthélémy, A., and Bibes, M. *Nature materials* **12**(7), 641–6 jul (2013).

[72] Kreisel, J., Weber, M. C., Dix, N., Sánchez, F., Thomas, P. A., and Fontcuberta, J. *Advanced Functional Materials* **22**(23), 5044–5049 dec (2012).

[73] Chaix-Pluchery, O., Cochard, C., Jadhav, P., Kreisel, J., Dix, N., Sanchez, F., and Fontcuberta, J. *Applied Physics Letters* **99**(7), 072901 (2011).

[74] Jayaraman, V., Rodgers, K., Mukerji, I., and Spiro, T. *Science* **269**(5232), 1843–1848 sep (1995).

[75] Marcus, M. and Lewis, A. *Science* **195**(4284), 1328–1330 mar (1977).

[76] Brodsky, M., Burstein, E., Cardona, M., Falicov, L., Klein, M., Martin, R., Pinczuk, A., Pine, A., and Shen, Y.-R. *Light Scattering in Solids I*, volume 8 of *Topics in Applied Physics*. Springer Berlin Heidelberg, Berlin, Heidelberg, (1983).

[77] Cardona, M., Chang, R., Güntherodt, G., Long, M., and Vogt, H. *Light Scattering in Solids II*, volume 50 of *Topics in Applied Physics*. Springer Berlin Heidelberg, Berlin, Heidelberg, first edition, (1982).

[78] Cantarero, A., Trallero-Giner, C., and Cardona, M. *Physical Review B* **40**(18), 12290–12295 dec (1989).

[79] Yu, P. and Cardona, M. *Fundamentals of Semiconductors*. Springer, Berlin, Heidelberg, New York, 3 edition, (2005).

[80] Weinstein, B. and Cardona, M. *Physical Review B* **8**(6), 2795–2809 sep (1973).

[81] Leite, R., Scott, J., and Damen, T. *Physical Review Letters* **22**(15), 780–782 apr (1969).

[82] Hayes, W. and Loudon, R. *Scattering of Light by Crystals*. John Wiley & Sons, New York, (1978).

[83] Nye, J. *Physical properties of crystals*. Oxford University Press, Oxford, (1985).

[84] Poulet, H. and Mathieu, J. *Vibration Spectra and Symmetry of Crystals*. Gordon and breach, Paris, (1976).

[85] Kroumova, E., Aroyo, M., Perez-Mato, J., Kirov, A., Capillas, C., Ivantchev, S., and Wondratschek, H. *Phase Transitions* **76**(1-2), 155–170 jan (2003).

[86] Munisso, M. C., Zhu, W., and Pezzotti, G. *Physica Status Solidi (B)* **246**(8), 1893–1900 aug (2009).

[87] Porporati, A. A., Tsuji, K., Valant, M., Axelsson, A.-K., and Pezzotti, G. *Journal of Raman Spectroscopy* **41**(1), 84–87 jan (2010).

[88] Loudon, R. *Proceedings of the Royal Society A: Mathematical, Physical and Engineering Sciences* **275**(1361), 218–232 sep (1963).

[89] Ganguly, A. and Birman, J. *Physical Review* **162**(3), 806–816 oct (1967).

[90] Loudon, R. *Advances in Physics* **13**(52), 423–482 oct (1964).

[91] Loudon, R. *Proceedings of the Royal Society of London. Series A, Mathematical and Physical Science* **275**(1361), 218–232 sep (1963).

[92] Scott, J., Leite, R., and Damen, T. *Physical Review* **188**(3), 1285–1290 dec (1969).

[93] Scott, J. *Physical Review B* **2**(4), 1209–1211 aug (1970).

[94] Martin, R. *Physical Review B* **4**(10), 3676–3685 nov (1971).

[95] Ralston, J., Wadsack, R., and Chang, R. *Physical Review Letters* **25**(12), 814–818 sep (1970).

[96] Damen, T. and Scott, J. *Solid State Communications* **9**(6), 383–385 mar (1971).

[97] Renucci, J., Tyte, R., and Cardona, M. *Physical Review B* **11**(10), 3885–3895 may (1975).

[98] Renucci, M., Renucci, J., Zeyher, R., and Cardona, M. *Physical Review B* **10**(10), 4309–4323 nov (1974).

[99] Jain, K. and Jayanthi, C. *Physical Review B* **19**(8), 4198–4204 apr (1979).

[100] Hunklinger, S. *Festkörperphysik*. Oldenburg Wissenschaftsverlag GmbH, München, 2 edition, (2009).

[101] Mulliken, R. S. *The Journal of Chemical Physics* **23**(11), 1997 (1955).

[102] Mulliken, R. S. *The Journal of Chemical Physics* **23**(11), 1997 (1955).

[103] Shapiro, S. and Axe, J. *Physical Review B* **6**(6), 2420–2427 sep (1972).

[104] Fleury, P., Scott, J., and Worlock, J. *Physical Review Letters* **21**(1), 16–19 jul (1968).

[105] Birman, J. *Physics Letters A* **45**(3), 196 sep (1973).

[106] Shigenari, T. *Physics Letters A* **46**(4), 243–244 dec (1973).

[107] Lockwood, D. J. and Cottam, M. G. *Journal of Applied Physics* **64**(10), 5876–5878 (1988).

[108] Tell, B., Damen, T., and Porto, S. *Physical Review* **144**(2), 771–774 apr (1966).

[109] Grimsditch, M., Cardona, M., Calleja, J. M., and Meseguer, F. *Journal of Raman Spectroscopy* **10**(1), 77–81 jan (1981).

[110] Cardona, M., Chang, R., Güntherodt, G., Long, M., and Vogt, H. *Light Scattering in Solids II*. Springer-Verlag, Berlin Heidelberg New York, (1982).

[111] Loudon, R. *Journal de Physique* **26**(11), 677–683 (1965).

[112] *Metripol Birefringence Imaging System - Manual*. Oxford Cryosystems Ltd, Oxford, (1999).

[113] Wood, I. G. and Glazer, A. M. *Journal of Applied Crystallography* **13**(3), 217–223 (1980).

[114] Lethbridge, Z. A. D., Keeble, D. S., Walker, D., Thomas, P. A., and Walton, R. I. *Journal of Applied Crystallography* **43**(1), 168–175 (2010).

[115] http://www.mccrone.com/linkam-high-pressure-stage?page_id=217 (2016).

[116] McKnight, R. E. A. *Anomalous elastic behaviour associated with phase transitions, observed using resonant ultrasound spectroscopy.* PhD thesis, University of Cambridge, (2009).

[117] Carpenter, M. A., Salje, E. K. H., and Howard, C. J. *Physical Review B - Condensed Matter and Materials Physics* **85**(22), 1–16 (2012).

[118] White, R. M., Nemanich, R. J., and Herring, C. *Physical Review B* **25**, 1822–1836 (1982).

[119] Eibschütz, M., Shtrikman, S., and Treves, D. *Physical Review* **156**(2), 562–577 apr (1967).

[120] Zhao, H. J., Íñiguez, J., Chen, X. M., and Bellaiche, L. *Physical Review B* **93**(1), 014417 (2016).

[121] Cao, S., Zhao, H., Kang, B., Zhang, J., and Ren, W. *Scientific reports* **4**, 5960 jan (2014).

[122] Marshall, L. G., Cheng, J.-G., Zhou, J.-S., Goodenough, J. B., Yan, J.-Q., and Mandrus, D. G. *Physical Review B* **86**(6), 064417 aug (2012).

[123] Du, Y., Cheng, Z. X., Wang, X. L., and Dou, S. X. *Journal of Applied Physics* **107**, 09D908 (2010).

[124] Todorov, N. D., Abrashev, M. V., and Ivanov, V. G. *Journal of physics. Condensed matter : an Institute of Physics journal* **24**(17), 175404 may (2012).

[125] Iliev, M., Abrashev, M., Laverdière, J., Jandl, S., Gospodinov, M., Wang, Y.-Q., and Sun, Y.-Y. *Physical Review B* **73**(6), 3–8 feb (2006).

[126] Weber, M. C., Kreisel, J., Thomas, P. A., Newton, M., Sardar, K., and Walton, R. *Physical Review B* **85**(5), 054303 feb (2012).

[127] Chaix-Pluchery, O. and Kreisel, J. *Phase Transitions* **84**(5-6), 542–554 may (2011).

[128] Marezio, M., Remeika, J. P., and Dernier, P. D. *Acta Crystallographica Section B Structural Crystallography and Crystal Chemistry* **26**(12), 2008–2022 (1970).

[129] Zhao, Y., Weidner, D. J., Parise, J. B., and Cox, D. E. *Physics of the Earth and Planetary Interiors* **76**, 17–34 (1993).

[130] Marezio, M. and Dernier, P. *Materials Research Bulletin* **6**(1), 23–29 jan (1971).

[131] Shannon, R. D. *Acta Crystallographica A* **32**(751) (1976).

[132] Moreira, J. A., Almeida, A., Ferreira, W. S., Chaves, M. R., Oliveira, J. B., da Silva, J. M. M., Sá, M. A., Vilela, S. M. F., and Tavares, P. B. *Journal of Electroceramics* **25**(2-4), 203–211 oct (2010).

[133] Daniels, L. M., Weber, M. C., Lees, M. R., Guennou, M., Kashtiban, R. J., Sloan, J., Kreisel, J., and Walton, R. I. *Inorganic chemistry* **52**(20), 12161–9 oct (2013).

[134] Damen, T., Porto, S., and Tell, B. *Physical Review* **142**(2), 570–574 feb (1966).

[135] Iliev, M., Litvinchuk, A., Hadjiev, V., Wang, Y.-Q., Cmaidalka, J., Meng, R.-L., Sun, Y.-Y., Kolev, N., and Abrashev, M. *Physical Review B* **74**(21), 214301 dec (2006).

[136] Laverdière, J., Jandl, S., Mukhin, A., Ivanov, V., and Iliev, M. *Physical Review B* **73**, 214301 jun (2006).

[137] Andreasson, J., Holmlund, J., Knee, C., Käll, M., Börjesson, L., Naler, S., Bäckström, J., Rübhausen, M., Azad, A., and Eriksson, S.-G. *Physical Review B* **75**(10), 104302 mar (2007).

[138] Andreasson, J., Holmlund, J., Rauer, R., Käll, M., Börjesson, L., Knee, C., Eriksson, A., Eriksson, S.-G., Rübhausen, M., and Chaudhury, R. *Physical Review B* **78**(23), 235103 dec (2008).

[139] Andreasson, J., Holmlund, J., Singer, S., Knee, C., Rauer, R., Schulz, B., Käll, M., Rübhausen, M., Eriksson, S.-G., Börjesson, L., and Lichtenstein, A. *Physical Review B* **80**(7), 075103 aug (2009).

[140] Venugopalan, S. and Becker, M. M. *The Journal of Chemical Physics* **93**(6), 3833 (1990).

[141] Venugopalan, S., Dutta, M., Ramdas, A. K., and Remeika, J. P. *Physical Review B* **31**(3), 1490–1497 (1985).

[142] Koshizuka, N. and Ushioda, S. *Physical Review B* **22**(11), 5394–5399 dec (1980).

[143] Singh, M. K., Jang, H. M., Gupta, H. C., and Katiyar, R. S. *Journal of Raman Spectroscopy* **39**, 842–848 (2008).

[144] Iliev, M. N., Abrashev, M. V., Laverdière, J., Jandl, S., Gospodinov, M. M., Wang, Y.-Q., and Sun, Y.-Y. *Physical Review B* **73**(6), 064302 feb (2006).

[145] Zhou, J.-S. and Goodenough, J. B. *Physical Review Letters* **94**(6), 065501 feb (2005).

[146] Kimura, T., Goto, T., Shintani, H., Ishizaka, K., Arima, T., and Tokura, Y. *Nature* **426**(6962), 55–58 nov (2003).

[147] Matsubara, M., Manz, S., Mochizuki, M., Kubacka, T., Iyama, A., Aliouane, N., Kimura, T., Johnson, S. L., Meier, D., and Fiebig, M. *Science* **348**(6239), 1112–1115 jun (2015).

[148] Kimura, T., Lawes, G., Goto, T., Tokura, Y., and Ramirez, A. P. *Physical Review B* **71**(22), 224425 jun (2005).

[149] Jeong, Y. K., Lee, J.-H., Ahn, S.-J., and Jang, H. M. *Solid State Communications* **152**(13), 1112–1115 jul (2012).

[150] Yuan, S. J., Ren, W., Hong, F., Wang, Y. B., Zhang, J. C., Bellaiche, L., Cao, S. X., and Cao, G. *Physical Review B* **87**(18), 184405 may (2013).

[151] Zhang, K., Xu, K., Liu, X., Zhang, Z., Jin, Z., Lin, X., Li, B., Cao, S., and Ma, G. *Scientific Reports* **6**(March), 23648 mar (2016).

[152] Balkanski, M., Wallis, R. F., and Haro, E. *Physical Review B* **28**(4), 1928–1934 aug (1983).

[153] White, R., Nemanich, R., and Herring, C. *Physical Review B* **25**(3), 1822–1836 feb (1982).

[154] Ferreira, W. S., Agostinho Moreira, J., Almeida, A., Chaves, M. R., Araújo, J. P., Oliveira, J. B., Machado Da Silva, J. M., Sá, M. A., Mendonça, T. M., Simeão Carvalho, P., Kreisel, J., Ribeiro, J. L., Vieira, L. G., Tavares, P. B., and Mendonça, S. *Physical Review B* **79**(5), 054303 feb (2009).

[155] Moreira, J. A., Almeida, A., Ferreira, W. S., Araújo, J. E., Pereira, A. M., Chaves, M. R., Kreisel, J., Vilela, S. M. F., and Tavares, P. B. *Physical Review B* **81**(5), 054447 feb (2010).

[156] Bhadram, V. S., Rajeswaran, B., Sundaresan, A., and Narayana, C. *EPL (Europhysics Letters)* **101**(1), 17008 jan (2013).

[157] Sharma, Y., Sahoo, S., Perez, W., Mukherjee, S., Gupta, R., Garg, A., Chatterjee, R., and Katiyar, R. S. *Journal of Applied Physics* **115** (2014).

[158] Udagawa, M., Kohn, K., Koshizuka, N., Tsushima, T., and Tsushima, K. *Solid State Communications,* **16**, 779–783 (1975).

[159] Riedel, E. *Allgemeine und Anorganische Chemie.* Gruyter, (2004).

[160] Schiemer, J., O'Flynn, D., Balakrishnan, G., and Carpenter, M. A. *Physical Review B - Condensed Matter and Materials Physics* **88**(5), 1–6 (2013).

[161] Abe, M., Kaneta, K., Gomi, M., Mori, Y., and Nomura, S. *Japanese Journal of Applied Physics* **16**(10), 1799–1804 oct (1977).

[162] Chaturvedi, S., Shyam, P., Apte, A., Kumar, J., Bhattacharyya, A., Awasthi, A. M., and Kulkarni, S. *Physical Review B* **93**(17), 174117 (2016).

[163] Von Hippel, A. *Reviews of Modern Physics* **22**(3), 221–237 (1950).

[164] Rovillain, P., Cazayous, M., Gallais, Y., Sacuto, A., Measson, M. A., and Sakata, H. *Physical Review B - Condensed Matter and Materials Physics* **81**(5), 1–5 (2010).

[165] Takahashi, Y., Kida, N., Yamasaki, Y., Fujioka, J., Arima, T., Shimano, R., Miyahara, S., Mochizuki, M., Furukawa, N., and Tokura, Y. *Physical Review Letters* **101**(18), 1–4 (2008).

[166] Gruber, J. B., Hills, M. E., Nadler, M. P., Kokta, M. R., and Morrison, C. A. *Chemical Physics* **113**(2), 175–186 (1987).

[167] Grünberg, P. *Zeitschrift für Physik* **225**(4), 376–382 aug (1969).

[168] Grünberg, P., Hüfner, S., Orlich, E., and Schmitt, J. *Journal of Applied Physics* **40**(3), 1501 (1969).

[169] Köningstein, J. A. and Schaack, G. *Physical Review B* **2**(5), 1242–1250 sep (1970).

[170] Faulhaber, R., Hüfner, S., Orlich, E., and Schuchert, H. *Zeitschrift für Physik* **204**(2), 101–113 (1967).

[171] Schuchert, H., Hüfner, S., and Faulhaber, R. *Journal of Applied Physics* **39**(2), 1137–1138 (1968).

[172] Fleury, P. A. *Physical Review Letters* **21**(3), 151–153 jul (1968).

[173] Fleury, P. A. *Physical Review* **180**(2), 591–593 (1969).

[174] Barath, H., Kim, M., Cooper, S. L., Abbamonte, P., Fradkin, E., Mahns, I., Rübhausen, M., Aliouane, N., and Argyriou, D. N. *Physical Review B - Condensed Matter and Materials Physics* **78**(13), 1–7 (2008).

[175] Weber, M. C., Guennou, M., Toulouse, C., Cazayous, M., Gillet, Y., Gonze, X., and Kreisel, J. *Physical Review B* **93**(12), 125204 mar (2016).

[176] Catalan, G. *Phase Transitions* **81**(7-8), 729–749 jul (2008).

[177] Rovillain, P., de Sousa, R., Gallais, Y., Sacuto, A., Méasson, M. a., Colson, D., Forget, A., Bibes, M., Barthélémy, A., and Cazayous, M. *Nature Materials* **9**(12), 975–979 dec (2010).

[178] Heron, J. T., Bosse, J. L., He, Q., Gao, Y., Trassin, M., Ye, L., Clarkson, J. D., Wang, C., Liu, J., Salahuddin, S., Ralph, D. C., Schlom, D. G., Íñiguez, J., Huey, B. D., and Ramesh, R. *Nature* **516**(7531), 370–373 dec (2014).

[179] Wang, J., Neaton, J. B., Zheng, H., Nagarajan, V., Ogale, S. B., Liu, B., Viehland, D., Vaithyanathan, V., Schlom, D. G., Waghmare, U. V., Spaldin, N. a., Rabe, K. M., Wuttig, M., and Ramesh, R. *Science (New York, N.Y.)* **299**(5613), 1719–22 mar (2003).

[180] Alexe, M. and Hesse, D. *Nature Communications* **2**, 256 mar (2011).

[181] Seidel, J., Fu, D., Yang, S.-Y., Alarcón-Lladó, E., Wu, J., Ramesh, R., and Ager, J. *Physical Review Letters* **107**(12), 126805 sep (2011).

[182] Xu, X., Brinzari, T., Lee, S., Chu, Y., Martin, L., Kumar, A., McGill, S., Rai, R., Ramesh, R., Gopalan, V., Cheong, S., and Musfeldt, J. *Physical Review B* **79**(13), 134425 apr (2009).

[183] Basu, S. R., Martin, L. W., Chu, Y. H., Gajek, M., Ramesh, R., Rai, R. C., Xu, X., and Musfeldt, J. L. *Applied Physics Letters* **92**(9), 091905 (2008).

[184] Ihlefeld, J. F., Podraza, N. J., Liu, Z. K., Rai, R. C., Xu, X., Heeg, T., Chen, Y. B., Li, J., Collins, R. W., Musfeldt, J. L., Pan, X. Q., Schubert, J., Ramesh, R., and Schlom, D. G. *Applied Physics Letters* **92**(14), 142908 (2008).

[185] Kumar, A., Rai, R. C., Podraza, N. J., Denev, S., Ramirez, M., Chu, Y.-H., Martin, L. W., Ihlefeld, J., Heeg, T., Schubert, J., Schlom, D. G., Orenstein, J., Ramesh, R., Collins, R. W., Musfeldt, J. L., and Gopalan, V. *Applied Physics Letters* **92**(12), 121915 (2008).

[186] Hauser, A. J., Zhang, J., Mier, L., Ricciardo, R. A., Woodward, P. M., Gustafson, T. L., Brillson, L. J., and Yang, F. Y. *Applied Physics Letters* **92**(22), 222901 (2008).

[187] Palai, R., Katiyar, R., Schmid, H., Tissot, P., Clark, S., Robertson, J., Redfern, S., Catalan, G., and Scott, J. *Physical Review B* **77**(1), 014110 jan (2008).

[188] Wemple, S. H. *Physical Review B* **2**(7), 2679–2689 oct (1970).

[189] Leite, R. and Scott, J. *Physical Review Letters* **22**(4), 130–132 jan (1969).

[190] Scott, J., Damen, T., Leite, R., and Silfvast, W. *Solid State Communications* **7**(13), 953–955 jul (1969).

[191] Kovaleva, N. N., Kusmartseva, O. E., Kugel, K. I., Maksimov, a. a., Nuzhnyy, D., Balbashov, a. M., Demikhov, E. I., Dejneka, A., Trepakov, V. a., Kusmartsev, F. V., and Stoneham, a. M. *Journal of physics. Condensed matter : an Institute of Physics journal* **25**(15), 155602 apr (2013).

[192] Krüger, R., Schulz, B., Naler, S., Rauer, R., Budelmann, D., Bäckström, J., Kim, K., Cheong, S.-W., Perebeinos, V., and Rübhausen, M. *Physical Review Letters* **92**(9), 097203 mar (2004).

[193] Rouquette, J., Haines, J., Bornand, V., Pintard, M., Papet, P., and Sauvajol, J. L. *Physical Review B* **73**(22), 224118 jun (2007).

[194] Fraysse, G., Rouquette, J., Haines, J., Bornand, V., Papet, P., and Pereira, A. S. *Inorganic Chemistry* **51**, 12619–12625 (2012).

[195] de la Flor, G., Wehber, M., Rohrbeck, A., Aroyo, M. I., Bismayer, U., and Mihailova, B. *Physical Review B* **90**(6), 064107 aug (2014).

[196] Palewicz, A., Przeniosło, R., Sosnowska, I., and Hewat, A. W. *Acta Crystallographica Section B: Structural Science* **63**(4), 537–544 (2007).

[197] Ramachandran, B., Dixit, A., Naik, R., Lawes, G., and Rao, M. S. R. *Physical Review B* **82**(1), 012102 jul (2010).

[198] Bai, X., Wei, J., Tian, B., Liu, Y., Reiss, T., Guiblin, N., Gemeiner, P., Dkhil, B., and C. Infante, I. *The Journal of Physical Chemistry C* **120**(7), 3595–3601 (2016).

[199] Moubah, R., Schmerber, G., Rousseau, O., Colson, D., and Viret, M. *Applied Physics Express* **5**(3), 035802 feb (2012).

[200] Železný, V., Chvostová, D., Pajasová, L., Vrejoiu, I., and Alexe, M. *Applied Physics A* **100**(4), 1217–1220 jul (2010).

[201] Clark, S. J. and Robertson, J. *Applied Physics Letters* **90**(13), 132903 (2007).

[202] Clark, S. J. and Robertson, J. *Applied Physics Letters* **94**(2), 022902 (2009).

[203] Goffinet, M., Hermet, P., Bilc, D. I., and Ghosez, P. *Physical Review B - Condensed Matter and Materials Physics* **79**, 014403 (2009).

[204] Neaton, J., Ederer, C., Waghmare, U., Spaldin, N., and Rabe, K. *Physical Review B* **71**(1), 014113 jan (2005).

[205] Haumont, R., Saint-Martin, R., and Byl, C. *Phase Transitions* **81**(9), 881–888 sep (2008).

[206] Lebeugle, D., Colson, D., Forget, A., Viret, M., Bonville, P., Marucco, J. F., and Fusil, S. *Physical Review B* **76**(2), 024116 jul (2007).

[207] Iliev, M. N., Abrashev, M. V., Mazumdar, D., Shelke, V., and Gupta, A. *Physical Review B* **82**, 014107 (2010).

[208] Fukumura, H., Harima, H., Kisoda, K., Tamada, M., Noguchi, Y., and Miyayama, M. *Journal of Magnetism and Magnetic Materials* **310**(2), e367–e369 mar (2007).

[209] Hermet, P., Goffinet, M., Kreisel, J., and Ghosez, P. *Physical Review B* **75**(22), 220102 jun (2007).

[210] Cazayous, M., Sacuto, A., Lebeugle, D., and Colson, D. *The European Physical Journal B* **67**(2), 209–212 jan (2009).

[211] Cazayous, M., Malka, D., Lebeugle, D., and Colson, D. *Applied Physics Letters* **91**(7), 071910 (2007).

[212] Guennou, M., Bouvier, P., Chen, G., Dkhil, B., Haumont, R., Garbarino, G., and Kreisel, J. *Physical Review B* **84**, 174107 nov (2011).

[213] Haumont, R., Bouvier, P., Pashkin, A., Rabia, K., Frank, S., Dkhil, B., Crichton, W., Kuntscher, C., and Kreisel, J. *Physical Review B* **79**(18), 184110 may (2009).

[214] Haumont, R., Kreisel, J., Bouvier, P., and Hippert, F. *Physical Review B* **73**(13), 132101 apr (2006).

[215] Lobo, R., Moreira, R., Lebeugle, D., and Colson, D. *Physical Review B* **76**(17), 172105 nov (2007).

[216] Ito, T., Ushiyama, T., Yanagisawa, Y., Kumai, R., and Tomioka, Y. *Crystal Growth & Design* **11**(11), 5139–5143 nov (2011).

[217] Palai, R., Katiyar, R. S., Schmid, H., Scott, J. F., Champion, P. M., and Ziegler, L. D. In *AIP Conference Proceedings*, volume 1188, 1188–1189, (2010).

[218] Singh, M. K., Jang, H. M., Ryu, S., and Jo, M.-H. *Applied Physics Letters* **88**(4), 042907 (2006).

[219] Singh, M., Ryu, S., and Jang, H. *Physical Review B* **72**(13), 132101 oct (2005).

[220] Yuan, G. L., Or, S. W., and Chan, H. L. W. *Journal of Physics D: Applied Physics* **40**(4), 1196–1200 feb (2007).

[221] Yang, Y., Sun, J., Zhu, K., Liu, Y., Chen, J., and Xing, X. *Physica B: Condensed Matter* **404**(1), 171–174 jan (2009).

[222] Beekman, C., Reijnders, A., Oh, Y., Cheong, S., and Burch, K. *Physical Review B* **86**(2), 020403(R) jul (2012).

[223] Hlinka, J., Pokorny, J., Karimi, S., and Reaney, I. *Physical Review B* **83**(2), 020101(R) jan (2011).

[224] Ramirez, M. O., Krishnamurthi, M., Denev, S., Kumar, A., Yang, S.-y., Orenstein, J., Ramesh, R., and Gopalan, V. *Applied Physics Letters* **92**(022511) (2008).

[225] Martí, X., Ferrer, P., Herrero-Albillos, J., Narvaez, J., Holy, V., Barrett, N., Alexe, M., and Catalan, G. *Physical Review Letters* **106**(23), 236101 jun (2011).

[226] Domingo, N., Narvaez, J., Alexe, M., and Catalan, G. *Journal of Applied Physics* **113**(18), 187220 (2013).

[227] Fujioka, Y., Frantti, J., and Kakihana, M. *The Journal of Physical Chemistry B* **108**(44), 17012–17014 nov (2004).

[228] Yang, M., Bhatnagar, A., and Alexe, M. *Advanced Electronic Materials* **1**(11), 1–5 (2015).